

FABRICATION AND CHARACTERIZATION
OF QUASI-2D CORRELATED SYSTEMS

By

Tung-Wu Hsieh

A DISSERTATION

Submitted to
Michigan State University
in partial fulfillment of the requirements
for the degree of

Physics—Doctor of Philosophy

2017

ABSTRACT

FABRICATION AND CHARACTERIZATION OF QUASI-2D CORRELATED SYSTEMS

By

Tung-Wu Hsieh

The combination of nanostructure and correlated systems has been an interesting field in the frontier of condensed matter physics. Exploring and understanding the physical properties of correlated electron materials with reduced dimensionalities is the focus of this study. For this purpose, we fabricated thin flakes of calcium ruthenate ($\text{Ca}_3\text{Ru}_2\text{O}_7$) and iron telluride (Fe_{1+y}Te) with various thickness via mechanical exfoliation and characterized their magneto-electronic transport properties. The two materials are chosen for their rich phase transitions in structure, conductivity and magnetic orders.

The electronic transport properties of exfoliated $\text{Ca}_3\text{Ru}_2\text{O}_7$ flakes have been investigated as a function of thickness. We find that flakes thinner than 10 nm are more insulating and show drastic changes in magnetoresistance and metal-insulator transitions. A possible scenario might be enhanced RuO_6 octahedral distortion due to the loss of apical oxygen atoms on the cleaved surfaces. This may play a more significant role in thinner flakes as the surface-to-volume ratio increases. The study establishes a control of ruthenate properties by dimensionality and connects the fields of two-dimensional materials and correlated electron systems.

In Fe_{1+y}Te exfoliated-flake devices we find the first-order structural phase transition in Fe_{1+y}Te bulk becomes broadened in flakes with an intermediate thickness accompanying a superconducting-like dip below 10K. Further reducing the thickness of the flakes wipes out all features, and the flakes behaves like a highly-disordered two-

dimensional system exhibiting charge-localized states with largely enhanced MR ratio. The behavior can be well described by Mott's variable range hopping regime, with a localization length ~ 10 nm which may originate from the excess iron atoms.

One of the future goals of this project is the carrier doping on exfoliated thin flakes (gating effect) using either solid high- κ dielectric or ionic liquid. Another goal will be exploring more perovskite type materials since our unique exfoliation method may be the only choice to mechanically cleave the layered structured crystals with strong interlayer binding force to date. Characterization of the structure of exfoliated flakes will be also an important work to further verify the origin of exotic behaviors of the flakes.

ACKNOWLEDGEMENTS

I would like to thank my advisor Prof. Xianglin Ke for his support after I switched from the former group in the middle of my graduate school and giving me the challenging task of exfoliating calcium ruthenate. And I really appreciate the help from our staff scientist Dr. Reza Loloee, the project cannot be finished without the precious experience and inspiring suggestions from Reza. On the measurement part Dr. Tao Zou is the one helps me the most, a lot of my data is taken efficiently with his written LabVIEW program. I have to thank Michael Gottschalk for spending enormous time in finding ruthenate flakes and scanning AFM. When learning the e-beam lithography, I am grateful that Dr. Eric Gingrich and Dr. William Martinez provided me a lot of useful tips helping me quickly getting my first ruthenate flake device done. For the ionic liquid problems and static charge problems, I appreciate Prof. Zhixian Zhou and Dr. Hsun-Jen Chuang in the Wayne State University because they generously spent their time and used their instrument working with me to find the solutions. I will remember that Prof. Scott Pratt and Prof. Brage Golding encouraged me in continuing my PhD. There are still many people generously helped me in my graduate student life I could not include all in this acknowledgement but will be remembered forever. Finally I would like to thank my wife Dr. Yung-Hsiu Tang for supporting me and bringing me Claire, the cutest baby in the world. At the end, I have to say the work is so challenging that it cannot be done without the help from everyone.

TABLE OF CONTENTS

| | |
|--|-----|
| LIST OF TABLES..... | v |
| LIST OF FIGURES..... | vi |
| Chapter 1 Introduction and Motivation | 1 |
| 1.1 Motivation:..... | 1 |
| 1.2 Formation of Mott-insulators..... | 5 |
| 1.3 Calcium ruthenate $\text{Ca}_3\text{Ru}_2\text{O}_7$ | 7 |
| 1.4 Antiferromagnetic ground state and transitions in Fe_{1+y}Te | 8 |
| 1.5 Why electrical transport measurements? | 9 |
| Chapter 2 Characterization methods..... | 11 |
| 2.1 Visibility of exfoliated flakes on substrates:..... | 11 |
| 2.2 Atomic force microscopy..... | 17 |
| 2.3 Scanning electron microscopy | 21 |
| 2.4 Raman spectroscopy | 23 |
| Chapter 3 Preparation of devices | 27 |
| 3.1 Preparation of substrates | 29 |
| 3.2 Exfoliation (Gorilla glue method)..... | 31 |
| 3.3 E-beam lithography..... | 34 |
| 3.4 Wiring and ESD protection..... | 39 |
| 3.5 Contact resistance and 4-probe measurement..... | 45 |
| 3.6 Ionic liquid gating..... | 50 |
| Chapter 4 Calcium ruthenate thin flake study | 62 |
| 4.1 Bulk material properties of $\text{Ca}_3\text{Ru}_2\text{O}_7$ | 62 |
| 4.2 MIT in thin flakes | 66 |
| 4.3 Magnetoresistance and antiferromagnetic transition | 71 |
| 4.4 Lateral dimension effect?..... | 78 |
| 4.5 MIT in Ca_2RuO_4 flakes..... | 81 |
| 4.6 Summary..... | 84 |
| Chapter 5 Properties of Fe_{1+y}Te thin flakes | 86 |
| 5.1 Introduction:..... | 86 |
| 5.2 Fe_{1+y}Te nanoflake devices | 90 |
| 5.3 Superconductor-like intermediate thin flakes | 95 |
| 5.4 VRH model in ultra-thin flakes | 98 |
| 5.5 Exfoliated $\text{FeSe}_{0.5}\text{Te}_{0.5}$ flakes and ionic liquid gating | 103 |
| 5.6 Summary..... | 107 |
| Chapter 6 Summary and Future Vision | 109 |
| REFERENCES..... | 113 |

LIST OF TABLES

| | |
|---|----|
| Table 1.1: Comparison of measurement techniques available to our group | 10 |
| Table 2.1: Fitting parameters of refractive index of $\text{Ca}_3\text{Ru}_2\text{O}_7$ | 13 |

LIST OF FIGURES

| | |
|---|----|
| Figure 1.1: Metal-insulator phase diagram based on the Hubbard model..... | 6 |
| Figure 2.1: The real and imaginary part of refractive index of $\text{Ca}_3\text{Ru}_2\text{O}_7$ | 12 |
| Figure 2.2: Averaged refractive index of $\text{Ca}_3\text{Ru}_2\text{O}_7$ | 13 |
| Figure 2.3: Idea of the reflection contrast..... | 14 |
| Figure 2.4: Simulated reflectivity of $\text{Ca}_3\text{Ru}_2\text{O}_7$ few layers on SiO_2/Si substrate. | 16 |
| Figure 2.5: Simulated reflectivity contrast for 10 layers of $\text{Ca}_3\text{Ru}_2\text{O}_7$ on top of SiO_2/Si substrates. | 17 |
| Figure 2.6: AFM tapping mode. | 18 |
| Figure 2.7: Several examples of common problems in AFM scanning..... | 20 |
| Figure 2.8: Flattening the AFM image by data processing. | 21 |
| Figure 2.9: The Stokes/anti-Stokes process..... | 25 |
| Figure 2.10: The experimental setup of Raman spectroscopy..... | 26 |
| Figure 3.1: The substrate design..... | 30 |
| Figure 3.2: Setup to crack the crystal along the direction of ab-plane. | 32 |
| Figure 3.3: Collecting flakes from broken crystal. | 32 |
| Figure 3.4: Examples of exfoliated flakes. | 33 |
| Figure 3.5: The workflow of e-beam lithography. | 34 |
| Figure 3.6: Alignment marks for e-beam lithography..... | 36 |
| Figure 3.7: Matching designed patterns with optical images. | 37 |
| Figure 3.8: Fabrication of electrodes on flakes. | 38 |
| Figure 3.9: Plasma cleaning of the residue..... | 39 |
| Figure 3.10: ESD hazard. | 40 |
| Figure 3.11: The SEM image of a burned device..... | 40 |
| Figure 3.12: Grounding aluminum case covering the stereo microscope region. | 42 |

| | |
|--|----|
| Figure 3.13: The grounding base of PPMS sample puck. | 43 |
| Figure 3.14: Other anti-ESD apparatus. | 43 |
| Figure 3.15: Baked silver epoxy on the chip. | 44 |
| Figure 3.16: Flow diagram of wiring procedures. | 45 |
| Figure 3.17: The I-V curve of a large FeTe flake from 300K to 10K. | 47 |
| Figure 3.18: The evolution of V_t as a function of temperature for two pairs of electrodes. | 48 |
| Figure 3.19: Contact resistance of a 54 nm $Fe_{1+y}Te$ flake device fabricated with in-situ ion-milling procedure. | 49 |
| Figure 3.20: Resistor model of 4-probe measurement. | 50 |
| Figure 3.21: The chemical composition of $DEME^+$ (top) and TFSI. | 51 |
| Figure 3.22: The idea of ionic liquid gating (cross-section of a IL-gating device). | 52 |
| Figure 3.23: Microscope setup. | 53 |
| Figure 3.24: The toothpick attached on the optical microstage used in dipping ionic liquid on the chip. | 53 |
| Figure 3.25: An ionic liquid drop on Ca_2RuO_4 device. | 54 |
| Figure 3.26: SiO_x ring surrounded device with ionic liquid dropped. | 55 |
| Figure 3.27: Leakage current as a function of gate voltage at room temperature. | 56 |
| Figure 3.28: Gate voltage influence on 4-probe resistance measurement. | 56 |
| Figure 3.29: Breakdown of the ionic liquid at room temperature. Both of the devices are Ca_2RuO_4 thin flakes. | 57 |
| Figure 3.30: Etched surface by ionic liquid after the measurement. | 57 |
| Figure 3.31: Graphene resistance as a function of gate voltage. | 59 |
| Figure 3.32: The image of graphene device and the R-V curve. | 60 |
| Figure 4.1: Schematics of RuO_6 octahedral distortion in $Ca_3Ru_2O_7$ | 65 |
| Figure 4.2: The metal-insulator transition and AFM transition of bulk $Ca_3Ru_2O_7$ | 66 |
| Figure 4.3: AFM images of exfoliated $Ca_3Ru_2O_7$ flakes. | 68 |
| Figure 4.4: R-T curves of $Ca_3Ru_2O_7$ exfoliated flakes. | 69 |
| Figure 4.5: The MR comparison as a function of angle of in-plane magnetic field. | 73 |

| | |
|---|-----|
| Figure 4.6: MR of 13/8 nm flake as a function of field strength at various temperatures..... | 76 |
| Figure 4.7: The magnetoresistance of 9nm $\text{Ca}_3\text{Ru}_2\text{O}_7$ flake..... | 77 |
| Figure 4.8: The R-T curves of the 7nm flake. | 78 |
| Figure 4.9: The magnetoresistance of the 7nm flake..... | 78 |
| Figure 4.10: The comparison of $\text{Ca}_3\text{Ru}_2\text{O}_7$ flakes with minor difference in thickness but dramatic difference in low-temperature R-T behavior difference..... | 79 |
| Figure 4.11: Ca_2RuO_4 crystal structure. | 82 |
| Figure 4.12: Ca_2RuO_4 images of devices. | 83 |
| Figure 4.13: The comparison of R-T curve of the bulk and 60nm flake around the transition temperature..... | 84 |
| Figure 5.1. The structure of Fe_{1+y}Te | 87 |
| Figure 5.2: Phase diagram of $\text{Fe}(\text{Te}_{1-x}\text{Se}_x)$ | 88 |
| Figure 5.3: The bulk properties of Fe_{1+y}Te crystal. | 88 |
| Figure 5.4: Images of an 11 nm exfoliated Fe_{1+y}Te flake..... | 91 |
| Figure 5.5: The images of 15nm Fe_{1+y}Te flake. | 92 |
| Figure 5.6: Raman modes of Fe_{1+y}Te crystal..... | 93 |
| Figure 5.7: Raman spectra of a 12nm Fe_{1+y}Te flake..... | 94 |
| Figure 5.8: The I-V curve of the 15nm flake measured at 10K..... | 95 |
| Figure 5.9: R-T curve of thick and intermediate flakes..... | 96 |
| Figure 5.10: The increase of resistance over several baking process..... | 97 |
| Figure 5.11: R-T curves of thin insulating flakes..... | 98 |
| Figure 5.12: Fitting of VRH model | 100 |
| Figure 5.13: Comparison on MR..... | 101 |
| Figure 5.14: Magnetoresistance of 16nm and 11nm Fe_{1+y}Te flakes..... | 101 |
| Figure 5.15: The evolution of superconductivity in exfoliated $\text{FeSe}_{0.5}\text{Te}_{0.5}$ flakes. | 104 |
| Figure 5.16: The ionic liquid gating effect study on FeSe exfoliated flakes..... | 104 |
| Figure 5.17: The fabricated $\text{FeSe}_{0.5}\text{Te}_{0.5}$ device with flake thickness 47nm. | 105 |

Figure 5.18: The R-T curve of superconducting $\text{FeSe}_{0.5}\text{Te}_{0.5}$ 47nm flake..... 106

Figure 5.19: The device with the ionic liquid gating..... 107

Chapter 1

Introduction and Motivation

This chapter focuses mainly on the motivation of this thesis study. General motivation about why we want to study the nanostructured correlated material is described in Section 1.1. A brief introduction on Mott-insulator and motivation of calcium ruthenate nanoflake study is given in Section 1.2. The interesting properties and the possibility of new findings in exfoliation of Fe_{1+y}Te nanoflakes are introduced in 1.3. Finally, a table of comparison on measurement methods and the reason why we study these materials mainly by transport method are explained in Section 1.4.

1.1 Motivation

Solid state materials in nature usually fall into three categories: conductors, insulators and semiconductors based on the separation of energy band gaps. Most of transport properties can be well predicted by the electronic band theory without considering electron-electron interaction despite the fact that the Coulomb force between electrons is actually very strong when they are closed to each other. The reason given by conventional solid-state-physics textbooks is: electron clouds shield the Coulomb interaction and the strong repulsion from many electrons cancels each other so the overall behavior is similar as if there was no interaction (with some correction rules based on interaction like Hund's rule). This counter-intuitive picture is amazingly applicable for many materials but, of course, not always true. Magnetic materials showing macroscopic

magnetic moments induced by strongly coupled d-orbital electrons stand as a great example while conventional superconductors discovered by Kamerlingh Onnes in 1911 with non-dissipating supercurrents (explained by BCS theory, in which electron-phonon interaction split the energy levels) serves as another one. These materials in which exotic properties are intrigued by electron-electron-interaction are called (strongly) correlated electron systems. Many of transition metal oxides are considered correlated electron systems as de Boer and Verwey first discussed the discrepancy of band theory prediction on NiO (later called Mott-insulator and features metal-insulator transition), in 1937¹. High- T_c superconductor² and iron-based superconductor^{3,4} are also members of this group. The mysterious physical phenomena in correlated systems are interesting not only because they are not completely understood but also being extremely sensitive to perturbations. The well-known T_c dependence on minor change of oxygen deficiency in YBCO superconductor manifests the importance of stoichiometry. In transitional metal oxides, metal-insulator transition can be manipulated by perturbation parameters like doping, pressure and fields: VO_2 ⁵⁻⁷, manganites^{8,9}, ruthenates¹⁰⁻¹³ and many other examples.

Nowadays, nanostructured-material has been a new rising research field. Thanks to the progress in fabrication technique and thin film technology in decades, preparing and probing materials in few-atom size in given dimensions become possible and the interactions on the reduced dimension e. g. the surface of the thin film or the edge of the constrictions become prominent. Also the dimension reaching the coherence length of the carriers may induce quantum mechanical effects. For example the conductance in low-

dimensional systems can be quantized such as carbon nanotubes¹⁴ and two-dimensional electron gas on GaAs/AlGaAs heterostructures¹⁵.

The main motivation of the dissertation work is to combine the nanostructures and correlated systems. Because correlated systems are extremely sensitive to perturbations as mentioned above, tuning the systems by the other parameter, the dimension, is an exciting direction. By constriction of the length scales on correlated systems in nanoscales, probing single domain behavior, controlling material properties using electrostatic gating, investigating surface effect and unraveling quantum mechanical phenomena emerging at nanoscale all become possible. The route has already attracted intense interests in the field of strongly correlated materials. For instance, researchers have already tried etching YBCO thin films with focused ion beam (FIB) in narrow constrictions and found the quantum of resistance $R = h/4e^2$ being the deterministic factor to suppress high- T_c superconductivity¹⁶. Single domain and the role of strain in metal-insulator transition have been observed in VO_2 nanobeams^{17,18} as well. And more recently the application of ionic-liquid technique is introduced on thin-film transition metal oxide to tune the transition temperature¹⁹ or the magnetic properties²⁰.

To realize the nanostructures of correlated systems, there are several existing ways. The reduction of the first dimension can be realized by the fabrication of thin films with the thickness in nanoscale. Conventional thin film deposition technique includes both chemical vapor deposition (CVD) and physical vapor deposition (PVD). High quality thin films through CVD usually require epitaxial growth, which is the deposition on specific substrates with similar lattice structure to the desired material laying atoms one after another for building the exact crystal structure with atomic precision. Single

crystal thin films can be grown using this method. But the cost of the instruments and limitation of the substrate hindering many research groups from using this technique. Also, a large substrate-film mismatch strain is inevitable such that the intrinsic property of the thin film without strain is not reachable through this method. PVD takes a vaporization process of the parent compound, by thermal energy or laser excitation, to deposit the thin film much faster than CVD, and usually does not require a specific substrate. Unfortunately the quality is usually worse than epitaxial growth so growing a single crystal thin film through this method is almost impossible. The correlated systems are sensitive to stoichiometry so any growth method without comparable quality to single crystal undermines further research on fundamental properties.

There is another route invented recently. Since the discovery of peculiar properties of graphene²¹, mechanical exfoliation using the “scotch-tape” method has been widely applied to prepare thin flakes from layered-structured materials which can preserve the crystallinity and stoichiometry from bulk without the strain effect compared to epitaxial grown thin films. Graphene, MoS₂²², topological insulator Bi₂Te₃²³ and more 2D materials have been found, broadening the horizon of nanostructured materials.

The dissertation work takes the route in fabrication and characterization of devices of exfoliated quasi-two-dimensional correlated systems, including calcium ruthenate Ca₃Ru₂O₇ and iron chalcogenide FeTe. These two categories of materials are chosen because of their layered structures and rich phases in bulk which are anticipated to be altered significantly in the exfoliated nanoflake form with reduced dimensionality along the c-axis. We will discuss on the basic ideas of the interesting phenomena briefly and the motivation to study these materials in this chapter.

1.2 Formation of Mott-insulators

From the Aufbau principle, electrons fill lower energy bands to higher energy bands. With the Fermi energy lies inside a band, one would expect the system to be metallic from the classical band theory since an incomplete band can accommodate excited carriers with little energies. The case is broken in certain materials where the electron-electron interaction takes part in and prevents the hopping of the carriers. As a result the band is split, leading to the formation of Mott-insulators. The earliest discussed Mott-insulator in 1937 is the nickel oxide¹ in which Mott argued that most of the electrons at low temperature are localized and the repulsion between electrons prevent them from hopping in near positions²⁴. For that reason it takes too much energy for electrons to hop from one site to the neighboring sites, thus the system becomes insulator. While the interaction strength (U/t) serves as an essential parameter in the formation of Mott-insulator, the filling of carrier density which usually leads to the metallicity of the system serves the other. With the basic idea of Hubbard model going to be introduced below, the phase diagram of Mott-insulators can be plotted with simply these two important factors²⁵:

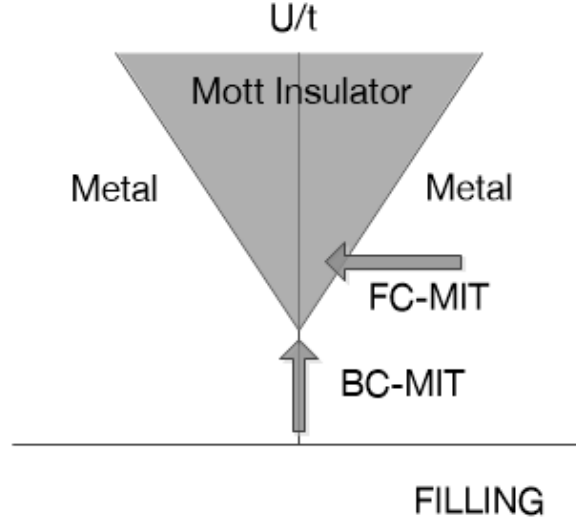


Figure 1.1: Metal-insulator phase diagram based on the Hubbard model.

The shaded area is the Mott-insulator, which can be achieved by both bandwidth-control metal-insulator-transition (BC-MIT) or filling control (FC-MIT) (From Imada et al., (1998)²⁵)

The origin of theoretical approach to the MIT starts from the well-known Hubbard model. Based on the tight-binding approximation, the Hubbard model Hamiltonian contains both the hopping term and the on-site interaction. It is a great simplification considering only electrons in the single band keeping the essentials of the electron correlations. The Hamiltonian H takes the form:

$$\begin{aligned}
 H &= H_t + H_U - \mu N \\
 H_t &= -t \sum_{\langle ij \rangle} (c_{i\sigma}^\dagger c_{j\sigma} + \text{H.c.}) \\
 H_U &= U \sum_i (n_{i\uparrow} - \frac{1}{2})(n_{i\downarrow} - \frac{1}{2})
 \end{aligned}$$

The $c_{i\sigma}$ is the annihilation operator at site i and spin σ , t is the hopping integral and the U is the on-site interaction energy. n is the number operator and $N \equiv \sum_{i\sigma} n_{i\sigma}$.

From this simple model the single band split into lower and upper Hubbard band that could explain the behavior of many Mott-insulators called Mott-Hubbard compound. While in realistic cases, for example in the transitional metal oxides, the hybridization of adjacent atomic orbitals like oxygen 2p and transition metal d-orbital may induce the charge transfer as the other important mechanism of Mott-insulators. Most of the known Mott-insulators are in these two categories.

1.3 Calcium ruthenate $\text{Ca}_3\text{Ru}_2\text{O}_7$

Among vast choices of strongly correlated materials, we chose the calcium ruthenate bilayer $\text{Ca}_3\text{Ru}_2\text{O}_7$ as our main subject of study. Not only because of its layered structure, there are many interesting aspects arising from the electronic and atomic structure of this specific material. Two phase transitions at $T_N = 56\text{K}$ manifesting a paramagnetic-antiferromagnetic transition and $T_{\text{MIT}} = 48\text{K}$ corresponding to a metal-insulator-like transition accompanied with the change of in-plane magnetic moment direction. The magnetic anisotropy is intimately related to the structural anisotropy with different degrees of RuO_6 octahedral tilting angles in the a-axis and b-axis.

We anticipate a radical change of physical properties in exfoliated ruthenate flakes for a couple of reasons: Firstly, the interbilayer coupling is playing a crucial role in the antiferromagnetic transitions, thus the symmetry breaking at the surface can alter the transition dramatically and the effect can be observed with enhanced surface-to-volume ratio. Secondly, the distortion of RuO_6 octahedron, which is a significant factor in the magnetic anisotropy mentioned in the previous paragraph, may be largely altered in the nanosheets and resulting a strong modification of electronic and magnetic properties. As

discussed in 1.1, the epitaxial growth of the material is extremely difficult especially on the order of few-nanometer giving us a motivation to develop the exfoliation method.

Our work on the calcium ruthenate focuses on the thickness dependence of metal-insulator transition and magnetotransport behavior, as well as the lateral dimension effect. Detailed information on device fabrication, characterization and the main result of measurements will be presented in Chapter 4.

1.4 Antiferromagnetic ground state and transitions in Fe_{1+y}Te

The other subjects of interest is Fe_{1+y}Te , which is an non-superconducting end member of the 11-type Fe-based superconductor $\text{Fe}_{1+y}(\text{Se}_x\text{Te}_{1-x})$. The material is antiferromagnetic at temperature below 65~75K (depending on the concentration of excess iron).^{26,27} The transition comes simultaneously with structural tetragonal-orthorhombic transition^{28,29}, and a semiconductor-metal transition with a sharp discontinuous jump of the resistivity. Even though the bulk crystal is non-superconductive, superconductivity can be triggered by incorporating oxygen³⁰, or introducing a tensile strain³¹ in the thin film form with T_c around 10K (oxygen) and 9.1~13K (strain) which is comparable to bulk FeSe. Perturbing the Fe_{1+y}Te system and searching for the superconductivity will be an interesting subject to explore. As we tune the structure by removing the constraint of adjacent layers, all of the properties and phase transitions listed above are possibly to change.

Our goal of studying Fe_{1+y}Te exfoliated flakes is to examine the effects of reduced dimensionality on the multiple transitions and to search the possible superconductivity without applying pressure/strain and oxidation. Although there are already a few existing works on FeSe and $\text{FeSe}_x\text{Te}_{1-x}$ using the mechanical exfoliation

method^{32,33}, Fe_{1+y}Te nanoflakes remain unexplored and calls for detailed investigation considering the bulk being the parent compound of the superconducting FeSe and $\text{FeSe}_x\text{Te}_{1-x}$. In addition, the recent SP(spin-polarized)-STM study on Fe_{1+y}Te discovering the re-orientation of magnetic moments of the surface atoms³⁴ leads to a great inspiration on the possibility of surface effect in the exfoliated flakes. The main result of the Fe_{1+y}Te project will be discussed in the Chapter 5 of this thesis.

1.5 Why electrical transport measurements?

The study of the proposed system mostly relies on the electrical transport measurement of exfoliated flakes. Though the selection of methodology strongly depends on the existing facility of the lab, transport measurement is the most direct way to confirm the metal-insulator transition and can probe some magnetic transition indirectly through magnetoresistance measurements, although the measurements require long-hours of device fabrication process in order to lay electrodes on the micrometer-sized flakes and suffer from bad contact resistance, electrostatic discharges, and many other problems. Note that magnetic moment measurements using SQUID or VSM are not realistic for small flakes, and the neutron scattering which can determine the microscopic magnetic structure also requires large bulky samples. There are also Raman spectroscopy and other optical measurements available for thin flake, but the temperature dependent measurement is not available for reachable commercial instruments. As a consequence, we use transport measurement as our principle research method, while on early stage of study we also use commercial Raman system in Prof. Swain's lab, and an ellipsometer in Prof. Bruening' lab, both in Dept. of Chemistry MSU, in order to confirm the exfoliated flakes are real ones coming from the bulk material.

| Method | Range | Advantages | Limitation |
|--------------------------|-----------------------------|--|---|
| transport measurement | 2-380K 0-9 Tesla | Small samples Resistance info. | Need device fabrication Sample burning |
| Raman spec. | RT, 0 field (commercial) | Less damage to samples Lattice information | Commercial instruments cannot scan T and H |
| SQUID | 2-300K 0-9 Tesla | No damage to samples Magnetic moment info. | Need large samples |
| Neutron scattering | 4-300K 0-11 Tesla | No damage to samples Magnetic structure info. | Need large samples |

Table 1.1: Comparison of measurement techniques available to our group

Chapter 2

Characterization methods

This chapter discusses the major characterization method utilized in this dissertation. In Section 2.1 the visibility of $\text{Ca}_3\text{Ru}_2\text{O}_7$ flakes is analyzed through transfer matrix method based on the refractive index data we measured on bulk crystal. Section 2.2 contains a brief introduction on atomic force microscope (AFM) and how data is taken and analyzed, including examples showing typical symptoms of scanning and the treatment. In Section 2.3 I will discuss briefly the working principle of SEM and EDX. Section 2.4 will be the basic physical principles of Raman spectroscopy and an example of experimental setup.

2.1 Visibility of exfoliated flakes on substrates:

Since the monolayers of 2D materials has been obtained by exfoliation methods including graphene²¹, MoS_2 ²², NbSe_2 ³⁵ and many others, a natural question arises: How can it be possible to see the few-nm flakes with naked eyes? The answer depends on the optical contrast of the thin flakes on the substrate as proposed by Blake et al,³⁶. From the experience human being usually can catch things with ~5% of contrast at the most sensitive wavelength region to naked eyes (500~550nm). To make sure exfoliated thin flakes on substrates can be identified, I have measured the refractive index of $\text{Ca}_3\text{Ru}_2\text{O}_7$ crystal with an ellipsometer in Prof. Merlin Bruening's group (Dept. of Chemistry, MSU) and then simulate the reflection contrast of few-layer $\text{Ca}_3\text{Ru}_2\text{O}_7$ on SiO_2 /Si substrate with the transfer matrix method to see if it is possible to see few-layer flakes on SiO_2

90nm and 300nm substrates. The refractive index has been measured 3 times and averaged. According to Prof. Bruening, the values from 400~450 nm and 700~750 nm are not accurate. The raw data are shown in Figure 2.1.

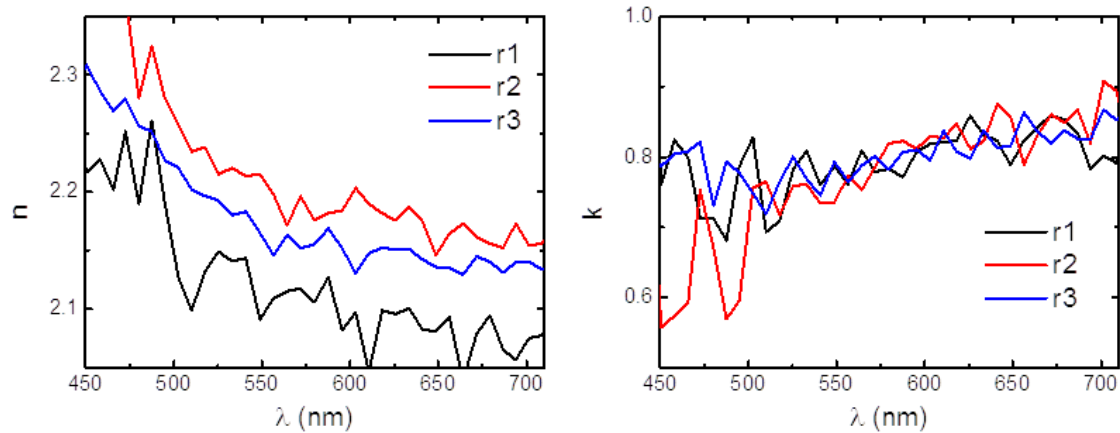


Figure 2.1: The real and imaginary part of refractive index of $\text{Ca}_3\text{Ru}_2\text{O}_7$.

Crystal measured at 3 different points (labeled r1, r2 and r3) with an ellipsometer. Data in 400~450 nm and 700~750 nm should not be trusted.

Ideally, the real part and imaginary part should follow the Kramers-Kronig (KK) relations in the whole range of wavelength, but because we are only interested in the visible light region, we use empirical equations which won't satisfy KK relations to fit the data. One is the Cauchy's equation for the real part and the imaginary part is fit with a linear function. The purpose of fitting is to attain a smooth approximation of refractive index for the reflective contrast simulation. I averaged the 3 measurements only in the reliable region (450~700 nm) for fitting. The real data is fitted with MATLAB function "nlinfit" (nonlinear regression) and imaginary data is fitted with Origin "Fit linear" function (least-square method)

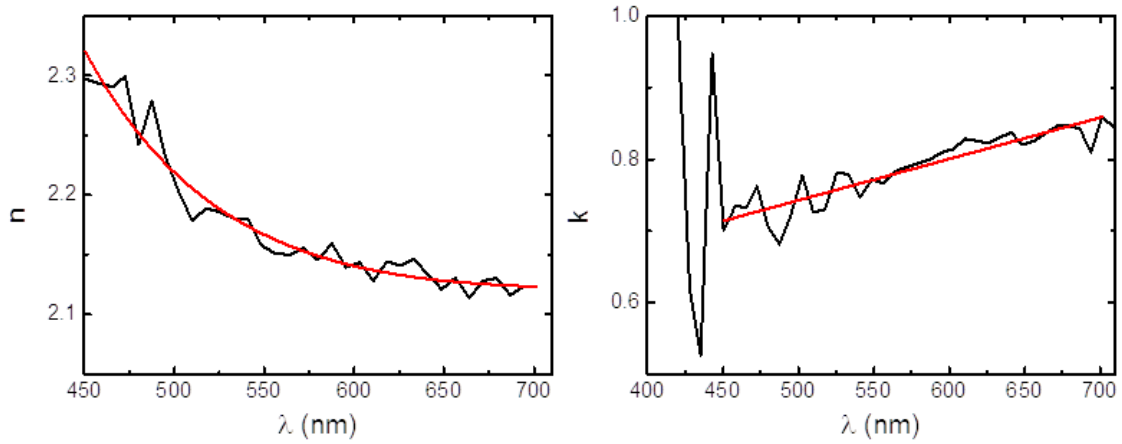


Figure 2.2: Averaged refractive index of $\text{Ca}_3\text{Ru}_2\text{O}_7$. Left: Real index.

Right: Imaginary index. Black curve: averaged data. Red curve: Fitted line.

Fitted Parameter:

Real: Cauchy's equation $n(\lambda) = \frac{A}{\lambda^2} + \frac{B}{\lambda^4} + \frac{C}{\lambda^6} + D$, wavelength in micrometers

Imaginary: $k(\lambda) = m \cdot \lambda + b$

| Parameter | A | B | C | D | m | b |
|-----------|---------|--------|---------|--------|--------|--------|
| Value | -0.0034 | 0.0554 | -0.1911 | 2.3141 | 0.5775 | 0.4539 |

Table 2.1: Fitting parameters of refractive index of $\text{Ca}_3\text{Ru}_2\text{O}_7$

Transfer matrix method:

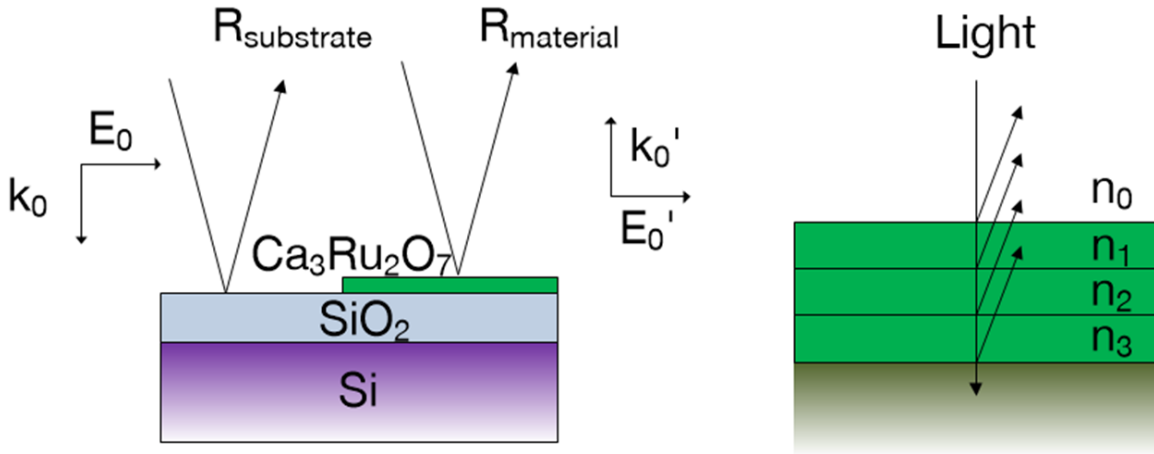


Figure 2.3: Idea of the reflection contrast. Left: The contrast is the difference between reflectivity on SiO_2 (substrate) and $\text{Ca}_3\text{Ru}_2\text{O}_7$ (material). Here k_0 is the wave vector of the incident light and the k_0' is the reflected light. Right: The reflectivity is calculated on every interface of different materials.

The calculation of reflectivity from transfer matrix method is based on the continuous condition of E-M fields at the interface of material n_0 and n_1 . The equation can be written as:

$$E_0 + E_0' = E_1 + E_1'$$

$$H_0 - H_0' = H_1 - H_1'$$

$$n_0 E_0 - n_0 E_0' = n_1 E_1 - n_1 E_1'$$

The first equation is from the continuity of the electric field, and the second is the same from magnetic field. By applying the condition of Fresnel equations $H = n^*E/c$ on the second equation we get the third equation. When the light travels through next layer it

picks up a phase $k_i d_i = \frac{2\pi n_i d_i}{\lambda}$, assuming the next layer to n_1 is semi-infinite denoted as

“T”, the boundary condition is:

$$\begin{aligned} E_1 e^{ikd_1} + E_1' e^{-ikd_1} &= E_T \\ n_0 E_0 e^{ikd_1} - n_1 E_1' e^{-ikd_1} &= n_T E_T \end{aligned}$$

By solving the equations with the matrix method, we get the r and t as the ratio of reflected and transmitted electric field to the incident field:

$$\begin{aligned} 1 + \frac{E_0'}{E_0} &= (\cos(kd_1) - i \frac{n_T}{n_1} \sin(kd_1)) \frac{E_T}{E_0} \\ n_0 - n_0 \frac{E_0'}{E_0} &= (i \frac{n_T}{n_1} \sin(kd_1) + n_T \cos(kd_1)) \frac{E_T}{E_0} \\ \begin{bmatrix} 1 \\ n_0 \end{bmatrix} + \begin{bmatrix} 1 \\ -n_0 \end{bmatrix} \frac{E_0'}{E_0} &= \begin{bmatrix} \cos(k_1 d_1) & -i \sin(k_1 d_1) / n_1 \\ -i \sin(k_1 d_1) / n_1 & \cos(k_1 d_1) \end{bmatrix} \begin{bmatrix} 1 \\ n_T \end{bmatrix} \frac{E_T}{E_0} \\ \begin{bmatrix} 1 \\ n_0 \end{bmatrix} + \begin{bmatrix} 1 \\ -n_0 \end{bmatrix} r &= \begin{bmatrix} \cos(k_1 d_1) & -i \sin(k_1 d_1) / n_1 \\ -i \sin(k_1 d_1) / n_1 & \cos(k_1 d_1) \end{bmatrix} \begin{bmatrix} 1 \\ n_T \end{bmatrix} t \end{aligned}$$

We define the transfer matrix M here since the same equation applies to the next layer, M will be a product of a series of matrixes.

$$\begin{aligned} M_i &= \begin{bmatrix} \cos(k_i d_i) & -i \sin(k_i d_i) / n_i \\ -i \sin(k_i d_i) / n_i & \cos(k_i d_i) \end{bmatrix} \\ M &= \prod M_i \end{aligned}$$

The final reflectivity = $|r|^2$ can be solved by the matrix element of M:

$$\begin{aligned} \begin{bmatrix} 1 \\ n_0 \end{bmatrix} + \begin{bmatrix} 1 \\ -n_0 \end{bmatrix} r &= M \begin{bmatrix} 1 \\ n_T \end{bmatrix} t = \begin{bmatrix} A & B \\ C & D \end{bmatrix} \begin{bmatrix} 1 \\ n_T \end{bmatrix} t \\ r &= \frac{An_0 + Bn_T n_0 - C - Dn_T}{An_0 + Bn_T n_0 + C + Dn_T} \\ R &= |r|^2 \\ C &= \frac{R_{material} - R_{substrate}}{R_{material} + R_{substrate}} \end{aligned}$$

Here C is the Michelson's contrast.

Applying the refractive index of silicon and silicon dioxide, and the $\text{Ca}_3\text{Ru}_2\text{O}_7$ measured previously, we get the R and C as a function of layers and wavelength. The result is presented in Figure 2.4 and Figure 2.5.

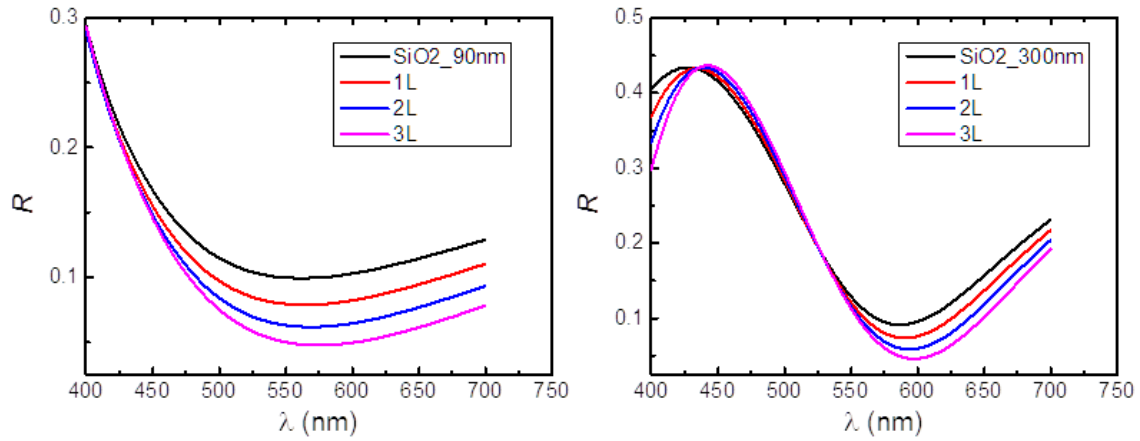


Figure 2.4: Simulated reflectivity of $\text{Ca}_3\text{Ru}_2\text{O}_7$ few layers on SiO_2/Si substrate. Left: SiO_2 90nm. Right: SiO_2 300nm. The single bi-layer $\text{Ca}_3\text{Ru}_2\text{O}_7$ thickness is assumed to be 0.977 nm that is half of the lattice parameter c because each unit cell contains 2 layers.

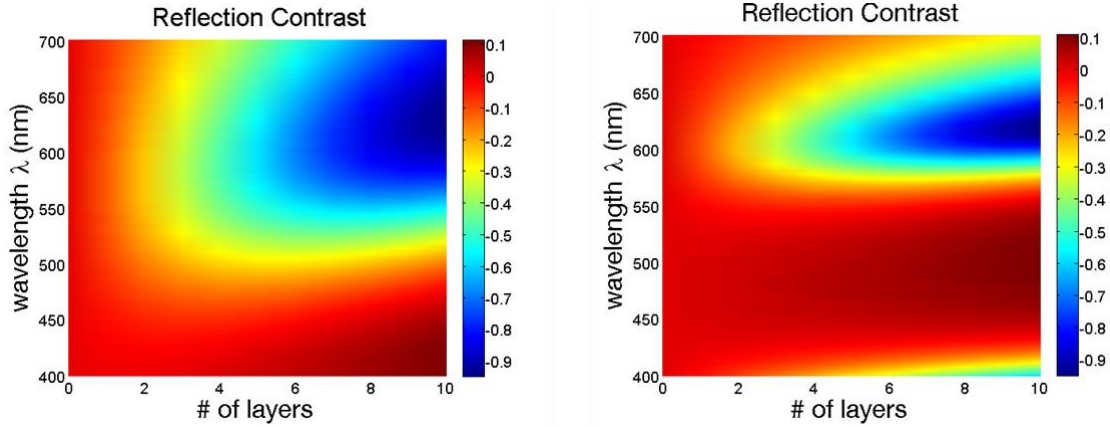


Figure 2.5: Simulated reflectivity contrast for 10 layers of $\text{Ca}_3\text{Ru}_2\text{O}_7$ on top of SiO_2/Si substrates. Left: SiO_2 90nm Right: SiO_2 300nm

$$C = \frac{R_{\text{material}} - R_{\text{substrate}}}{R_{\text{material}} + R_{\text{substrate}}}$$

From the results, we obtain the contrast C larger than 5% (0.05) on both substrates with few-layer flakes around 550nm indicating it is possible to see them with eyes. And 90 nm SiO_2 substrates have better contrast ratio over 300 nm SiO_2 . The flake will appear darker on the substrate in the visible wavelength.

2.2 Atomic force microscopy

The thickness of flakes is measured with the atomic force microscopes (AFM) because it is almost the only way to determine the thickness of micrometer-sized flakes with nm-precision with reasonable efficiency. There are several different operating options of AFM, and we will just briefly introduce the tapping mode AFM which we use for our measurement. The basic working principle, as depicted in Figure 2.6, is sensing the tiny height differences on the surface with an oscillating tip. While the tip is oscillating at its resonant frequency, the frequency and the amplitude of the tapping tip would be sensitive to the weak attraction force between the tip and the surface, and the

force would be stronger in the higher area (closer to the tip). By shining laser on the back of the tip and detecting the reflected signal with optical sensors, it would be possible to determine the height difference to atomic level (~ 0.1 nm) at the optimal condition. There is a piezo stage drags the tip in one direction for a linear scan, and multiple linear scans compose a complete area scan of the surface. We use both a digital instrument DI-3100 AFM and an Asylum-Cypher AFM.

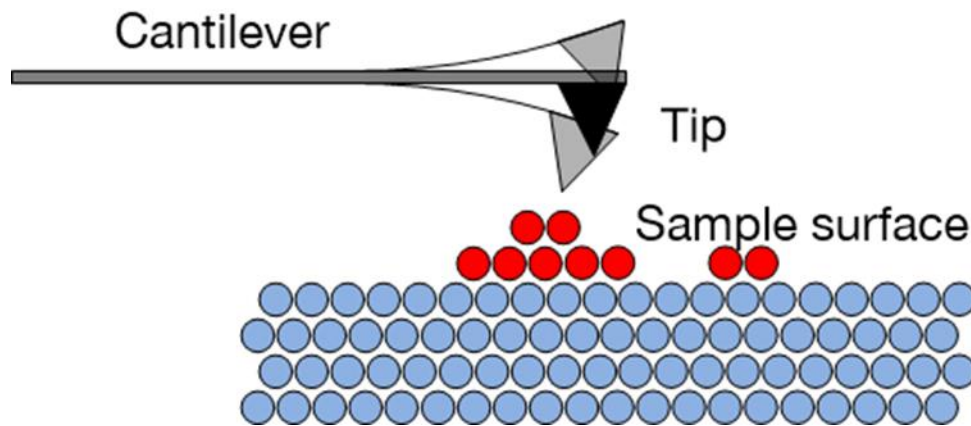


Figure 2.6: AFM tapping mode. The tapping tip on the flapping cantilever measures the height profile of a sample (red) on a substrate (blue)

The most important (and the most consumed) part of the scanning is the tip. Choosing an appropriate tip from multiple options may take some basic knowledge. If there is no specific need (magnetic force, conductive or insulator) usually people choose Si tip because it is cheap and available from most of the suppliers. The Si tip is etched to reach the sharpness about 10nm that is enough for most of the application. The force constant (of bending the cantilever) is particularly important for contact mode scan of tiny features which requires the cantilever to be as soft as ~ 0.1 N/m, so usually the cantilever is very long. For tapping mode the force constant is much larger, around several tens of N/m and the cantilever is much shorter.

The most problems we face when scanning AFM is usually the artifacts. In Figure 2.7 three kinds of artifacts are shown with real examples. (a,b) is the double-image problem created by two peaks on the tip because both of them can sense the surface and the outcome is the superposition of the two images. The distance between the two images is the distance between the two peaks on the tip. Usually this effect happens with a damaged tip after repeatedly scanning of rough surface or steep high edges. In (c) the interference pattern shows up on the graph as a false signal since it is not related to any height information. Because we use laser beam to probe the oscillation of the tip, and it is quite closed to the sample surface, thus the ring or stripe patterns generated by interference between incident and reflected laser light takes place frequently. The solution to this problem is re-adjusting the tip and laser position so that the tip can block the laser spot better, preventing the reflection of laser from sample surface. (d) The effect of dull tips which makes all small dots on the graph look the same weird pattern like the “c” in the example. Sometimes it can be a triangular pattern or even more irregular shapes. The origin of this artifact is the tip being worn out and unable to sense features smaller than the tip size, so the feature will look all the same as the shape of the tip. Overall, being cautious about the tip status and watch out for the artifact of the scanned image is the key to make successful AFM scans.

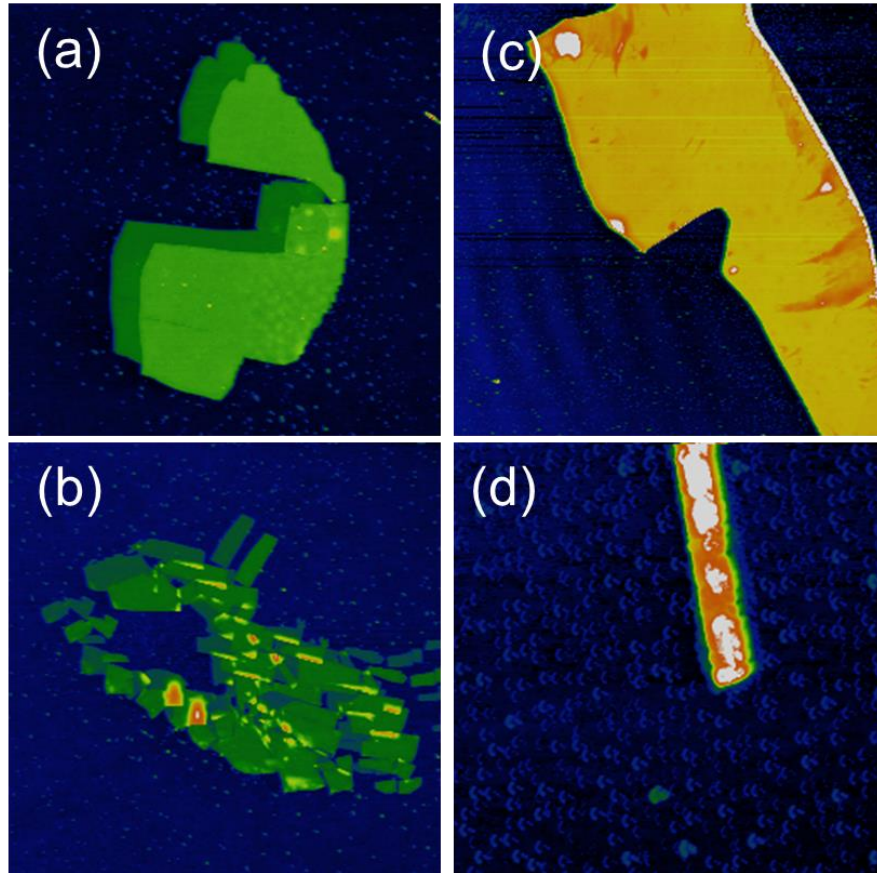


Figure 2.7: Several examples of common problems in AFM scanning. (a,b) The “shifted” image indicates there are two peaks on a single tip both scanning the feature and generate duplicated images. The images are $\text{Ca}_3\text{Ru}_2\text{O}_7$ exfoliated flakes on SiO_2/Si substrates. (c) Interference pattern in AFM scanning. The blue-black stripes on the lower-left of the image is a false signal induced by the interference pattern on the sample. The scanned item is a FeTe exfoliated flake. And many “scar” features are also presented on the upper-middle part. (d) The effect of dull-tip making all small dot looks like a “c”.

Once the data is taken, analyzing the AFM graph is also an important part. Since when the AFM tip hits a bad spot, it ruins the rest part of a single line scan leaving a scar-

like feature on the graph. And the height reference point may differ between different line scans and the whole surface may be inclined to a direction. In this case, we first remove the scars by replacing the ruined part with the two adjacent lines, and then flatten the whole image by applying a linear correction to every line scan so that the height references are the same on our assigned line/surface which we assume is flat (usually the plain SiO₂ surface without flakes/glue spots). The work mention above is done by DI analyze software or an open-source software Gwyddion.

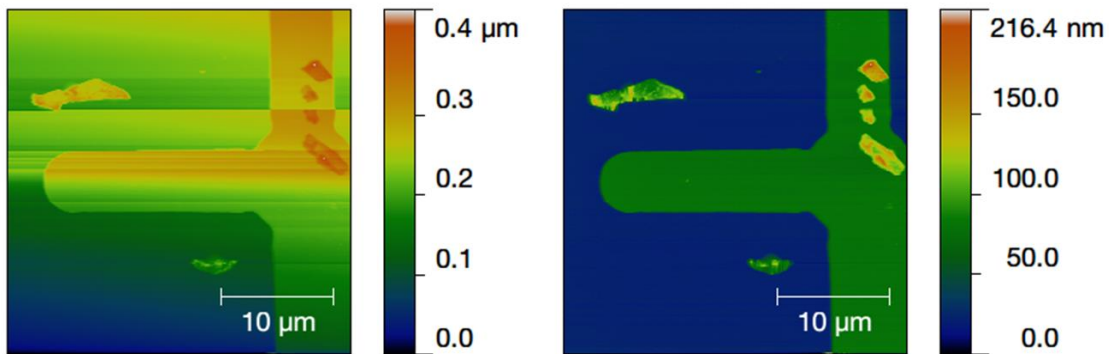


Figure 2.8: Flattening the AFM image by data processing. The raw scan data on the left is a cross-bar marker fabricated on the SiO₂/Si substrate with some small flakes around. The height reference jumped off between some sections. After the flattening and removal of scar the essential information of the graph becomes clear.

2.3 Scanning electron microscopy

There are two applications of SEM in our projects. One is to investigate the details of broken devices since SEM scanning is much faster than AFM when we don't need thickness information on the surface and the other is to utilize e-beam lithography which will be introduced in the next chapter. Here we just briefly discuss the working

principle of SEM. A SEM consists of several parts: beam emitter, condenser lens, deflection lens and detectors. Electron beams are generated from the beam emitter and accelerated up to 15~30 keV in the high vacuum, passing through the condenser lens and condensed onto a very narrow spot, typically ~10 nm in the lateral dimension or less. And the deflection lens control the direction of the focused electron beam to scan the surface. Finally the scattered electrons are picked up by the detector for imaging.

There are mainly two kinds of beam emitter: thermal filament and field emission (FE). The thermal filament is heated up by a large electrical current so that some electrons can overcome the energy barrier to escape the surface by absorbing thermal energy. A FE type electron source is usually a sharp tip for creating a large local field on the tip so that some electrons can be pulled out directly by the field. Thermal filament features a more stable emission current so it is usually used for e-beam lithography which requires a precise beam current control and FE is much faster in turning on/off so it is better for imaging. But currently FE can be controlled quite stable as well so there are also FE type SEMs used for e-beam lithography. Since the electron carries charge, so the movement can be controlled with electromagnetic fields. Condenser lens is composed of a series of coils and plates generating EM fields for focusing the electron beams, and deflection lens apply usually just electric field to shift the beam spot on the surface.

When the accelerated electrons with the kinetic energy on the order of 10 keV hit the surface, all of the inner orbital electrons of atoms on the surface will be knocked out because the binding energies are just on the order of 10 eV. Low energy x-rays will be produced with the recombination of these electrons and collecting the x-ray spectra helps analyzing the elemental composition of the sample (EDX). Most of high energy electrons

are bounced back without much loss of energy, usually called backscattered electrons (BSE), while some of them penetrate deeper, keeping knocking out more electrons from the material called secondary electrons (SE). Typical SEMs have both kinds of detectors for BSE and SE, while the SE detectors are commonly used for imaging because SE reveals more details in the scanning.

Aside from imaging the surface, SEM can control the position and on/off of the focused e-beam to “write” a pre-programed pattern on the sample. This is the basic concept of the e-beam lithography and the details will be introduced in the device fabrication process.

We have used a Hitachi SU-4700 SEM (FE) for imaging and EDX analysis, a JEOL 840A (Thermal filament) and a Hitachi SU-5000 SEM (FE) for e-beam lithography.

2.4 Raman spectroscopy

Probing the structural change of tiny exfoliated flakes with Raman spectroscopy has been a common method since the graphene is found to have significant peak shift below 5 layers³⁷. Because the method is fast and does not require extra process or treatment on the flakes. In our case, though we did not see significant shift from the thin flakes of $\text{Ca}_3\text{Ru}_2\text{O}_7$ ~10 nm and the signal from the thinner flakes are too weak to detect, it still gives us some indication that the flakes keep the similar structure at this thickness. For Fe_{1+y}Te flakes it is too difficult to have an uncontaminated spectrum since they oxidize quickly both in air and under strong irradiation.

To explain the Raman effect in one sentence, it is the inelastic scattering of light by lattices creating/annihilating normal mode phonons. Classically, it can be written in the form of an oscillating electric field driving the polarization of the material. Suppose

the frequency of the field is ν_0 , the normal mode frequency is ν_m , for a non-zero polarizability change $\left(\frac{\partial\alpha}{\partial q}\right)_0$ we will have the emitted light from the oscillation of polarization at frequency $\nu_0 + \nu_m$ and $\nu_0 - \nu_m$ as shown in the follow:

$$\begin{aligned}
E &= E_0 \cos(2\pi\nu_0 t) \\
P &= \alpha E = \alpha E_0 \cos(2\pi\nu_0 t) \\
q &= q_0 \cos(2\pi\nu_m t) \\
\alpha &= \alpha_0 + \left(\frac{\partial\alpha}{\partial q}\right)_0 q \\
P &= \alpha_0 E_0 \cos(2\pi\nu_0 t) + \left(\frac{\partial\alpha}{\partial q}\right)_0 E_0 q_0 \cos(2\pi\nu_m t) \cos(2\pi\nu_0 t) \\
&= \alpha_0 E_0 \cos(2\pi\nu_0 t) + \left(\frac{\partial\alpha}{\partial q}\right)_0 E_0 q_0 [\cos(2\pi((\nu_0 + \nu_m)t) + \cos(2\pi(\nu_0 - \nu_m)t)]
\end{aligned}$$

We call the “-” peak “Stokes” and the “+” as the “anti-Stokes”. The light with original frequency is called Rayleigh-scattered light.

Classical model gives the right frequency of the Raman scattered light, but fails to describe the correct ratio of intensity between Stokes and anti-Stokes. This is because of the quantum nature of the light (photon) and the oscillation (phonon). Consider n phonons in a quadratic potential well $V = \frac{m\omega^2}{2} x^2$ in which $E = \hbar\omega(n + \frac{1}{2})$, the excitation of light is $H_E = E_0 x$ since the wavelength of light is way longer than the lattice constant. From the transition matrix element calculated in basic quantum mechanics we know this Hamiltonian can only increase/decrease n by one. The result corresponds to Stokes/anti-Stokes processes mentioned above. The intensity of Stokes and anti-Stokes peaks can be estimated with the energy (frequency) difference and temperature because phonons are bosons:

$$\frac{I_{AS}}{I_S} \propto \frac{\omega_{AS}^3}{\omega_S^3} e^{-\frac{\Delta E}{k_B T^*}}$$

We plot the energy level diagram of phonons and the a real spectrum containing both Stokes and anti-Stokes peaks in Figure 2.9.

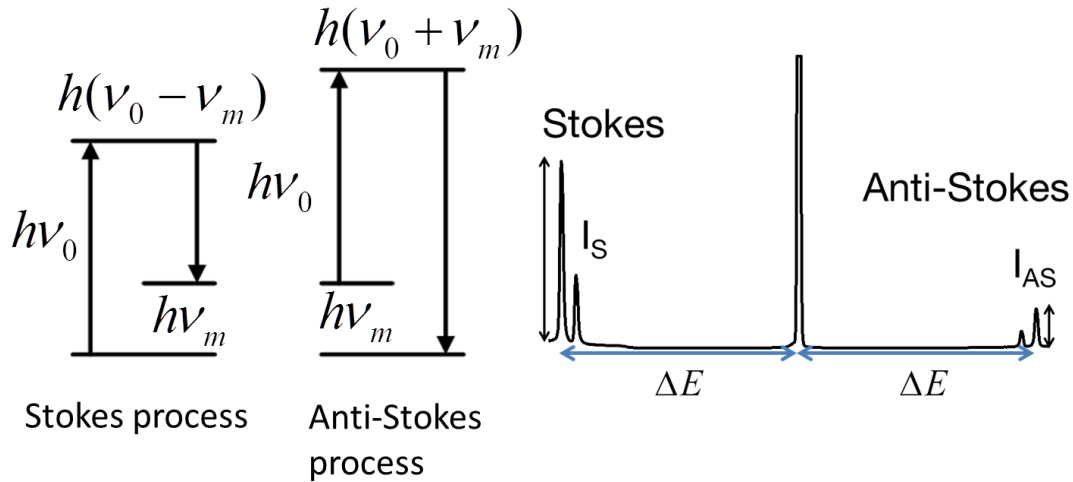


Figure 2.9: The Stokes/anti-Stokes process. Left: The energy level diagram of the Raman scattering. Right: the actual spectrum of Raman spectroscopy and the central peak is the laser excitation.

In practical, we use reflective micro-Raman spectroscopy for detecting signals from the exfoliated flakes on SiO₂/Si substrates. The idea is illustrated in the following picture. Flakes are found under an optical microscope using a 100X objective and laser is sent through the objective to excite the flakes. We select a certain polarization of analyzer from the reflected light mixing Raman signals and Rayleigh-scattered light and then block the latter by a notch filter designed to extinguish the light within a very narrow wavelength region since the signal of Raman signals is much weaker (typically 10⁻⁶ in ratio) and cannot be seen without reducing the strength of Rayleigh-scattered light. In

order to suppress exactly at the laser wavelength, a notch filter is put right in front of the detector. A diagram of typical Raman spectroscopy setup is plotted in Figure 2.10.

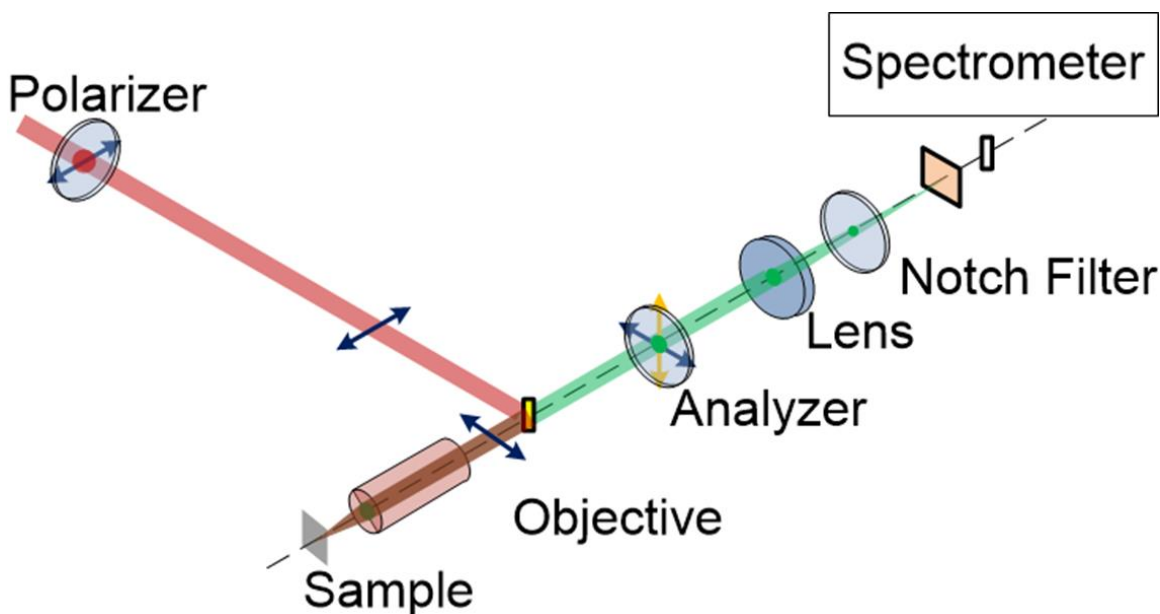


Figure 2.10: The experimental setup of Raman spectroscopy. Usually 100X objective is used for small samples. The polarizer and analyzer select the polarization of exciting laser and scattered Raman signal. Red light (deeper) is the incident laser, reflected by a small mirror (or a beam splitter) and focus on the sample through a microscope objective.

In commercial Raman instruments sometimes there is no analyzer available so we have plenty of Raman spectra without selection of polarization. The laser source is 532nm Nd-YAG laser producing power on the order of mW. Heating effect is observed usually with the power over 10 mW (depends on thickness, size and thermal conductivity of the flake) so at room temperature the power is limited as small as possible around 1~3mW when collecting the data.

Chapter 3

Preparation of devices

As a member of layered structured material, $\text{Ca}_3\text{Ru}_2\text{O}_7$ in principle could be mechanically exfoliated into thin flakes containing only few atomic layers as well, but due to the CaO structure formed between RuO_6 octahedral and Ca ions, the layer-layer ionic binding force inside the material is much stronger than graphite (that has van der Waals force) so that exfoliation cannot be carried out easily. In the early studies researchers found the typical exfoliation method (scotch tape) generates “flakes” with the thickness on the order of micrometers and the minimum thickness they can find is about 330 nm^{38} , which is apparently not thin enough for any possible transition triggered by reduction of dimensionality.

In the beginning of this project, our group had tried several methods to exfoliate the crystal. We tried scribing SiO_2/Si substrates with crystal edges hoping the thin flakes to fall off on the substrates. But it only generates traces which can hardly be distinguished as the material because they look just like powder and lack characteristic Raman peaks, also it cannot be used for device fabrication because the size is too small and the surface is not flat. We also tried adding $\text{Ca}_3\text{Ru}_2\text{O}_7$ powder into IPA, sonicate it for several hours and centrifuge the solution, hoping the sonication knocks off some floating flakes in the solution and we can collect them by dipping a drop of solution on SiO_2/Si substrates and blow-dry. It turns out that there are rarely some tiny pieces with thickness around few nanometers which can be found by AFM scanning, and they are too small to be observed

under optical microscopes. Further characterization to verify if they are really $\text{Ca}_3\text{Ru}_2\text{O}_7$ is not possible either because of the size of the flakes.

To deal with this problem, I invented a method which turns the mechanical exfoliation process of few-nanometer-thick flakes possible with $\text{Ca}_3\text{Ru}_2\text{O}_7$ and it is also applicable for other “hard” layer-structured materials. The basic idea of this method is as follows. First, fix the ab-plane of a crystal on a flat surface by strong glue, and then glue the other parallel side of the crystal on a top lid. After the glue is totally cured, we crack the crystal along ab-plane by levitating the top lid. The newly generated surface of the crystal contains a lot of loosely-connected flakes that can be easily picked up by scotch tape and transferred onto SiO_2/Si substrates. The method can be applied repeatedly on the newly cracked crystals until they are too thin to be cracked uniformly.

The exfoliated flakes in large sizes can be characterized in the ways mentioned in previous chapters. Later on they can be made into devices with gold electrodes by e-beam lithography for electrical transport measurement in the Quantum Design Physical Property Measurement Systems (PPMS). During the fabrication process, I have encountered many problems, such as bad contact resistance, the static charge burns the device instantly when it connected with the probes, the ionic liquid dispersed away and etched the device, etc. Details of exfoliation, device fabrication and resistance measurement, including ionic liquid gating will be explained in this chapter. Section 3.1 and 3.2 will cover the preparation of substrates and the method of exfoliation. E-beam lithography procedures are described in Section 3.3. Problems with contact resistance are explained in Section 3.5. And finally the idea and the test results with ionic liquid gating are presented in Section 3.6.

3.1 Preparation of substrates

Before we exfoliate flakes onto the substrates, by learning the wisdom of development of 2D material research we know that without proper label or coordinate it will be extremely hard to find the same micrometer-wide flakes on a centimeter-wide substrate repeatedly for characterization and device fabrication purposes. To define the position of flakes on substrates, we need to pre-pattern the substrates and clean them before use. Besides the coordinates, we also want to make some large contact pads to save e-beam writing time and use them for potential ionic-liquid gating purposes.

The substrates used for exfoliation are prepared from SiO₂ 90 or 300 nm /Si wafer (100) purchased from Graphene Supermarket. There are plenty of suppliers of this kind of wafers and we pick up this just for convenience reason. The pre-made coordinates together with large contact pads (200x100 μm²) are made by photolithography and thermal evaporation. First the SiO₂/Si wafer is spin-coated with S1813 photoresist at 3000 rpm for 40 seconds and baked at 95°C in oven for 30 minutes. After that the wafer is exposed to UV under a designed chromium-quartz mask, fabricated by Photo Science Inc., for the desired pattern and developed/rinsed with MF-319 developer/DI water 30sec/30sec. The patterned wafer would be then transferred into the thermal evaporator chamber. Ti/Au thin film with thickness 3/60 nm in high vacuum ($\sim 10^{-7}$ Torr) is deposited and lifted off in warm acetone with slight sonication. Fabricated wafers finally are covered by S1813 and baked again for protection and sliced into 8x8mm pieces by a digitalized dicing saw. The design and fabricated chip outlook are presented in Figure 3.1.

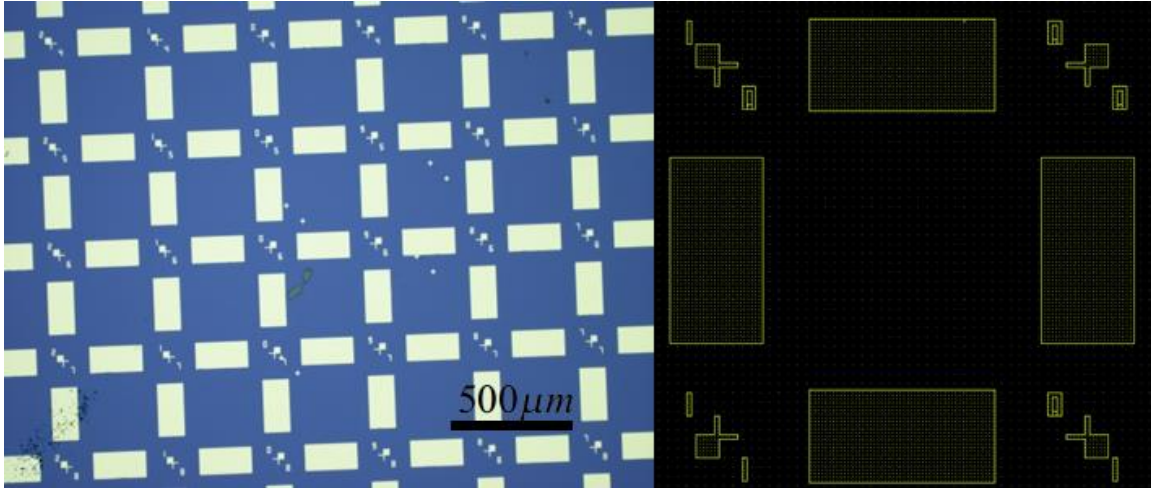


Figure 3.1: The substrate design. Left: 5X optical image of substrate (with some exfoliated flakes) yellow rectangle blocks and coordinates are patterned and deposited with Ti/Au thin films. Right: Design of coordinates and contact pads. The crosses with blocks denotes different four areas on the substrate avoiding confusing recurring coordinates.

There are two cleaning procedures for the patterned substrates. One is called “solution clean” by soaking the substrates first in warm acetone for 5 minutes to remove the photoresist protection layer and rinsed in IPA (isopropanol), followed by blow-dry IPA with nitrogen gun. And the other is the RCA clean which takes much longer time (in deed it is the second step of a complete RCA clean of Si wafer without piranha step). The procedure starts from soaking the chips in the 1:1:5 H_2O_2 (~25%): NH_4OH (~30%): H_2O (ratio in volume) and heat up to 70°C for 30 minutes, rinse in DI water, blow-dry. The H_2O_2 should be a fresh bottle or it will not be effective after opened and kept in refrigerator 24 hours or at room temperature 30 minutes. Solution clean + RCA clean are recommended to improve flake-substrate attachment and increase the exfoliation yield, and they usually works better for Fe_{1+y}Te , $\text{Fe}(\text{Se},\text{Te})$ and graphene exfoliation. For

exfoliation of $\text{Ca}_3\text{Ru}_2\text{O}_7$ flakes solution clean is good enough. The final step is to put the substrate in the plasma chamber, pump down below 60mTorr, and clean the substrates with oxygen plasma at pressure around 500 mTorr and with power = 300W for 2 minutes. After cleaning, the substrates should be used in exfoliation within a day to avoid contamination by exposing them in the air for too long.

3.2 Exfoliation (Gorilla glue method)

The basic idea of this method is to fix the bulk crystal on both sides of ab-plane with two pieces of microscope slides, and then cleave the crystal by pulling the two slides apart. To fix a few-millimeter piece of $\text{Ca}_3\text{Ru}_2\text{O}_7$ crystal we use Gorilla glue which cures with moisture and glue the ab-plane side of the crystal on a microscope slide. The process takes 2-3 hours. Until the glue is fully dried, we use another microscope slide with Gorilla glue to cap the other side of the crystal. To ensure the flat contact between the crystal and the microscope slide, a small C-clamp is applied over the sandwich and folded tissue is filled on both sides of the microscope slides avoiding tilted contact. The setup is drawn in Figure 3.2 with a picture of a real example. After another 2-3 hours we can break the crystal by levitating the slide so that the crystal breaks through the ab-plane. Crystal flakes can be then exfoliated by pressing scotch tape over the broken surface and then transferred onto pre-cleaned SiO_2/Si substrates. The schematics of the process are shown in Figure 3.3. After exfoliation, the substrates are put into oxygen plasma chamber to clean up the tape residue since $\text{Ca}_3\text{Ru}_2\text{O}_7$ does not oxidized so it can survive the oxygen plasma and the substrates are examined under a high magnification optical microscope for flakes with micrometer size.

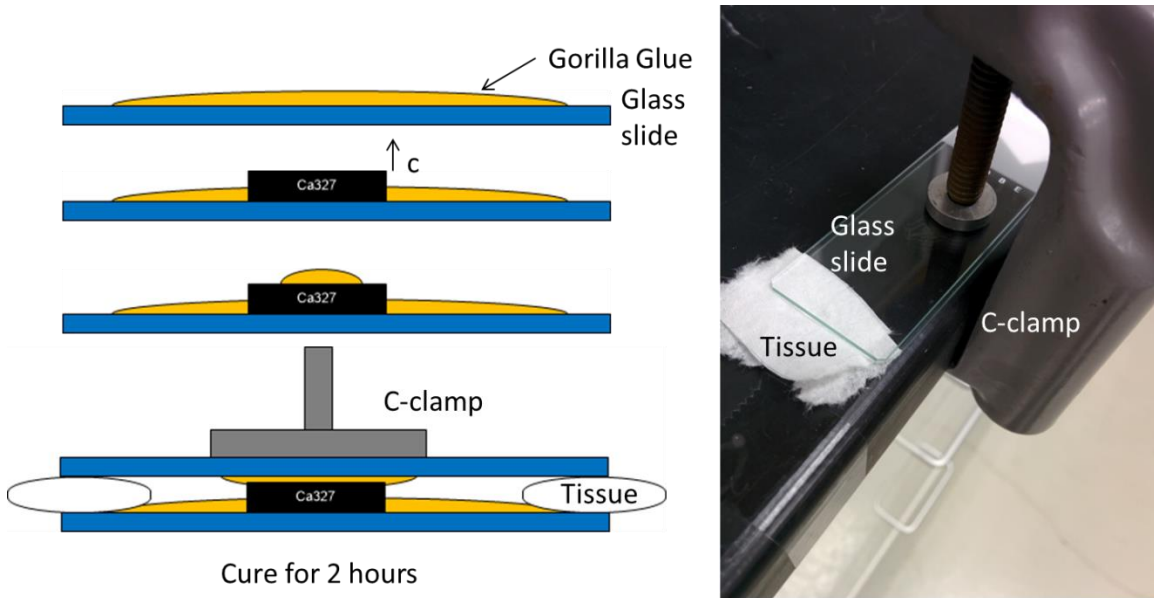


Figure 3.2: Setup to crack the crystal along the direction of ab-plane. Left: the procedures of fixing the $\text{Ca}_3\text{Ru}_2\text{O}_7$ crystal on microslides. (from top to bottom) Right: a picture of actual setup, tools used in procedures are labeled with their names.

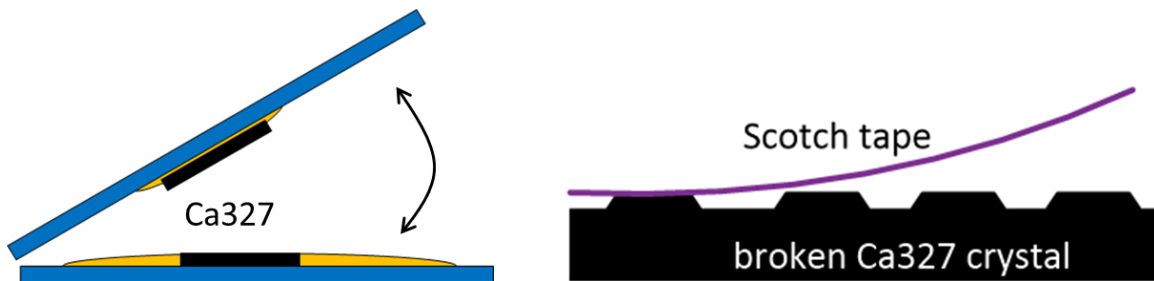


Figure 3.3: Collecting flakes from broken crystal. After the glue is cured, the crystal is broken through the layer direction and flakes can be collected using Scotch tape method on the broken plane of crystal.

The example of typical substrate surfaces are in Figure 3.4. Tanned colored big flakes are usually much thicker than 100 nm, and we are focusing on blue or dark colored small flakes. Usually few flakes on the order 20-100 nm could be found in a good-split sample. But the method depends heavily on the cleaved surface quality. If the broken

surface is flat and shiny which usually indicates a nice ab-plane cleavage, we can get many useful flakes, and the cracked crystals can be glued and split again. If this is not the case, nearly no useful flakes (under 100nm) can be found in the exfoliated samples and crushing away the residue glue/bad surface with razor blades gives little hopes on making another good split.

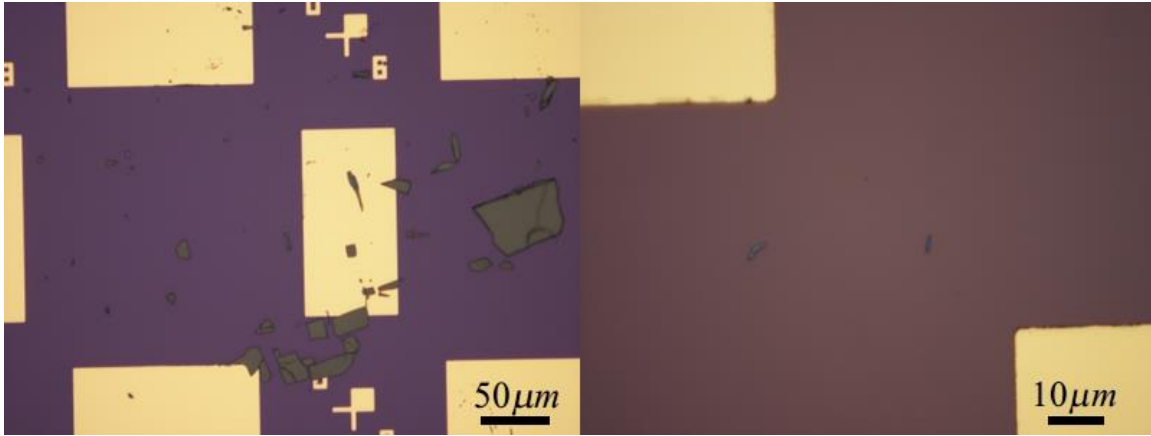


Figure 3.4: Examples of exfoliated flakes. Left: Typical exfoliation of large blocks of $\text{Ca}_3\text{Ru}_2\text{O}_7$, thickness ranging from several hundred nm to few micrometers. Right: Few flakes can be sometimes found nearby large blocks, the thickness of the smaller one is about 30 nm for example.

3.3 E-beam lithography

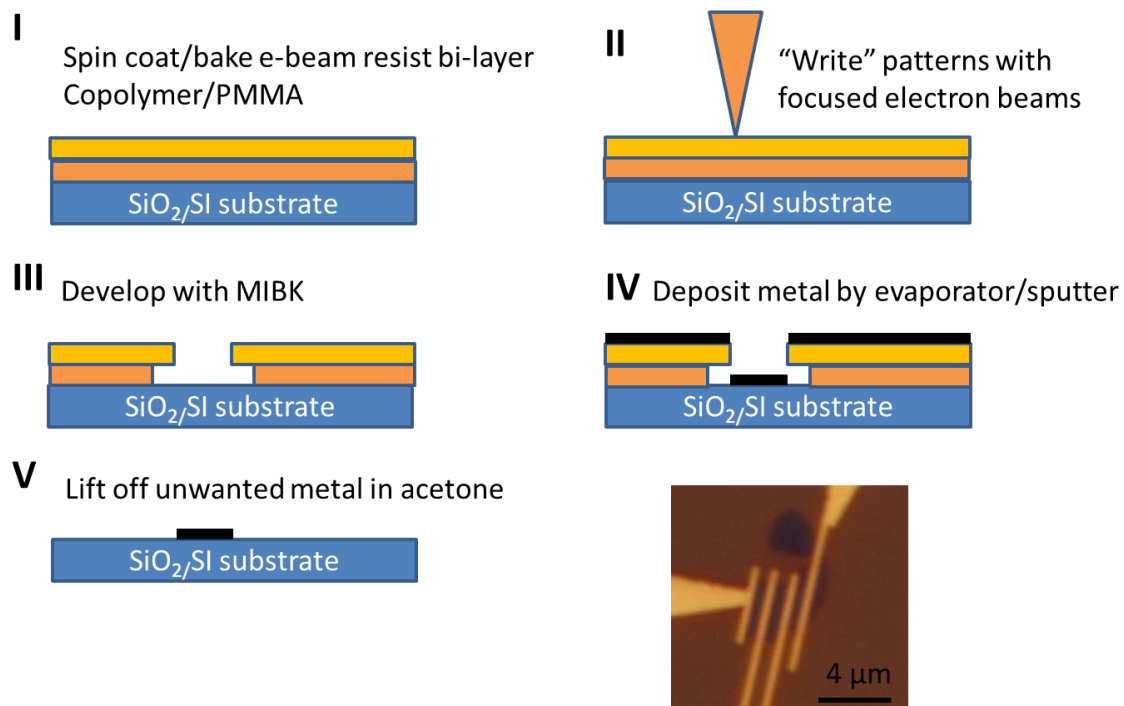


Figure 3.5: The workflow of e-beam lithography. The process follows the number of the diagram and the last one is an optical image of fabricated device based on a 20 nm $\text{Ca}_3\text{Ru}_2\text{O}_7$ flake. The orange layers stand for e-beam resist mentioned in the main text and the black layer stands for metal.

E-beam lithography is a necessary step in order to lay sub-micrometer electrodes on the exfoliated flakes. The work flow is explained in Figure 3.5. First the substrates are spin-coated with bi-layer e-beam resist MMA/MAA EL9 and PMMA C2, both with rotation speed 4000rpm and baking condition 180°C on a hot plate for 90 seconds. Bi-layer coating is chosen because the advantage of easy liftoff which make less harm to the flakes. Then the substrates are sent into a Joel-840 (thermal filament) or Hitachi SU-5000 (Field-emission) SEM. Electron beams are accelerated and focused on the desired region to “write” designed patterns by modifying chemical structure of the e-beam resist so that

it becomes soluble in the developer MIBK. Then the sample will be deposited with material by evaporation or sputtering, and lift-off in warm acetone for 10~15 minutes following by IPA rinse and blow-dry. Acetone flushing and light sonication will be used if the film is not lifted-off automatically.

The devices fabricated in the dissertation consist of four electrodes on a flake and a top gate nearby the flake but not in contact with the flake and other electrodes. The fabrication process includes putting alignment marks, designing the electrodes, writing and development, deposition and lift-off. On some devices we have SiO rings over the device.

Alignment marks are written nearby the sample by referencing the optical images and the pre-made coordinates on the substrates. Usually two crosses defining an area about $80 \times 80 \mu\text{m}^2$ are written near a flake. In some cases alignment marks will be put a bit away from the flake to get avoid of pre-made coordinates and contact pads. Ti(2nm)/Au(60nm) thin film is deposited by thermal evaporation which is also used for coordinates on the substrates. See Figure 3.6 for the developed align mark pattern and the finished ones.

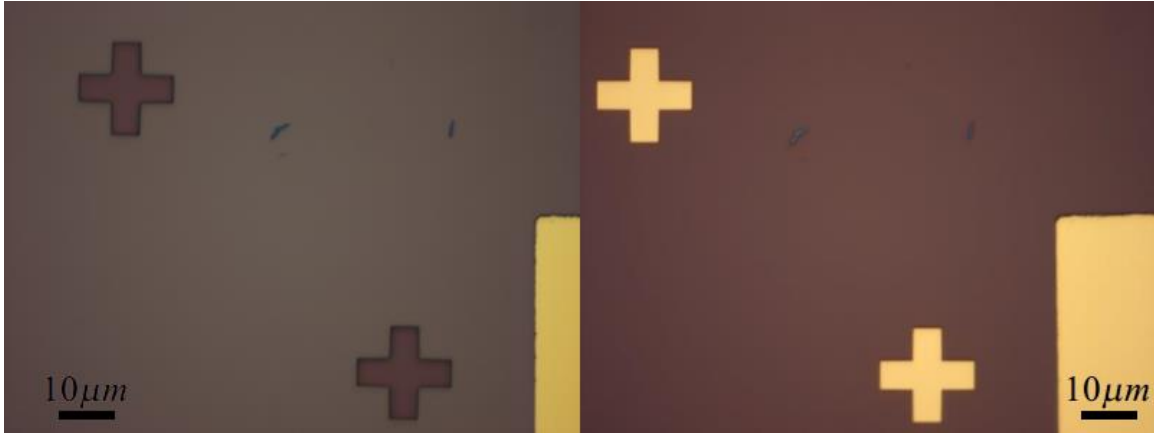


Figure 3.6: Alignment marks for e-beam lithography. Left: Developed e-beam resist mask for deposition. Right: finished alignment marks. Both images are taken under a 100X microscope objective.

Electrodes are designed to connect the large pre-made contact pads to the flakes; the actual process is carried out with the software Design CAD and Microsoft PowerPoint. Patterns drawn with Design CAD can be pasted onto the optical image in PowerPoint with appropriate sizing and alignment with the marks to see if the electrodes will be connecting the flake and the contact pads (See Figure 3.7). In real writing procedures the patterns are aligned by matching the alignment marks in design and the actual marks fabricated on substrates from the previous step. Two-step writing at 500X and 100X covers up a region $\sim 800 \mu\text{m} \times 800 \mu\text{m}$ without losing resolution for fine patterns. For 100X writing, the aperture is opened up for larger writing current yielding less writing time when using JEOL SEM.

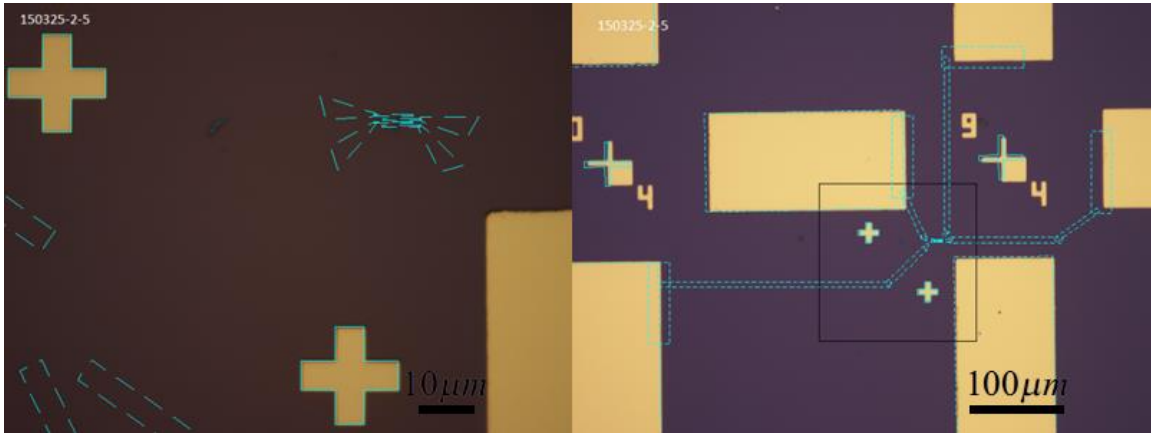


Figure 3.7: Matching designed patterns with optical images. Blue dashed lines are pasted onto the image from Design CAD. Left: 100X Right: 20X optical images.

Ni(10nm)/Au(100nm) deposition by sputtering is the best for the device since the adhesion is better and also the contact resistance is reasonable (few $k\Omega$). Ti(3nm)/Au(100nm) has been tried a lot before on $\text{Ca}_3\text{Ru}_2\text{O}_7$ but the contact resistance is usually too big for measurement and sometimes random (several 10k to $M\Omega$). Au(100nm) only gives reasonable contact resistance but bad adhesion that sometimes won't survive lift-off and get broken with ionic liquid easily. An example of the developed pattern to finished device is in Figure 3.8.

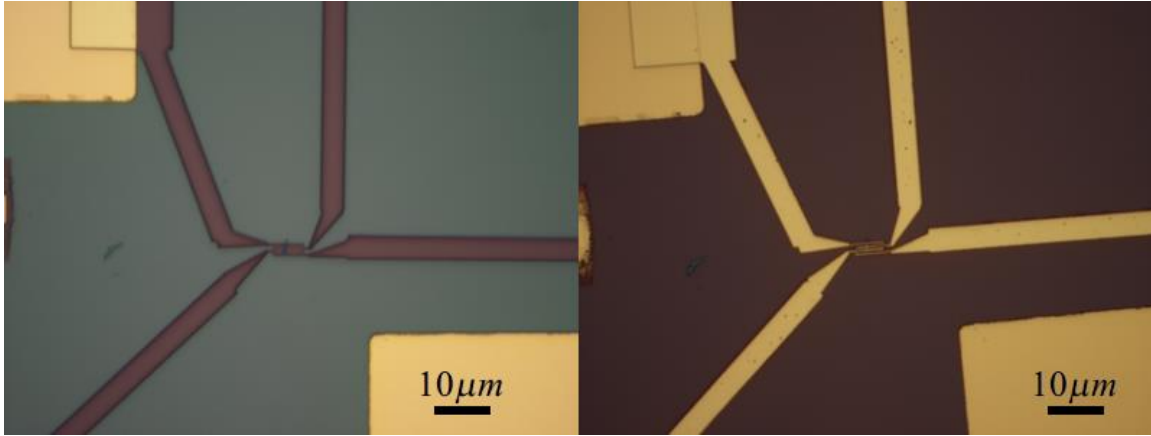


Figure 3.8: Fabrication of electrodes on flakes. Left: Developed e-beam resist mask on the flake. The center part is blurry because the distance between electrodes is below diffraction limit of the visible light. Right: Finished device with deposition of Ni(10nm)/Au(100nm) through sputtering.

The writing of alignment mark is usually done with a dosage of $300 \mu\text{C} / \text{cm}^2$ well as electrodes far from the flakes. The dosage of patterns right on the flakes need to be set separately to $430\sim 480 \mu\text{C} / \text{cm}^2$ depending on the width and separation of electrodes. The number should be carefully set because the width of each wire is only a few hundred nm and there are 4 wires running parallel to each other. Under/overdosing may cause a failed device because gold will be lifted-off in under-dosing case since there is still e-beam resist in the written pattern or the electrodes will be shorted in the case of overdosing because the width of patterns expands so the electrodes touch each other. Generally when electrodes are closer to each other, less dosage should be used and the other way else. Oxygen plasma can be used to remove under-dosing e-beam resist residue with power = 100W and time = 30s ~ 60s but the patterns will suffer some distortion so it is not

recommended for very fine electrodes. Figure 3.9 provides an example of plasma cleaning improves the as-developed pattern.

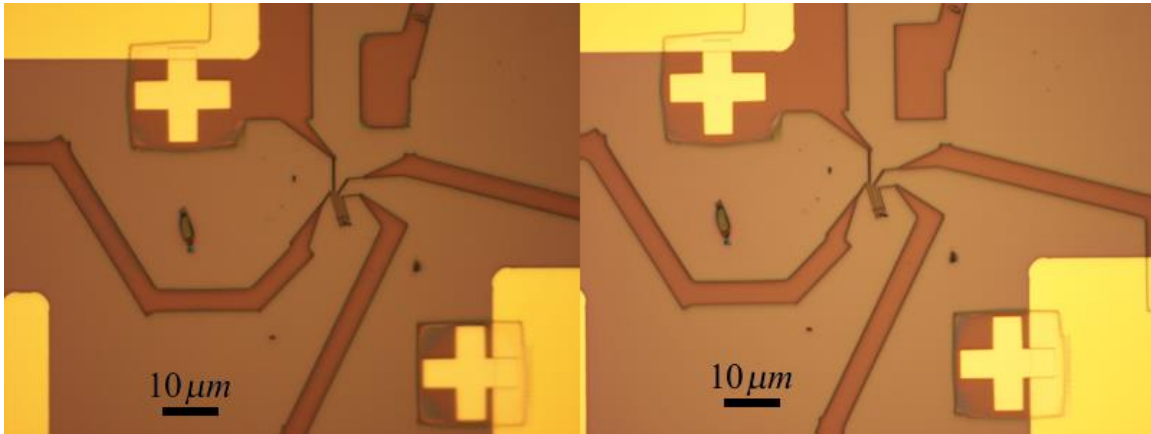


Figure 3.9: Plasma cleaning of the residue. Left: Developed e-beam resist mask with residue in the pattern. Right: Cleaned pattern after oxygen plasma power = 100W and time = 30 sec. The angles of the rectangular gate electrode become sharper and the residue in the left electrode is cleaned up.

3.4 Wiring and ESD protection

The electrostatic discharge (ESD) is a very challenging problem in the early stage of this project. Once we tried to connect a fabricated device to the probe, the flake and the electrodes always burned. The reason is because some static charges which have very high potential conduct a sudden large current through the narrow flake and generate a lot of heat and destroy the device. Depending on how much current is passed, sometimes we see the whole device are destroyed including the gold electrode deposited on the top of the flake, as shown in Figure 3.10. Sometimes only small fractions of the flake are burned which is difficult to check under the optical microscope so we have to take SEM images on them as presented in Figure 3.11. The problem is difficult to solve because static

charges exist everywhere in the environment and during the wiring process the device may make electrical contact with many other things. So the process must be taken care thoroughly from wiring up the device to transferring it into the PPMS chamber to prevent the risk of burning devices.

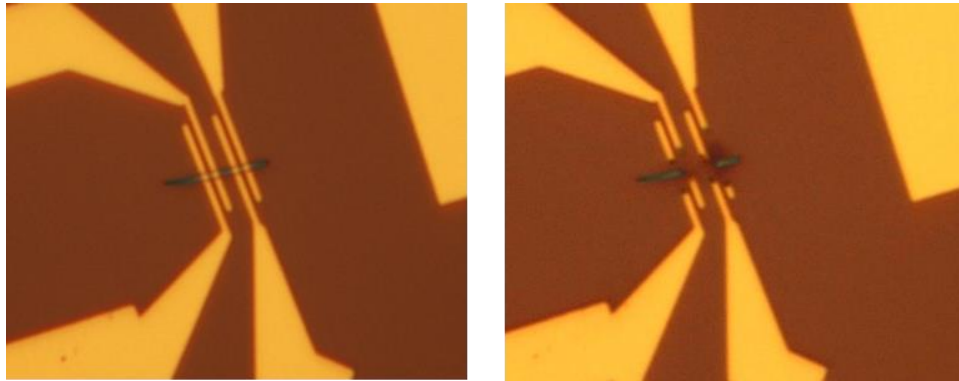


Figure 3.10: ESD hazard. The sample burned after being connected to the probe. Not just the flake but the local gold electrodes are all burned and vaporized. The device is a flake of exfoliated $\text{Ca}_3\text{Ru}_2\text{O}_7$.

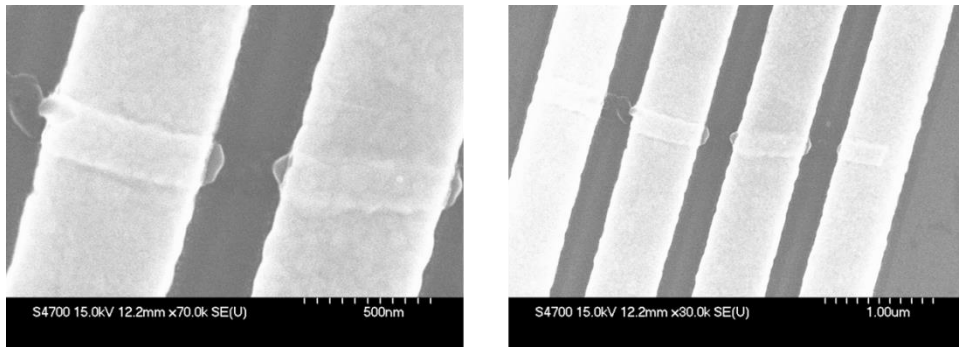


Figure 3.11: The SEM image of a burned device. The wide bright stripes are the gold electrodes and the tiny wire across the stripes is the $\text{Ca}_3\text{Ru}_2\text{O}_7$ nanoflake. The flake is burned between every two adjacent electrodes. The distance between electrodes is about 300nm.

The typical route is: A chip with fabricated devices would be placed on a clean microscope slide under a stereo microscope with a grounded aluminum case (Figure 3.12)

in order to eliminate possible charged dusts falling on the device. Anti-ESD lab coat, grounding wristband and charge dissipating gloves are equipped to prevent the discharge. Before handling the wires and touching the chips it is also recommended to turn on the ion fan (Figure 3.14(a)) and blow away charges and particles attached on cloths and skin. Mixed silver epoxy (Epoxy kit A and B 1:1) is applied on the contact pads connected with 4-probes or a gate electrode and extended away from the device by a toothpick with a thin gold wire tip. 25 μ m dia. gold wires are placed at the ends of silver epoxy extension. To cure the silver epoxy, the chip could be loaded into an oven set at 250°C for 5 minutes or directly into the PPMS sample chamber with all electrodes grounded and baked at 380K for two hours. The latter method is better because it eliminates the possibility of discharges completely since the resistance of epoxy gradually goes down and removes any potential differences between probes slowly. In addition, baking in the vacuumed chamber prevents oxidation for sensitive materials. The representative device with baked epoxy is shown in Figure 3.15. A PPMS sample puck is prepared by connecting it with a home-made socket (Figure 3.13) and grounding all contacts together including the metal part of the puck such that it can be freely moved between the stereo microscope and the ionic liquid dipping stage for convenience. The chip is mounted on the PPMS sample puck with a dip of N grease on the back side for better thermal contact and all extended gold wires are pressed onto indium contacts. The corresponding position of 4-probes and the gate electrode will be recorded on the lab book before loading. On the probe side, it is better to have the instrument (PPMS internal circuit or the Keithly 2400) turned on and running a very small current (usually 10^{-8} A) through all grounded 4-terminals before loading the device in. The reason is because when turning on the instrument there is

usually a sudden large pulse current and it may burn the device if it is connected. Two switch boxes are made to control the probes (Figure 14 (b) (c)): One can turn on/off grounding each channel and the other can add or the $1M\Omega$ buffer resistance of the current probe. The purposes of these two boxes is to ground unused probes and also keep device grounded when loading in, and also prevent a large pulse current when the current go through. The workflow of the mounting of devices is plotted in Figure 3.16.

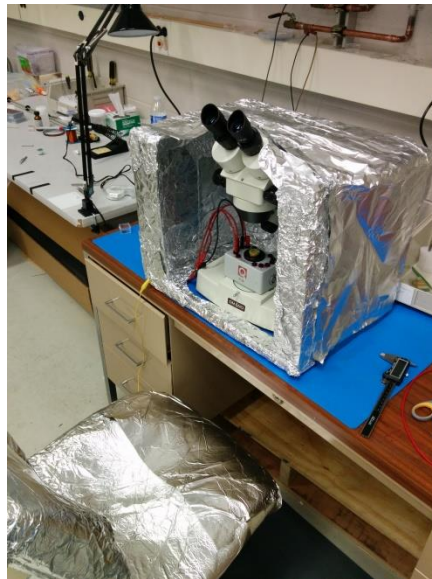


Figure 3.12: Grounding aluminum case covering the stereo microscope region. The case and the blue anti-ESD table mat are connected to the metal gasline which is connected to the ground.

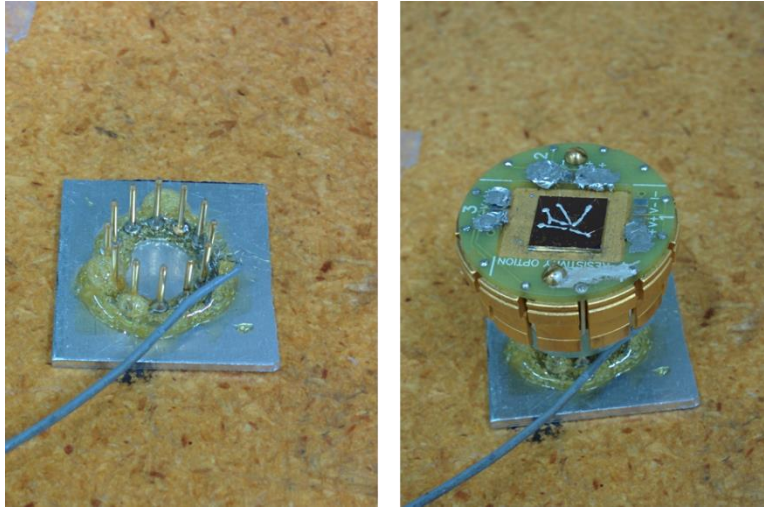


Figure 3.13: The grounding base of PPMS sample puck. The base is made with metal pins glued on a piece of aluminum. The pins are soldered together with a long wire connected to the ground.



Figure 3.14: Other anti-ESD apparatus. (a) Ion fan (b,c) grounding switch boxes for turning on/off grounding on each probe/channel. The buffer resistors used in the box are $1\text{M}\Omega$ for each channel.

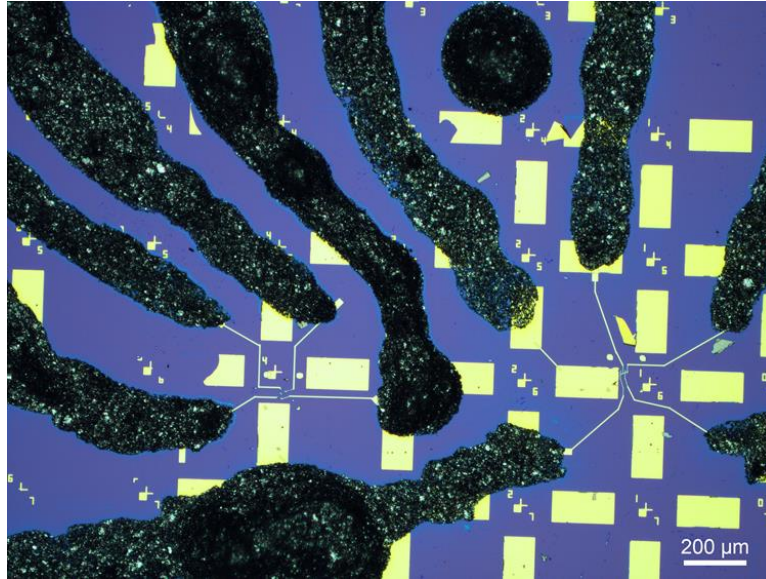


Figure 3.15: Baked silver epoxy on the chip. Black stripes are silver epoxy applied by hand with a toothpick. The epoxy stripes connects the electrodes to gold wires (not shown) and further to the push indium contacts of the PPMS sample puck. Epoxy looks dark under the microscope because the surface is rough and does not reflect light normally back into the objective.

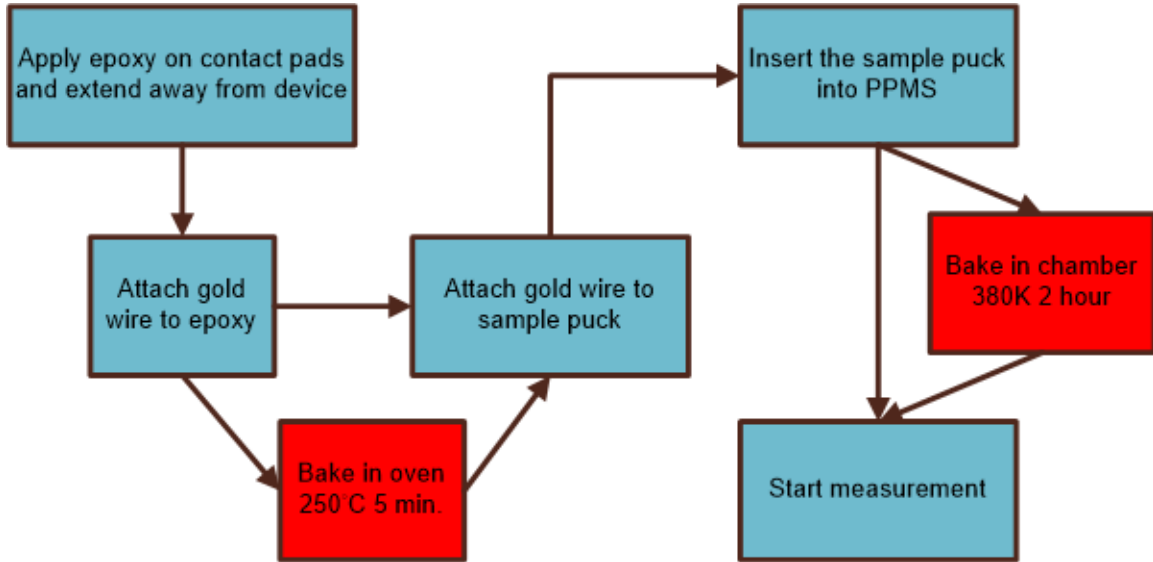


Figure 3.16: Flow diagram of wiring procedures. Baking procedures are labeled as red blocks. The epoxy need to be baked just once so there are two possible routes.

3.5 Contact resistance and 4-probe measurement

Typically there will be a large resistance generated at the junction of two different materials called “contact resistance”, especially in the case of metal and semiconductor because of the so-called Schottky barrier. It hinders the measurement of intrinsic resistance in materials because the magnitude of contact resistance could be much larger than the intrinsic resistance and we could not separate the two through direct two-probe measurement. So there are two directions to take for measuring the intrinsic resistance: lower the contact resistance and minimize its effect by 4-probe measurement.

In order to lower the contact resistance, we could not neglect the fact that the origin of the contact resistance is usually quite complicated and it differs in different systems. Here we list some of the common sources of the contact resistance: 1. Bad adhesion of the junction usually caused by rough/dirty surface. 2. Mismatch of work

function. 3. Oxidized/deteriorated surface. The methods of reducing contact resistance with individual materials will be discussed in the following.

First, the contaminant between the metal electrodes and the flake surface can be from several sources. The un-developed e-beam resist is the most common one, and the glue from the exfoliation process is the other. To remove the excess e-beam resist, the light oxygen plasma mentioned in the e-beam lithography chapter is the best way, but unfortunately only applicable to materials like $\text{Ca}_3\text{Ru}_2\text{O}_7$ which is invulnerable to oxidation. In other cases the tuning of e-beam lithography parameters such as dosage and development time to reduce the possibility of un-developed resist is a crucial issue. The same problem happens with glue residue since some residue cannot be removed by acetone or IPA. Even though there are some studies³⁹ about using diluted room-temperature RCA clean solution mentioned before (original $\text{H}_2\text{O}_2:\text{NH}_4\text{OH}:\text{H}_2\text{O}$ 1:1:5, diluted 1:1:10 or 1:1:20) and soaking graphene for overnight to remove the photoresist residue, that is not 100% effective to glue and still have potential oxidation concern (graphene is relatively chemical-inert so it is free of this problem).

The work function mismatch between the flake and the adhesion layer of metal electrodes has been briefly mentioned in the lithography section. Especially in metal-semiconductor junction, the large difference of work function makes the junction a Schottky barrier. Ti (work function = 4.33eV) thin film leads to large contact resistance up to $\sim\text{M}\Omega$ for typical contacts on $\text{Ca}_3\text{Ru}_2\text{O}_7$ and has been replaced by Ni (5.04eV) which is closed to gold (5.1eV) and the contact resistance is minimized.

At last we discuss the degraded surface of flakes which mainly occur in Fe_{1+y}Te or Te-rich $\text{Fe}(\text{Se},\text{Te})$. At the early stage of the FeTe project, the tricks of lowering contact

resistance we developed for $\text{Ca}_3\text{Ru}_2\text{O}_7$ does not work for FeTe at all. We tried optimizing the lithography process to get very clean development, and make many devices with different metals for electrode deposition but it always shows insulating behavior at low temperature. The I-V curves of every two electrodes are very non-linear as shown in the Figure 3.17.

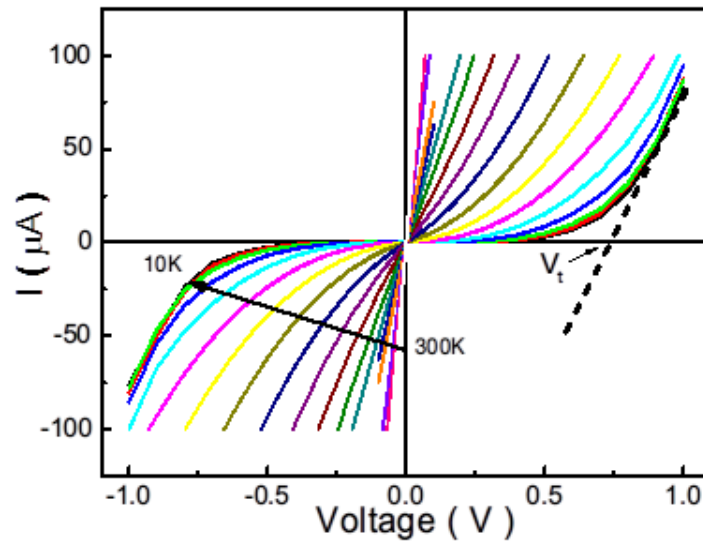


Figure 3.17: The I-V curve of a large FeTe flake from 300K to 10K. The low-temperature I-V has a turn-on voltage V_t taken from the crossing of extension of high-voltage part and the zero current voltage axis.

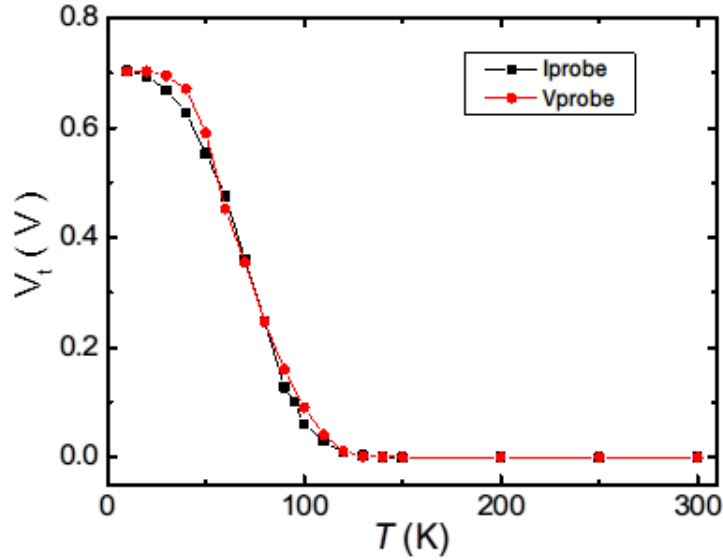


Figure 3.18: The evolution of V_t as a function of temperature for two pairs of electrodes. The rapid raising of V_t starts from around 100K and becomes saturated at low temperature.

We first suspect the behavior originates from the Schottky barrier, but the discrepancy between the thermionic emission model and the observed turn-on voltage cannot be explained since the V_t saturated at low temperature (Figure 3.18). From the graph it can be understood as an insulating barrier with finite length formed around 100K, so the voltage needed to tunnel the barrier will not diverge since the length is fixed. By fitting the I-V curve we found the length at 10K is about 1.2 nm, which coincide with the observation with TEM of the surface layer degradation of $\text{Fe}_{1+y}\text{Te}^{40}$. To solve this problem, we use *in-situ* ion-milling before the metal deposition to remove 2 nm of surface layer of flakes, and the I-V curve of newly fabricated devices becomes linear at all temperature range with a contact resistance on the order of 100Ω at room temperature estimated by the difference of 4-probe and 2-probe measurement in the example in Figure

3.19. Other flakes like the 15nm one which is insulating shows the similar result (in Chapter 5).

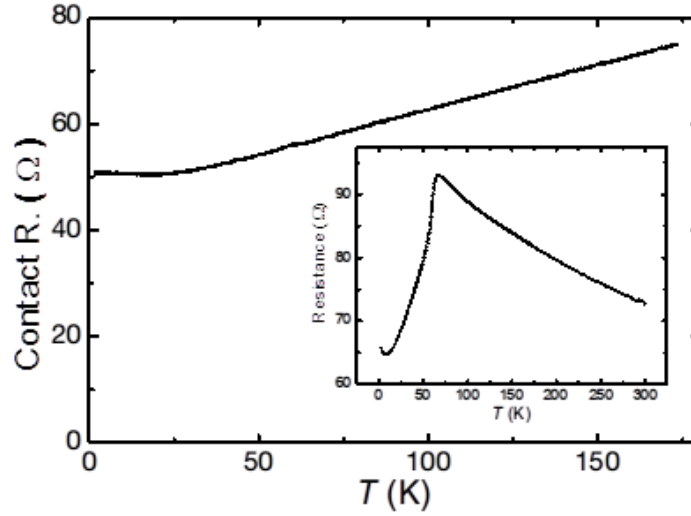


Figure 3.19: Contact resistance of a 54 nm Fe_{1+y}Te flake device fabricated with in-situ ion-milling procedure. Inset: The 4-probe measurement retains the bulk-like behavior. The R-T curve shows nice metallic behavior confirming the ohmic contact properties in all temperature range.

Finally we introduce briefly the four-probe measurement. The idea of four-probe measurement is shown in the Figure 3.20. To measure the intrinsic resistance of the sample, e.g. R_{S2} , we cannot avoid a contact resistance R_C when we use a metal electrode deposited on the surface of the sample. The solution is applying a larger current I_S through the sample with two outer electrodes and measuring the voltage difference of two inner electrodes with a smaller current I_P . Since the voltage drop will be

$$V = I_P (R_{C2} + R_{C3}) + (I_P + I_S) R_{S2}$$

$$\frac{I_P}{I_S} \ll \frac{R_S}{R_C}, V \approx I_S R_{S2}.$$

(R_C , R_S here is the order of magnitude of contact and intrinsic resistance.)

Usually the probe current is about the order of pA (e. g. Keithley 2400 we used), given that our I_S is on the order of μA , the 6 orders of difference will be able to eliminate the effect of contact resistances.

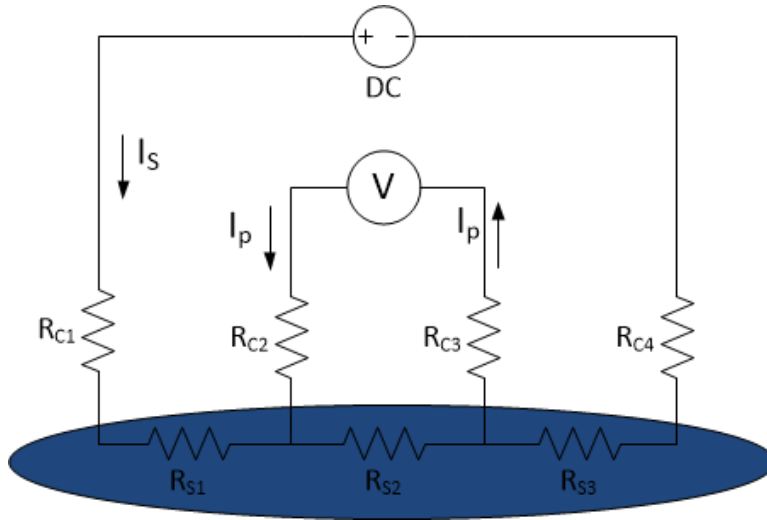


Figure 3.20: Resistor model of 4-probe measurement. $R_{C\#}$ stands for the contact resistance of $\#$ th contact and $R_{S\#}$ for the intrinsic resistance of the flake. Blue ellipsoid denotes the flake.

3.6 Ionic liquid gating

Ionic liquid is defined as a kind of organic salt with melting point below room temperature. Because of the ions flowing freely inside the liquid it usually has pretty high dielectric constant compared to common gating oxide material such as SiO_2 or Al_2O_3 .⁴¹ The liquid forms electric double layer on the interface when a potential difference is applied on both sides and generates very large carrier density on the electrodes in contact with the liquid. The liquid we used in our experiment is DEME-TFSI (N,N-diethyl-N-(2-methoxyethyl)-N-methylammonium bis(trifluoromethylsulphonyl-imide)), which is commonly used in many EDL (electric double layer) devices. It breaks into DEME^+ and

TFSI when the voltage is applied on two electrodes in contact of the liquid, and it freezes below 180K and the induced charge on surface will be frozen as well. The chemical composition is shown below in Figure 3.21.

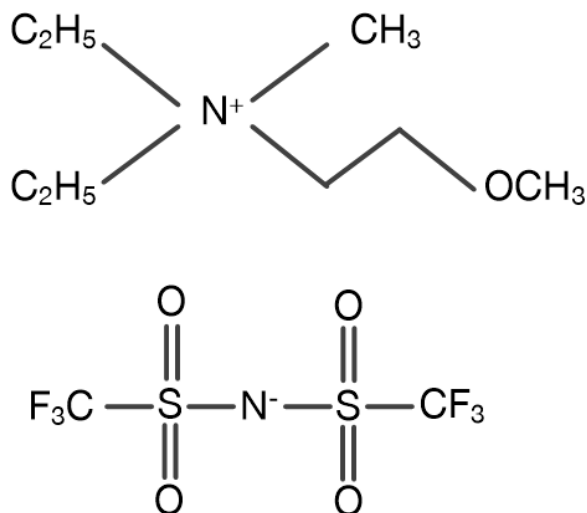


Figure 3.21: The chemical composition of DEME⁺ (top) and TFSI⁻.

The working cycle depends on the type of the ionic liquid. Take DEME-TFSI as an example, the liquid freezes at 180K so the electric field has to be applied above the temperature so the molecules could still move around to form electric double layer on the gated surface. And usually gate voltage is scanned within positive to negative 6V at this temperature to see the resistance voltage change as a first observation of gate effect. Then the gate voltage will be fixed and the device will be cooled down to low temperature to see if low-temperature properties can be change by this gating voltage.

To apply a reasonable amount of ionic liquid on the device, I built up a setup for precise dipping purpose by using existing material in the lab. First I attached a flash light on one of the eye pieces of a biological microscope which has only bottom light source so that it can serve as a one-eyed confocal microscope. To record the images I used cell-

phone camera and took the image through the eyepiece. Second, I sharpened a toothpick and taped it on a wedge of microscope slides combined with an optical micro-stage which can move in three dimensions with micrometer precision. The tip of the toothpick could pick up very little ionic liquid and move under the microscope so that the liquid can be dropped at desired location by lowering the tip carefully toward the surface. When the tip gets very closed I would pull it up and see if there is some liquid left on the surface, this usually takes a couple times of practice to get a desired size of droplet and precise location.

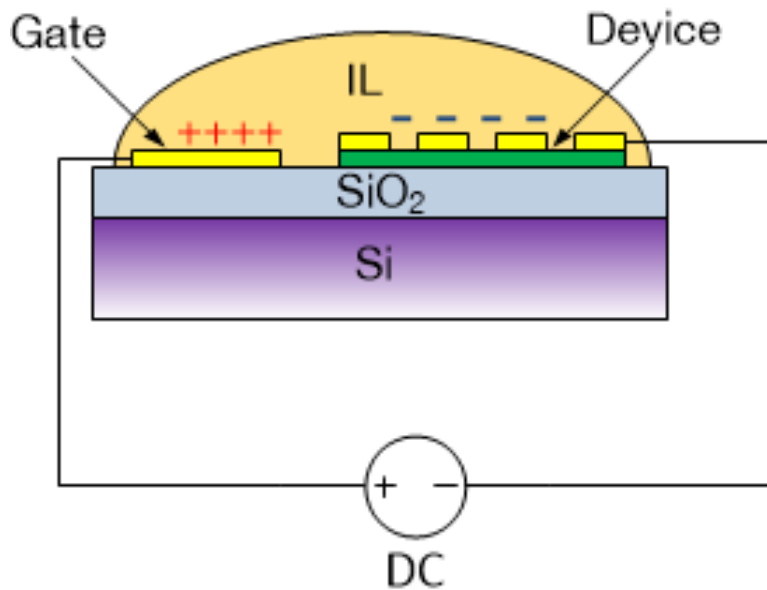


Figure 3.22: The idea of ionic liquid gating (cross-section of a IL-gating device). The yellow pad is the gold pad deposited on the substrate as the electrode for the device and the large gate pad near the sample. When the voltage is turned on, there will be high charge density induced on the surface of the gate electrode and the device.

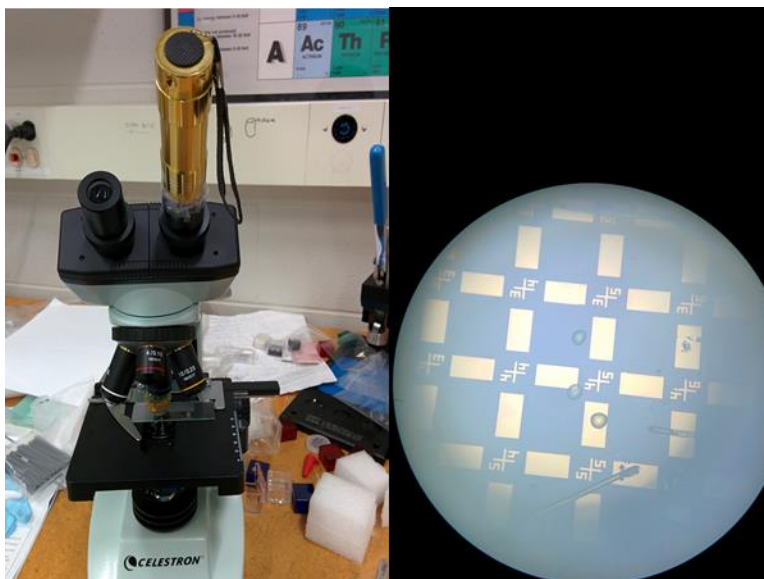


Figure 3.23: Microscope setup. Left: The microscope with flashlight attached to it. Right: A image seen from the other eyepiece, taken by cell phone camera. The little droplets are dips of ionic liquid dropped on surface for practice.



Figure 3.24: The toothpick attached on the optical microstage used in dipping ionic liquid on the chip.

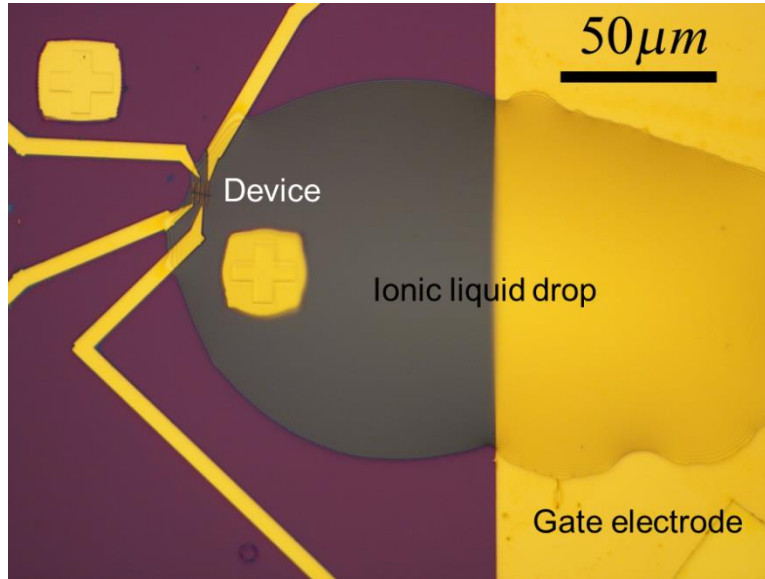


Figure 3.25: An ionic liquid drop on Ca_2RuO_4 device. This is a nice example because we want the area ratio covered by ionic liquid of device to gate electrode to be very small, and the drop position and size is just desired.

SiO_x rings are put onto the device as the optional step for ionic liquid application. The purpose of this ring is to block the contact between large gold pad nearby that shares most of the voltage drop. A ring pattern with inner diameter $\sim 100 \mu\text{m}$ and outer diameter $\sim 200 \mu\text{m}$ is written on a device rounding the flake and an ionic liquid gate inside. When the devices are made they are visible in the SEM so the last step does not require an alignment. The SiO_x is deposited by thermal evaporation in another chamber. The finished device with ionic liquid added is in Figure 3.26. Later we found it is not efficient to put such a ring compares to designing the electrodes not using large gold pads nearby except the gate electrode. Thus it was not used in devices fabricated later on. To avoid the contact pad, we just pull the electrode far away in the lithography process.

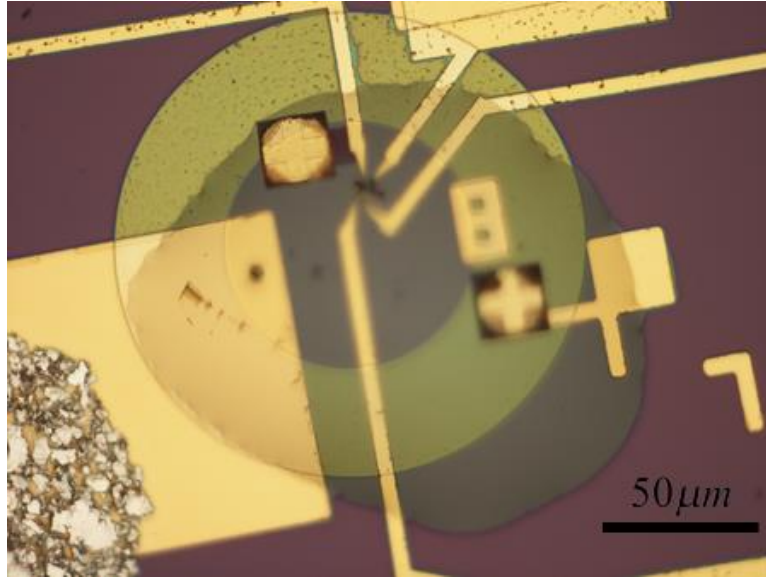


Figure 3.26: SiO_x ring surrounded device with ionic liquid dropped. The SiO_x ring is transparent, covering the nearby wires and circuit. The ionic liquid drop changes the optical length so the center of device and the flake are blurred, not focused simultaneously with other parts of the image.

The key problem in the ionic liquid gating is the leakage current. Ideally ionic liquid should be insulating and work as a dielectric media, but just like other dielectric, the current will leak through with high electric field. The problem is more serious at high temperature. At room temperature, only 3 volts of gating voltage can create a significant leakage current as seen in the Figure 3.27. The current induces a voltage drop between the electrodes of the device which interferes with the 4-probe measurement of the intrinsic resistance. The Figure 3.28 shows a measurement on the same sample using different excitation current with the leakage current induced voltage drop, confirming the drop is not an intrinsic effect of the flake resistance since it shrinks with larger excitation current.

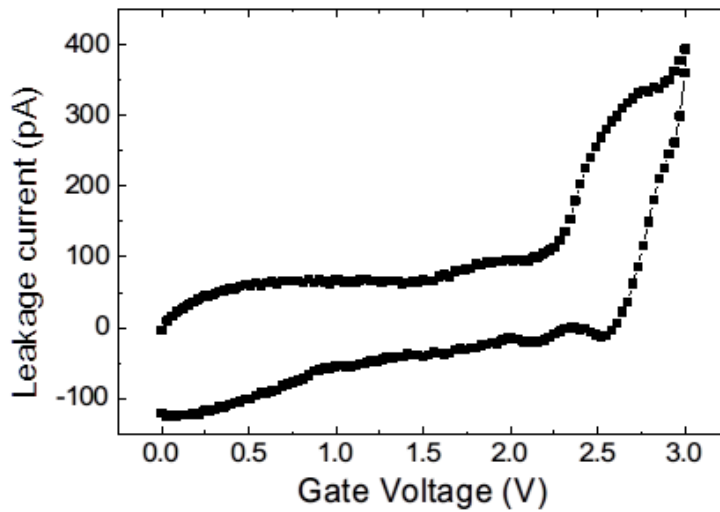


Figure 3.27: Leakage current as a function of gate voltage at room temperature.

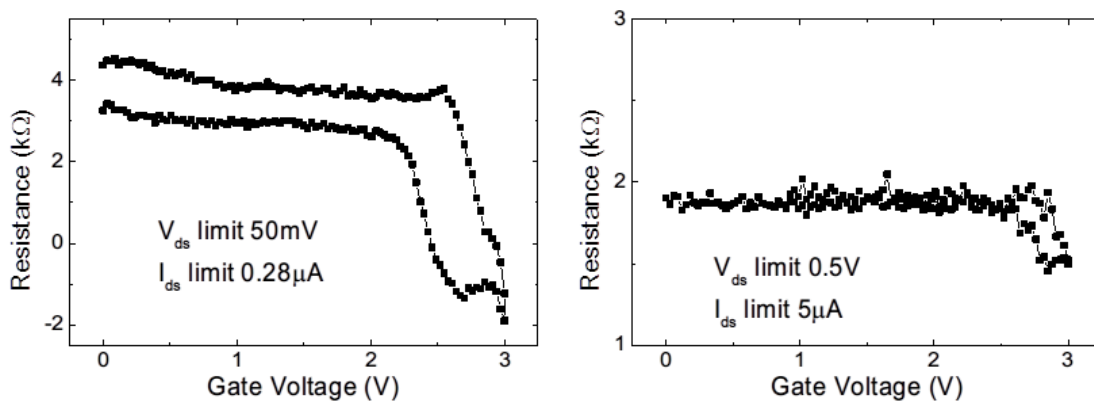


Figure 3.28: Gate voltage influence on 4-probe resistance measurement.

The limitation on both voltage and current through the drain-source electrodes is applied. The device is a 40nm Ca_2RuO_4 thin flake.

If a large voltage is applied on the ionic liquid, eventually the liquid will break down. In Figure 3.29 we saw two examples of the breakdown with positive and negative voltage. As mentioned above with only 3 Volts there is already significant leakage current. If 6 Volts is applied at room temperature the liquid will break down for sure and

cause a large voltage drop as observed in the resistance drop in the Figure. The difference in resistance drop from the two graphs is again from the difference of excitation current. After the breakdown, the device is usually destroyed by the electro-etching effect and both flakes and electrodes are etched away (Figure 3.30).

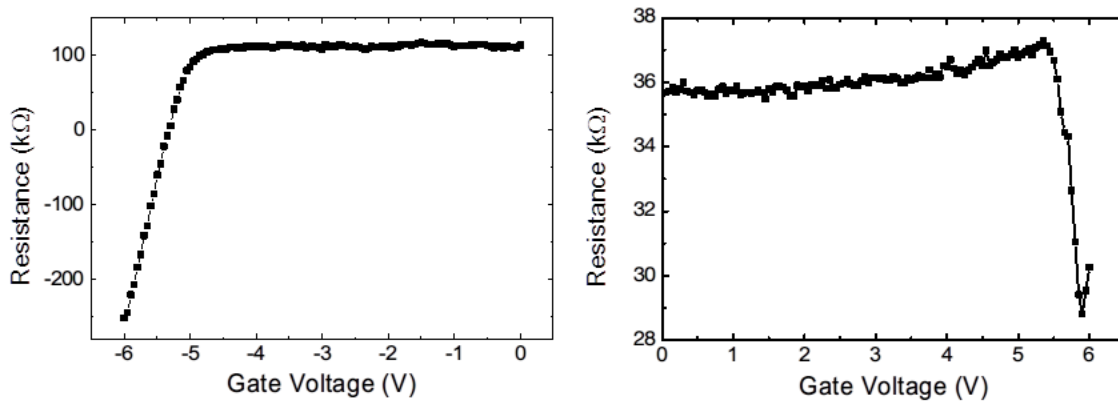


Figure 3.29: Breakdown of the ionic liquid at room temperature. Both of the devices are Ca_2RuO_4 thin flakes.



Figure 3.30: Etched surface by ionic liquid after the measurement. The liquid dispersed all over the surface.

Based on the experience, we prepared a batch of test devices using exfoliated graphene to examine the gate effect. Graphene as a well-known material is good for the test, since the exfoliation and device fabrication is relatively easier than all of materials studied in our projects, and also the thickness is below 1nm which makes carrier doping very effective. We successfully retained the typical gate effect of graphene by scanning the voltage at 200K right above the freezing point of the liquid. The results are shown in Figure 3.31 and Figure 3.32. The R-V curves exhibit a peak in resistance because graphene has a Dirac-cone band structure and allows electron or hole-doping depending on gate voltage. The resistance peak is the charge neutral point (CNP) where ideally there is no free electron or hole so the resistance reaches the maximum. The peak position is shifted after each scan probably because of the gating voltage moved the local charged impurities and changed the CNP. We have also tried several scan speed and as expected, slower scan speed leads to smaller peak shift and the peak shape is also sharper. After several rounds we froze the liquid by cooling down to 160K and warmed up to 200K again, tested with scan speed = 8.8mV/s again and see similar results. We have confirmed the similar result on other graphene devices as well.

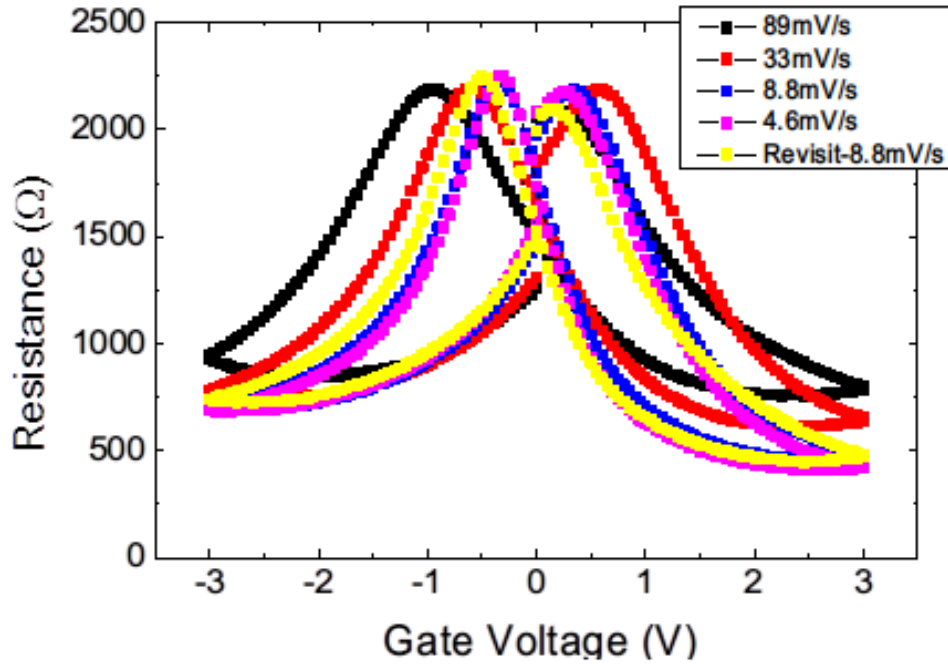


Figure 3.31: Graphene resistance as a function of gate voltage. The curve is scanned at various scanning speeds scanned at 200K. Scanning route is always 0V, 3V, -3V, 0V. The resistance at high gate voltage reaches about 25% of the peak value.

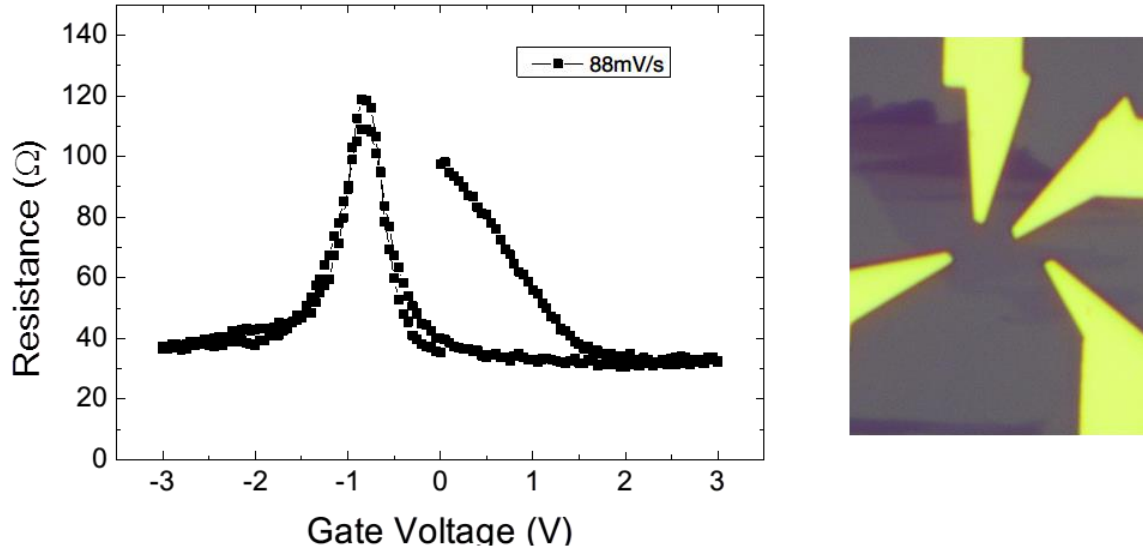


Figure 3.32: The image of graphene device and the R-V curve. The device shows sharper charge neutral point peak but it is finally destroyed at low temperature because the frozen ionic liquid broke.

After the gate voltage scanning, we tried to cool the device down to lower temperature. But the frozen ionic liquid always broke and destroyed the device. Slow cooling rate ($<1\text{K}/\text{min}$) is used but the frozen liquid still breaks. Somehow on $\text{FeSe}_{0.5}\text{Te}_{0.5}$ and some Ca_2RuO_4 flakes we don't have this problem. Currently we still cannot control this problem at low temperature and it may be the most frustrating problem in using ionic liquid. I have a suspect that is correlated to the substrate surface properties such as hydrophilic or hydrophobic since I have treated the graphene surface with diluted RCA clean solution and it will make the surface hydrophilic, or the moisture absorbed on the surface but has not tried it out. Ionic liquid is super sensitive to the water moisture and that could be the reason. For the future plan it may be necessary to examine this

problem before re-starting projects related to ionic liquid. More information about the future plan can be found in Chapter 6.

Chapter 4

Calcium ruthenate thin flake study

From the method established in previous chapters, we exfoliated calcium ruthenate flakes for the first time and fabricated 4-probe devices with various thickness using mechanical exfoliation method. In this chapter we mainly focus on the study of nanostructured $\text{Ca}_3\text{Ru}_2\text{O}_7$. Through the (magneto)transport measurement on exfoliated $\text{Ca}_3\text{Ru}_2\text{O}_7$ nanoflakes, we find that thin flakes below 10 nm become more insulating and the magnetoresistance behavior is drastically different from that of thicker samples, implying a change in both electronic state and magnetic order. Such a change may be associated with the enhanced RuO_6 octahedral distortion and weakening of ferromagnetic interaction due to the loss of oxygen at the cleaved surfaces, whose contribution to the physical properties becomes more significant as the surface-to-volume ratio increases in the thinner flakes. In section 4.5, we briefly discuss our preliminary study on Ca_2RuO_4 nanoflakes and the potential electric gating effect using ionic liquid. These studies not only bring another dimensionality to control the physical properties of ruthenates, but also in general establish the marriage between correlated electron systems and two dimensional materials.

4.1 Bulk material properties of $\text{Ca}_3\text{Ru}_2\text{O}_7$

The strong electron-electron Coulomb interaction and the intimate interplay between spin, charge, lattice, and orbital degrees of freedom in transition-metal oxides (TMOs) give rise to a rich variety of interesting electronic and magnetic phenomena^{42 43}. In general, the strong magnetic and electronic instabilities in these systems render their properties very susceptible to subtle non-thermal stimuli, such as chemical doping,

magnetic field, pressure, etc., which can readily tip the balance between competing interactions and generate new quantum phases and complex phase diagrams.

Recently, there have been increasing efforts in studying nanostructured correlated TMOs which enable ones to probe the exciting collective phenomena arising from quantum confinement, to tune materials properties via electrostatic gating effect, as well as to probe the non-equilibrium physics of correlated TMOs stemming from the competition of various interactions⁴⁴. Thus far, most of studies on nanostructured TMOs have been focused on oxide nanowires or epitaxial oxide thin films. However, for TMOs with layer structure, earlier attempts on thin film growth often led to intergrowth of the materials which change the materials properties in unintentional ways⁴⁵. In contrast, the mechanical exfoliation approach not only can circumvent the intergrowth problem, but also offers the feasibility to deposit the exfoliated oxide nanosheets on a variety of templates for potential device applications. Although research along this line is still in its infancy, early attempts have shown some success. For instance, recent Raman spectroscopy on the nanosheet structure of high- T_c superconductor, $\text{Bi}_2\text{Sr}_2\text{CaDy}_x\text{Ca}_{1-x}\text{Cu}_2\text{O}_{8+\delta}$, reveals a significant change in the strength of magnetic exchange interaction compared with the bulk material⁴⁶; and transport measurements on a monolayer of superconducting $\text{Bi}_2\text{Sr}_2\text{CaCu}_2\text{O}_x$ show an insulating behavior²². Thus, the cleaved oxide nanosheets provide a unique platform to investigate physical properties of the correlated oxides at nanoscale.

Ruthenates with Ruddlesden-Popper (RP) layer structure, $(\text{Sr,Ca})_{n+1}\text{Ru}_n\text{O}_{3n+1}$, represent an exciting class of $4d$ TMOs, which display a broad spectrum of perplexing ground state properties^{47 48 49}. With reduced n (e.g., $n = 1$, or 2), although the associated

RP materials can generally be regarded as quasi-two dimensional systems, the correlation between layers along the c-axis still plays a non-negligible role in determining physical properties of bulk materials. For example, the observation of c-axis coherent transport in bulk $\text{Ca}_3\text{Ru}_2\text{O}_7$, Sr_2RuO_4 and $\text{Sr}_3\text{Ru}_2\text{O}_7$ at low temperatures implies that the charge carriers are not fully confined to the layer planes^{50 51 52}. Besides, the interbilayer coupling in $\text{Ca}_3\text{Ru}_2\text{O}_7$, albeit weak, is crucial in leading to the antiferromagnetic transition resulting from the coupling between bilayers^{53 54 55 56}. Thus, provided the nanosheet structures of RP ruthenates with the reduced dimensionality along the c-axis, one may anticipate the physical properties of ruthenates to change dramatically. In addition, due to the symmetry breaking and the absence of constraint at the surface and interface, the structural distortion of RuO_6 octahedron may be markedly altered considering the enhanced surface-to-volume ratio in the nanosheet structure, which is also expected to strongly modify magnetic and electronic properties in nanosheets as a result of the strong correlation between lattice and other degrees of freedom in RP ruthenates.

The material of interest in this work is the bilayer ruthenate ($n = 2$), $\text{Ca}_3\text{Ru}_2\text{O}_7$.(Figure 4.1) $\text{Ca}_3\text{Ru}_2\text{O}_7$ exhibits two phase transitions: one at $T_N = 56$ K corresponding to the paramagnetic-antiferromagnetic phase transition, and the other at $T_{\text{MIT}} = 48$ K referring to a metal-insulator-like phase transition that is accompanied by the change of the magnetic moment direction from the a-axis at high temperature to the b-axis at low temperature^{53 57 55} (Figure 4.2). Such magnetic anisotropy is known to arise from spin-orbit coupling via lattice, which is intimately related to the structural anisotropy with different degree of RuO_6 octahedral tilting along the a-axis and b-axis (as seen in Figure 4.1)⁵⁸. And it was proposed that the change of spin anisotropy below T_{MIT}

is essential to the change of the electronic band structure⁵⁹. The metallicity of $\text{Ca}_3\text{Ru}_2\text{O}_7$ reappears below 30 K⁵⁰, originating from a small Fermi surface pocket surviving through the MIT⁶⁰. And this material possesses strong magnetic and electronic instabilities, as evidenced by their susceptibility to chemical substitution, pressure, and magnetic field reported previously^{61 56 62 55 63 64}.

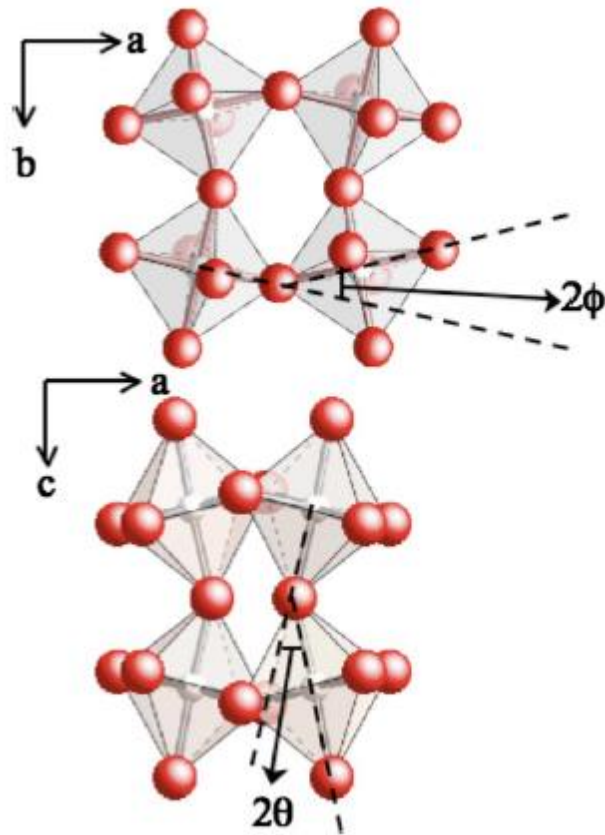


Figure 4.1: Schematics of RuO_6 octahedral distortion in $\text{Ca}_3\text{Ru}_2\text{O}_7$. ϕ and θ are defined as rotation and tilting angles.(From J. Peng Phys. Rev. B (2010))

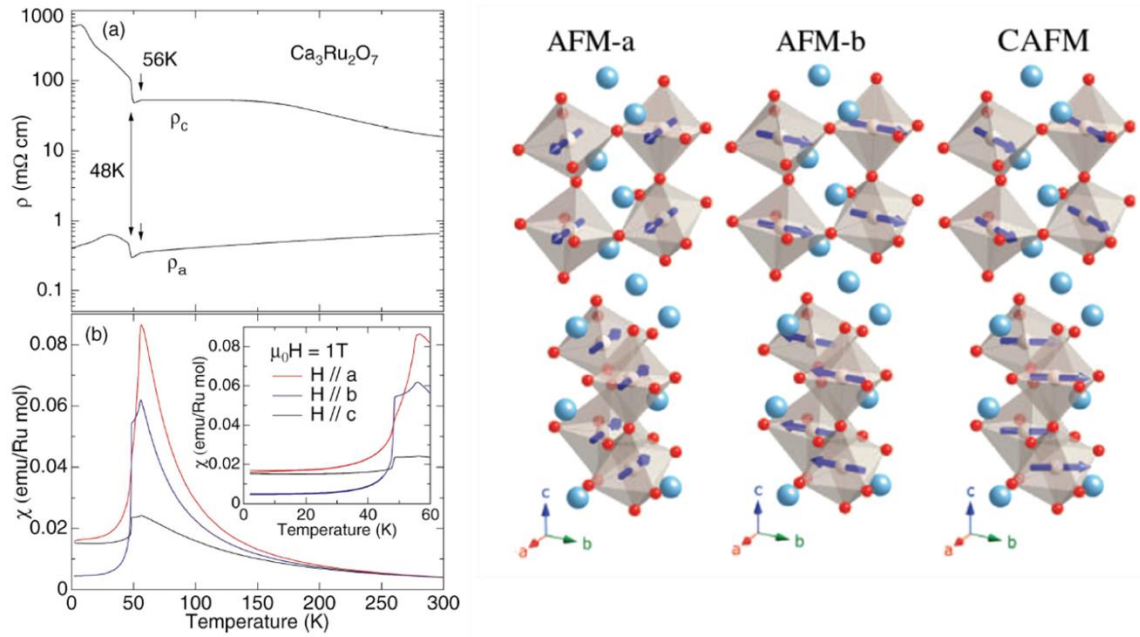


Figure 4.2: The metal-insulator transition and AFM transition of bulk $\text{Ca}_3\text{Ru}_2\text{O}_7$. Left: the resistivity along a and c axis and the magnetic susceptibility gives the $T_{MIT} = 48\text{K}$ and $T_N = 56\text{K}$. Right: The magnetic structure of $\text{Ca}_3\text{Ru}_2\text{O}_7$ (from Yoshida, Y. et al.,(2004) Phys. Rev. B and Wei Bao et al., Phys. Rev. Lett. (2008)).

4.2 MIT in thin flakes

$\text{Ca}_3\text{Ru}_2\text{O}_7$ single crystals were grown using floating zone method. By gluing both sides (ab plane) of the crystal on two pieces of microslides and plying open the crystal, flakes are generated on the newly broken surface which are then transferred to the pre-patterned SiO_2 (285 nm)/Si substrates using Scotch tape method. Oxygen plasma cleaning is performed to remove excess glue from the tape. Flakes with various thickness ranging from ~ 3 nm up to ~ 100 nm were located under an optical microscope and then the topology was measured using the atomic force microscope. Nanoflake devices with

four-terminal electrode pattern were fabricated using the standard e-beam lithography procedure (inset of Figure 4.3). Ohmic contacts were formed by depositing 10 nm Ni (used as the adhesive layer) and 100 nm Au electrodes by DC sputtering. Electronic transport measurements were carried out using Quantum Design PPMS cryostat. Note that an earlier study of exfoliated $\text{Ca}_3\text{Ru}_2\text{O}_7$ can only achieve flakes as thin as 300 nm³⁸. Details of the procedures are described in Chapter 2 and 3.

Figure 4.3 presents the atomic force microscopy images of several representative flakes of different thickness. All the flakes show atomically flat surface, as illustrated by the line profile scan done on a 9 nm flake sample shown in the inset. It is worth noting that the thinnest flake with sizeable lateral dimension that we achieved is ~ 3 nm depicted, which corresponds to 1.5 unit cell thick (note the lattice parameter $c = 1.956$ nm).

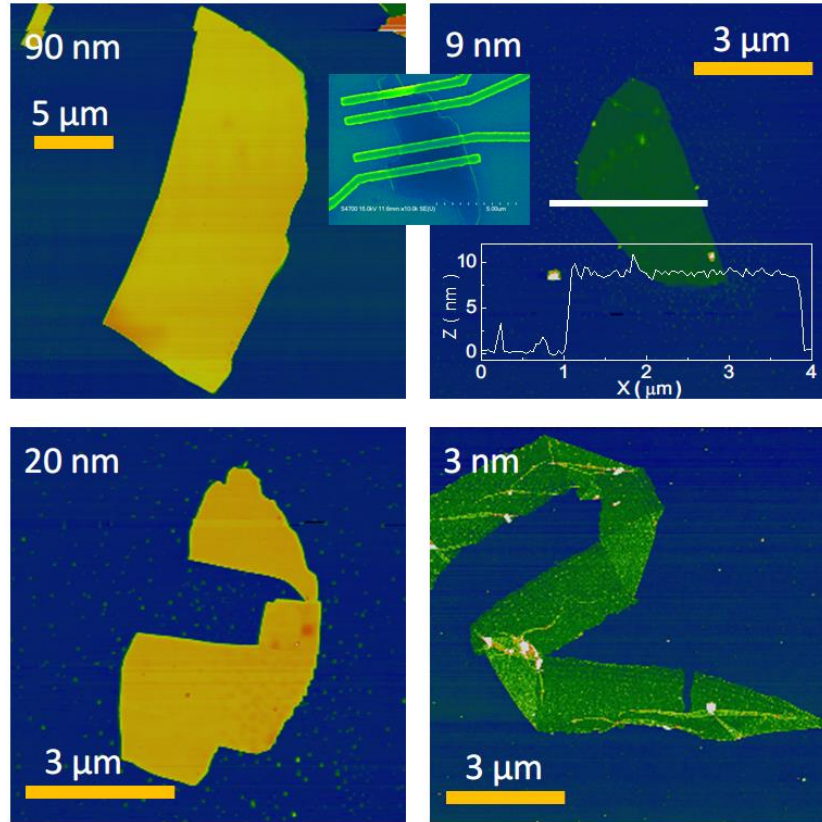


Figure 4.3: AFM images of exfoliated $\text{Ca}_3\text{Ru}_2\text{O}_7$ flakes. Representative atomic force microscopy images of the exfoliated $\text{Ca}_3\text{Ru}_2\text{O}_7$ flakes with different thickness. Insets show the scanning electron microscope image with false color of a fabricated flake device with 4 gold electrodes and the cross section line profile of the 9 nm flake

Figure 4.4 shows the resistivity (ρ) as a function of temperature (T) measured on devices with various flake thickness. For the 90 nm flake, the $\rho(T)$ curve behaves identical to what is observed in the bulk counterpart⁵⁰: a large drop in resistivity occurs at $T_N = 56$ K followed by a sudden (first-order type) increase at $T_{\text{MIT}} = 48$ K, and eventually the metallic resistivity behavior reappears below 26 K. With decreasing the flake thickness (25 nm and 13 nm), while the overall MIT and the reentrance of metallicity behaviors are preserved, the first-order type MIT is smeared out. As the flake thickness

further decreases, T_{MIT} observed in the device of 9 nm and 8 nm flakes clearly shifts to 33 K and 30 K respectively without the re-entrance of metallicity at lower temperature. Interestingly, for the thinnest measurable flake (~ 7 nm), no transition is observed and the device shows an insulating behavior all the way to the lowest temperature, with the resistivity two orders of magnitude higher than that for thicker flakes at $T = 2$ K. And flakes thinner than 7 nm are very resistive and not measurable.

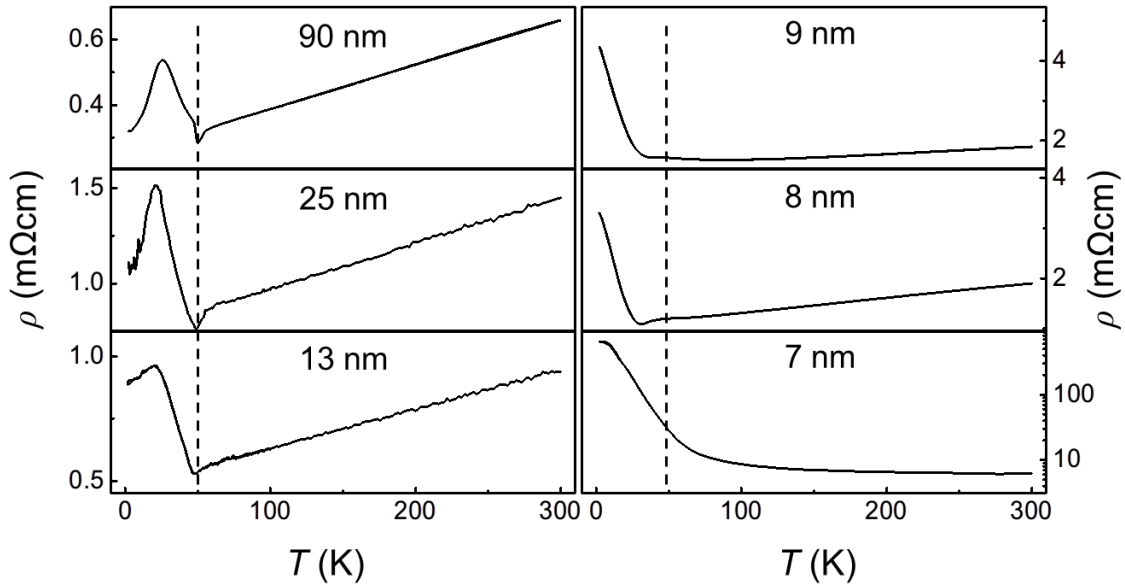


Figure 4.4: R-T curves of $\text{Ca}_3\text{Ru}_2\text{O}_7$ exfoliated flakes. Thickness is labeled in each graph and the dashed line indicates the T_{MIT} in bulk. Three thicker flakes on the left follows the T_{MIT} but the other three thinner flakes on the right the T_{MIT} deviate significantly.

There are a couple of scenarios that may happen to the structure as the flake becomes thinner and thinner. On the one hand, it is known that compared to Sr-based counterparts, Ca-based ruthenates tend to have much larger structural distortion due to the smaller ionic radius of Ca^{2+} than Sr^{2+} ⁶⁵. Thus, naively, one may anticipate that the

RuO₆ octahedral distortion might be (partially) relaxed due to the absence of constraint on the surface and interface. Provided this was the case, however, the flakes should become more metallic as the thickness decreases, which is opposite to the experimental observation. On the other hand, earlier scanning probe microscopy and low-energy electron diffraction studies on Sr₂RuO₄, which has no structural distortion in bulk, found that the RuO₆ octahedra on the cleaved surface layers are distorted with an octahedral rotation around the c-axis by about 9 degree⁶⁶. Similarly, larger RuO₆ octahedral distortion was also observed on cleaved surface of Ca_{1.9}Sr_{0.1}RuO₄, which gives rise to lower T_{MIT} on the surface compared to the bulk⁶⁷. Therefore, as the exfoliated nanoflake gets thinner, its RuO₆ octahedral distortion might become more severe. A natural question then arises: What drives the larger structural distortion on the surface of ruthenates? One plausible mechanism is the loss of oxygen on the cleaved surfaces. It is highly likely that the apical oxygen atoms in the RuO₆ octahedra are (partially) lost on the cleaved surface, which leads to oxygen deficient on the surface layer. Recently, it has been found that oxygen deficiency in Sr₃Ru₂O_{7-δ} and Ca₂RuO_{4-δ} give rises to a decrease in the c-lattice parameter but an increase in the in-plane lattice parameters, thus resulting in larger RuO₆ distortion compared to the stoichiometric compounds^{68 69}.

Accordingly, the enhanced structural distortion may account for the decrease of T_{MIT} in the thinner Ca₃Ru₂O₇ nanoflakes shown in Figure 4.4, a feature similar to the reduced T_{MIT} on the cleaved surface of Ca_{1.9}Sr_{0.1}RuO₄ compared to the bulk counterpart⁶⁷. Furthermore, the enhanced structural distortion in thin nanoflakes is anticipated to reduce the electronic bandwidth as well, leading to the tendency of opening the bandgap. Thus, as the nanoflake gets thinner and thinner such that the surface-to-volume ratio become

larger, the electronic state arising from the cleaved surface and interface layers becomes dominant, resulting in the observed more insulating transport behavior for flakes thinner than 8 nm. Additionally, the reduced bandwidth, i.e., the decrease of the carrier hopping energy (t) tends to soften the antiferromagnetic phase transition ($T_N \sim t^2/U$, U : Coulomb energy). For instance, T_N is ~ 42 K in the 8 nm flake compared to 56 K in the bulk sample. It is worth noting that the partial reduction of Ru^{4+} to Ru^{3+} due to the loss of oxygen atom can weaken magnetic exchange interactions and contribute to the decrease of T_N too.

4.3 Magnetoresistance and antiferromagnetic transition

In addition to the insulating behavior at low temperature, thinner flakes also exhibit markedly different magnetic anisotropy and magnetoresistance (MR, which is defined as $\frac{\rho(H)-\rho(0)}{\rho(0)}$) behavior from those of thicker films or bulk. Figure 4.5 shows the comparison of the in-plane angle dependence of MR for two flakes of 90 nm and 8 nm at various temperatures. The measurement field is 9 T, and the angle (θ) is relative to the chip edge. For the 90 nm flakes, the $\text{MR}(\theta)$ exhibits two-fold symmetry with troughs positioning around 220° and 40° at $T = 60$ K but with troughs around 130° and 310° at $T = 2$ K, and the $\text{MR}(\theta)$ curves at these two temperatures can be roughly fitted using a sine-squared function. Such an angular dependent MR behavior mainly stems from spin-scattering associated with the field-dependent spin structure, and is consistent with the magnetic anisotropy determined from neutron diffraction studies on bulk $\text{Ca}_3\text{Ru}_2\text{O}_7$ with the easy-axis along the a-axis and b-axis (see the labels in Fig. 3) above and below T_{MIT} , respectively⁵⁵. Note that the MR behavior at $T = 20$ K and 40 K cannot be fitted using a sine-squared function, a feature similar to the out-of-plane MR behavior observed at this

temperature regime⁷⁰, which was attributed to the angle-tuned spin-valve effect that is affected by the change of magnetic anisotropy when T approaches T_{MIT} . For the 8 nm flake sample, besides the smaller T_{N} (~ 42 K) and T_{MIT} (~ 30 K) as discussed above, interestingly, the angular dependence of $\text{MR}(\theta)$ curves display no much variation below and above T_{MIT} . Similar feature is also observed in the 9 nm flake sample. As discussed previously, the magnetic anisotropy in this compound arises from spin-orbit coupling. This implies that, unlike thick or bulk samples where spin-orbit coupling changes below T_{MIT} at which the c-axis compresses and b-axis expands⁷¹, there is no drastic change in spin-orbit coupling as a function of temperature in thinner flakes, potentially associated with the absence of first-order like structural change as inferred from the transport measurements shown in Figure 4.4. Furthermore, owing to the strong spin-charge coupling in ruthenates, the distinction in $\text{MR}(\theta)$ behavior in the 90 nm and 8 nm flakes suggests that their ground states at low temperature possess different magnetic structures. By comparing the $\text{MR}(\theta)$ curves measured at $T = 60$ K depicted in Figure 4.5(d,h), we tentatively denote a and b-axes for the 8nm flake as labeled in Figure 4.5(h).

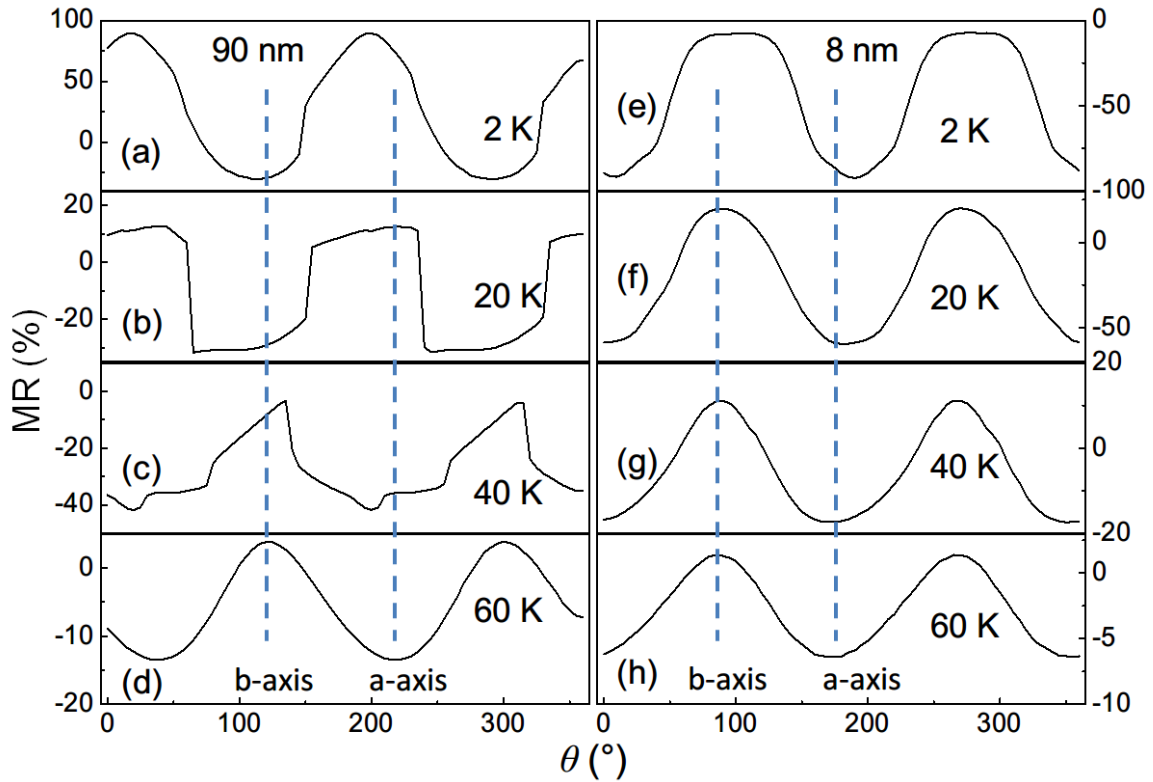


Figure 4.5: The MR comparison as a function of angle of in-plane magnetic field. The left graphs are taken from the 90nm thick flake and the right figure from the 8 nm thin flake. The MR is defined as the percentage change compared with the resistance measured with zero magnetic field. Inset: geometry of the chip (crystal plane) and the rotation of in-plane magnetic field.

The alteration in the magnetic structures as the flakes becomes thinner is supported by the $MR(H)$ measurements. Figure 4.6 presents the $MR(H)$ data measured at various temperatures with the magnetic field applied along both a and b-axes for 13 nm and 8 nm flakes. Note that a and b-axes are determined via $MR(\theta)$ measurements discussed above. For the 13 nm flake, the overall MR behavior is similar to that observed in the bulk sample⁵⁰. As shown in Fig. 4(a), with the magnetic field up to 8 T applied

along the a-axis, which corresponds to the magnetic hard-axis, the flake exhibits positive MR at $T = 2$ K and negative MR at higher temperatures. And with the field applied along the b-axis, i.e., the magnetic easy-axis, a field-induced phase transition is clearly observed, as inferred from the hysteresis loop in MR around 6 T. The similarity in MR(H) data of 13 nm flake to those of the bulk^{55 63} implies that the magnetic structures observed in the bulk highly likely persists in the nanoflakes down 13 nm thick. In sharp contrast, the 8 nm flake exhibits remarkably different MR(H) behavior. For $H // a$ (Figure 4.6(c)), overall the sample displays negative MR at all temperatures measured except that there show a small positive MR around 1 T at $T = 30$ K which is close to the T_{MIT} . The MR magnitude reaches about 90% at 2 K and 9 T, which then decreases monotonically with increasing temperature, which is distinct from the observation on the 13 nm flake shown in Figure 4.6(a). For $H // b$ (Figure 4.6(d)), the MR behavior is also different from that observed in the 13 nm flake. At $T = 2$ K, the MR shows a non-monotonic dependence on the magnetic field, with a dip around 3 T. With increasing temperature, the MR value gradually changes the sign and the dip feature in MR disappears at $T = 30$ K with the MR value at 9 T reaching the maximum followed by a decrease at higher temperature. Again, the drastic distinction in MR between 13 nm and 8 nm flakes reflects the change in magnetic structure as the flake thickness decreases. Very interestingly, it is worth noting that the MR phenomena shown in Figure 4.6(c,d) are quite similar to the MR observed in the bulk Fe-doped $\text{Ca}_3\text{Ru}_2\text{O}_7$ ⁷², which possesses a coexistence of commensurate and incommensurate spin structure at low temperature in the absence of magnetic field⁶² and a field-induced incommensurate-to-commensurate (canted antiferromagnet) magnetic phase transition⁷³.

Finally, we briefly comment the mechanism of the change in the magnetic structure of thinner flakes. Firstly, as discussed previously, the RuO_6 octahedron is compressed along the c -axis in the presence of oxygen loss at the cleaved surfaces, which is expected to change the magnetic structure due to the strong spin-lattice coupling in ruthenates. However, the octahedral compression tends to result in enhanced antiferromagnetic superexchange interactions that can give rise to G-type antiferromagnetic structure as reported in both Ca_2RuO_4 ⁷⁴ and Ti-doped $\text{Ca}_3\text{Ru}_2\text{O}_7$ ⁷⁵. Secondly, the partial reduction of Ru^{4+} to Ru^{3+} due to the loss of oxygen atom can weaken the original ferromagnetic interaction and locally induce the antiferromagnetic interaction between Ru^{4+} and Ru^{3+} , which may consequently lead to an incommensurate magnetic structure. Note that incommensurate magnetic structure has been observed in Fe-doped $\text{Ca}_3\text{Ru}_2\text{O}_7$ due to the competing interactions in combination with magnetic anisotropy and the Dzyaloshinskii-Moriya interaction⁶². Although challenging, future studies using microprobe resonant x-ray diffraction are very desirable to directly probe the nature of the magnetic structure of the nanoflakes as a function of thickness.

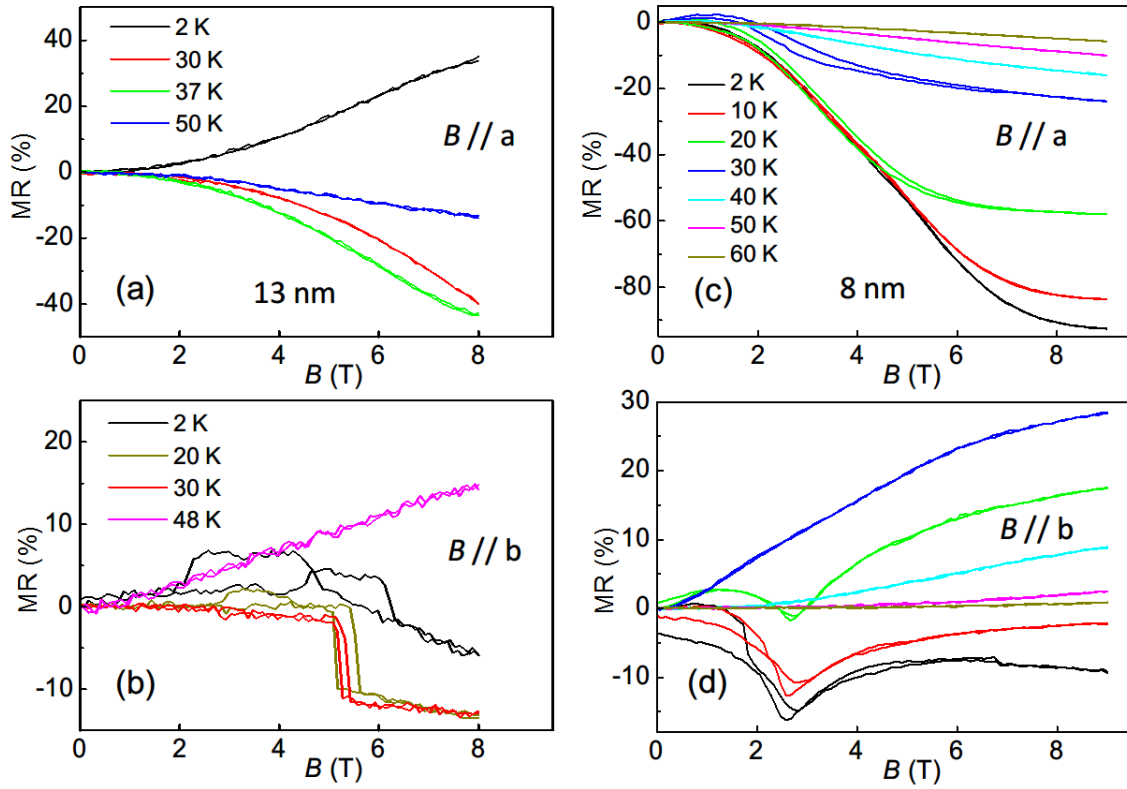


Figure 4.6: MR of 13/8 nm flake as a function of field strength at various temperatures. Left: 13nm flake with the field on b-axis. Bottom left: 13nm flake, field on a-axis. Right: 8 nm flake, field on “b-axis”. Bottom right: 8 nm flake, field on “a-axis”.

It is worth mentioning that the MR behavior in the 9 nm flake (Figure 4.7) is very similar to that of 8 nm flake but with smaller amplitude. The result reinforces the reproducibility of the feature and also the thickness-related origin of the magnetic structure.

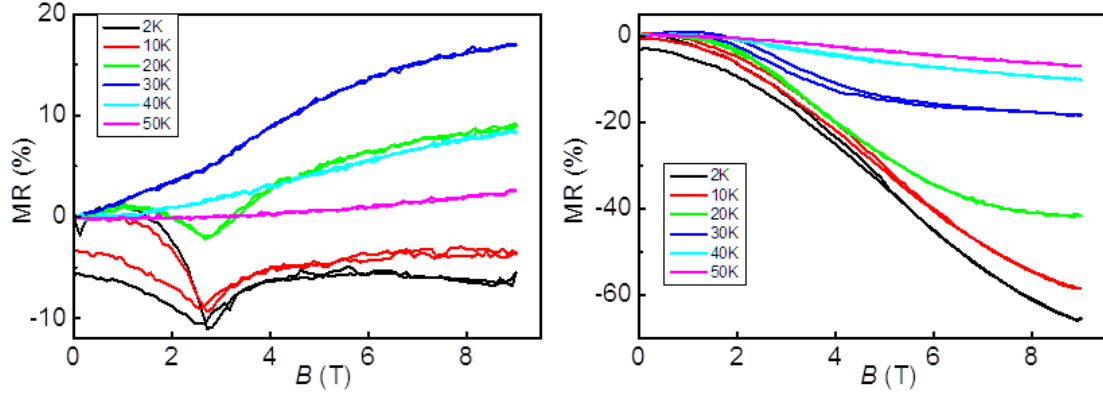


Figure 4.7: The magnetoresistance of 9nm $\text{Ca}_3\text{Ru}_2\text{O}_7$ flake. Left: B parallel to b-axis. Right: B parallel to a-axis.

We also studied in detail on the only measurable insulating flake with thickness = 7 nm, although thus far we could not completely understand our observation on this sample. Figure 4.8 plotted with resistivity in log scale with respect to T or 1/T, which does not follow a simple linear trend in any temperature region. This indicates that the insulating behavior cannot be simply ascribed to thermal activated semiconducting gap ($\rho \propto \exp(\frac{\Delta}{k_B T})$) or Mott's variable range hopping regime in any dimensions ($\rho \propto \exp(\frac{\Delta}{k_B T})^{\frac{1}{d+1}}$) leaving the detailed mechanism of conductance in thinner flakes to be explored more in the future.

Additionally, the MR of the 7 nm flake shown in Figure 4.9 also behaves differently from that of 8 nm and 9 nm flakes. The incommensurate and commensurate magnetic order we proposed in the previous two flakes might be modified further with larger distortion by increased surface-bulk ratio. But at this point there are not enough clues to give a definite picture of the origin of the behavior.

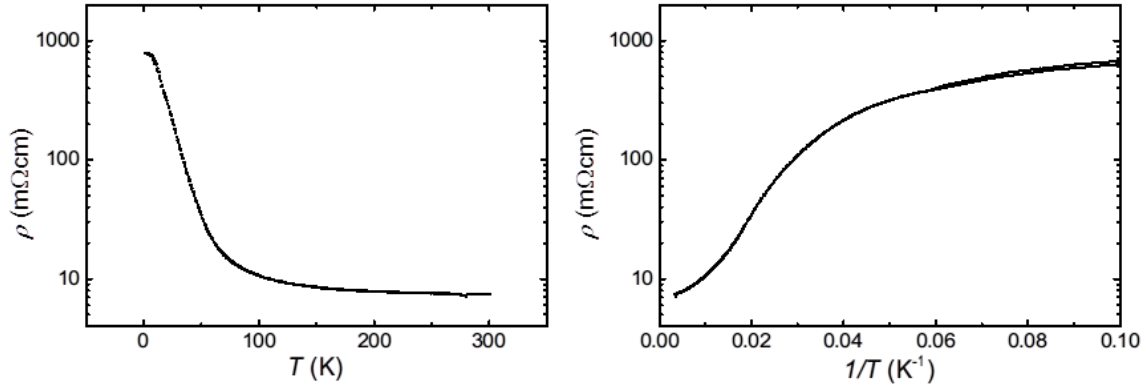


Figure 4.8: The R-T curves of the 7nm flake. Left: The metal-insulator transition disappeared completely and the low-temperature behavior is very insulating. Right: The resistance in log-scale is not linear versus $1/T$.

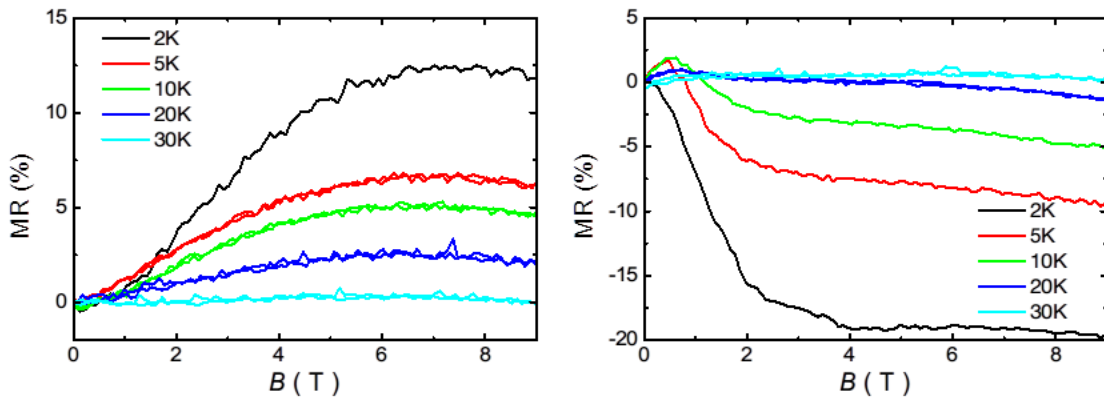


Figure 4.9: The magnetoresistance of the 7nm flake. Left: The hard-axis positive MR is enhanced at low-temperature. Right: The easy-axis negative MR is also larger at lower temperature.

4.4 Lateral dimension effect?

In some of the thicker flakes ($>13\text{nm}$) we observe the re-entrance of the metallic state at low temperature ($<30\text{K}$) similar to the bulk, however, strangely some other flakes (with comparable thickness but narrower) show insulating behavior below T_{MIT} and never

return to metallic again. Thus such an insulating in the narrower flakes should not be ascribed the thickness effect for the very thin flakes below 10nm as we discussed in previous sections. In Figure 4.10 we plotted the R-T curve comparison of two set of flakes for clearance. Two flakes with thickness near 50nm and two near 30nm confirm that the insulating behavior happens in narrow flakes regardless of the thickness. This is interesting because the width of the “narrow” flakes is still several hundreds of nanometers, which is still pretty wide compared to the nanowires people study about the quantized conductance and 1D Peierls transition. We will discuss several possible reasons as follows.

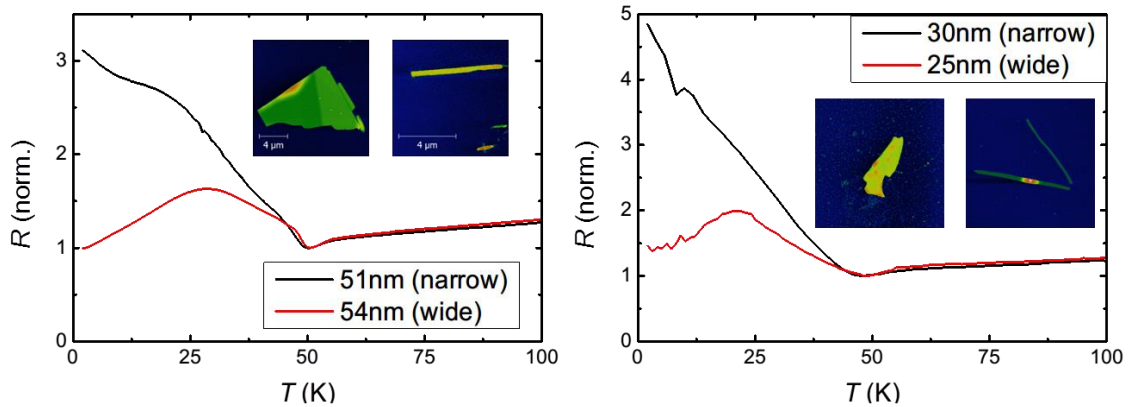


Figure 4.10: The comparison of $\text{Ca}_3\text{Ru}_2\text{O}_7$ flakes with minor difference in thickness but dramatic difference in low-temperature R-T behavior difference. Left: the comparison of 54nm (wide) and 51nm (narrow) flakes. Inset: the AFM images of the two flakes. Right: The same comparison between 25nm and 30nm flakes.

An intuitive guess would be the size of the nanowire that quantizes the conductance of the electrons and prevents the re-entrance of the metallic state. But the

calculation in detail will show that is not possible. Consider that the conductance in near 1D constriction is given:

$$G = \frac{g_s e^2}{h} \sum_{m=1}^{\infty} \theta \left(\frac{W k_F}{\pi} - m \right)$$

Here g_s is the degeneracy of spin = 2, θ is the step function, W is the width of constriction and k_F is the Fermi wavenumber. From the literature the k_F of $\text{Ca}_3\text{Ru}_2\text{O}_7$ at low temperature is estimated to be $\sim 3.2 \cdot 10^8/\text{m}$, which means the unit conductance corresponds to $W \sim 10\text{nm}$. Take a 30nm flake for example, the width of a typical wire-shaped flake is about 200 nm, the conductance of the constriction will be $2 \cdot 20 \cdot e^2/h = 0.001545$, equivalent to 647Ω in resistance. But the value is calculated for a single layer, in $\text{Ca}_3\text{Ru}_2\text{O}_7$ conduction is through quasi-2D bilayers at the low temperature and a 30 nm flake roughly have 30 bilayers. Consider 30 bilayers connected in parallel, the lowest possible resistance value is $\sim 21\Omega$ which is not going to limit the behavior of the flake since the lowest resistance in the actual 30 nm flake at the T_{MIT} exceeds 500Ω .

Even though the quantized conductance seems unlikely to be the reason of the absence of low-temperature metallic state, the calculation does provide some ideas about the effect of width in the constriction. In the literature the origin of the metallic state in bulk $\text{Ca}_3\text{Ru}_2\text{O}_7$ is attributed to the incomplete gapping of Fermi surface arising from a small difference in hopping distances on a and b axes. We are not sure if the anisotropy will be removed in the lateral constriction, but the dimension seems to be too long compared to the thickness to talk about the surface effect. Another possibility left is the phase coherence length of electrons in the system that could probably exceed the width, making the interference in the width direction significant. The interaction might further

gap the Fermi surface and prevent the return of metallic state, but for the present we have too little clue to propose a practical model and examine this observation.

4.5 MIT in Ca_2RuO_4 flakes

The motivation on the study of Ca_2RuO_4 arises from the structural similarity to $\text{Ca}_3\text{Ru}_2\text{O}_7$. The Ca_2RuO_4 has a single RuO_2 layer spaced by Ca^{2+} ions (see Figure 4.11) instead of bilayers in $\text{Ca}_3\text{Ru}_2\text{O}_7$. Thus an interesting question would be: Will the thickness effect be different in Ca_2RuO_4 and $\text{Ca}_3\text{Ru}_2\text{O}_7$ because of the bilayer/single layer? Indeed we would expect even stronger thickness effect in Ca_2RuO_4 because the intra-bilayer bonding is absent so it could possibly be easier for the surface monolayer to relax the distortion imposed by Jahn-Teller effect. Also the effect can be observed by transport measurement because it is also a Mott-insulator with high T_{MIT} (357K)⁷⁶ above the room temperature with an order of magnitude of resistivity change. The transition accompanies with the change of lattice constant⁷⁷ so it occasionally break the crystal. As an possible effect of substrate mismatch strain or decrease in crystallinity, previous studies of the epitaxial thin films often observe broader transition at lower temperature⁷⁸ or the transition completely disappeared⁷⁹. After we established the exfoliation method on the $\text{Ca}_3\text{Ru}_2\text{O}_7$ crystal, we tried to apply this method to the Ca_2RuO_4 crystals as well. And the transport measurement on the 60 nm flake indicates that the MIT transition is preserved.

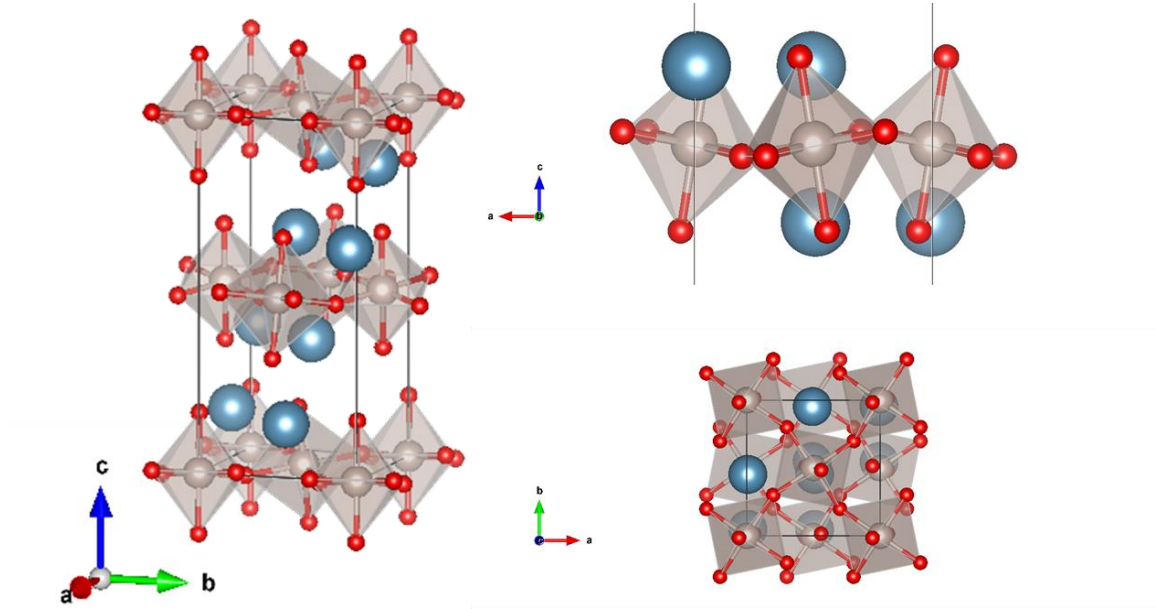


Figure 4.11: Ca_2RuO_4 crystal structure. The unit cell (left), b-axis view (top right) and c-axis view (bottom right) are presented. The crystal has single layer RuO_6 structure instead of bi-layer. The octahedra are still rotated and tilted because of the Jahn-Teller effect.

It turns out that it is much more challenging to obtain Ca_2RuO_4 thin flakes compared to $\text{Ca}_3\text{Ru}_2\text{O}_7$ because of the very small Ca_2RuO_4 crystals that we have. We made the 60 nm flake device (Figure 4.12 (b)) and measured the transport (Figure 4.13) at high temperature. The transition is very similar like the bulk crystal confirming the quality of exfoliated flake is comparable with the bulk single crystal without the strain effect in the epitaxial thin films even though the flake is not quite flat. It is worth noting that the resistivity of the flake is much smaller than the bulk. The literature⁷⁶ reports that the resistivity of the crystal is on the order of $100 \text{ } \Omega \cdot \text{cm}$ at room temperature which is not very different from our bulk measurement. But the resistivity of the flake is on the order of $0.1 \text{ } \Omega \cdot \text{cm}$ which is 3 orders smaller that cannot be explained by geometrical effect or

any mistake in estimation of the shape. We observed low resistivity on most of flakes but they are not very consistent with each other in the R-T. A more systematic study of this material is needed for a conclusion.

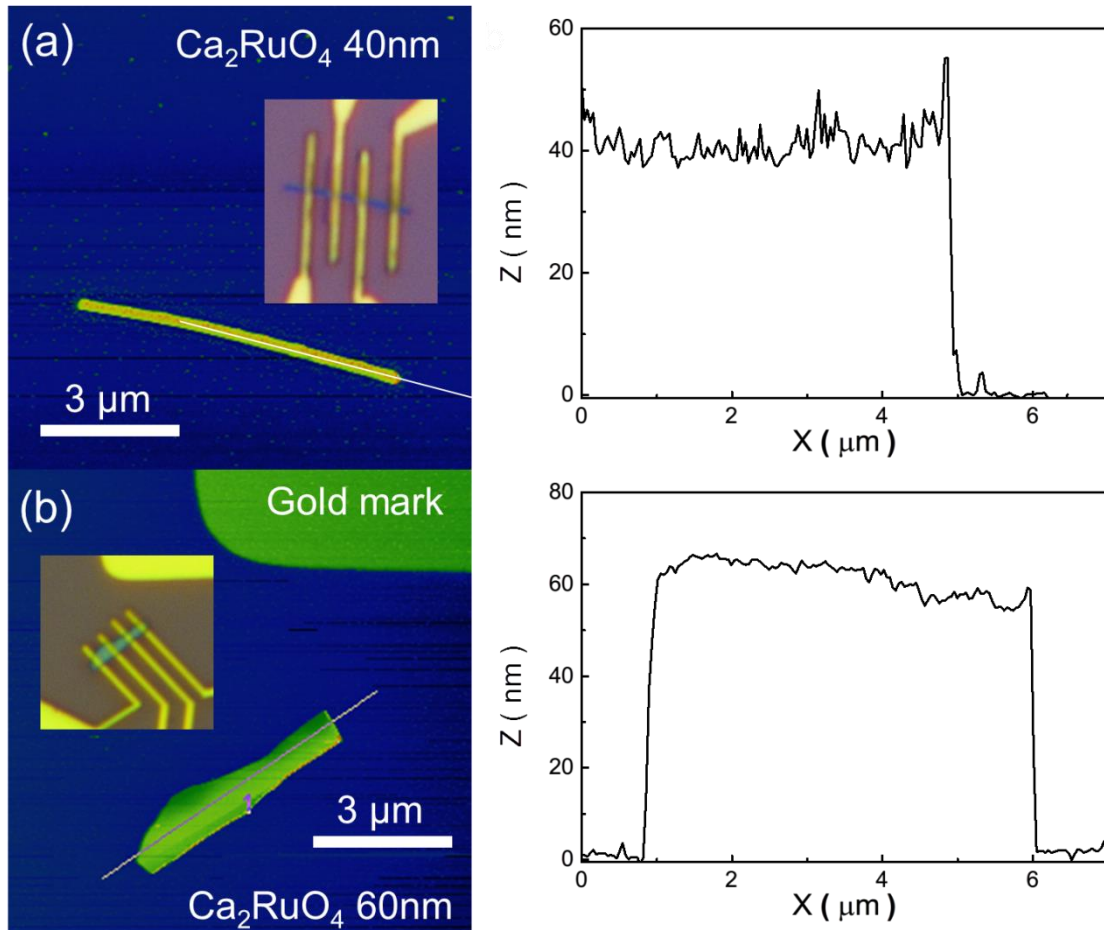


Figure 4.12: Ca_2RuO_4 images of devices. (a) The AFM image and cross-section of the white line of the 40nm flake showing the flake is a flat narrow wire. Inset: the image of fabricated device. (b) The AFM image and cross-section of the 60nm showing the flake is slightly tilted.

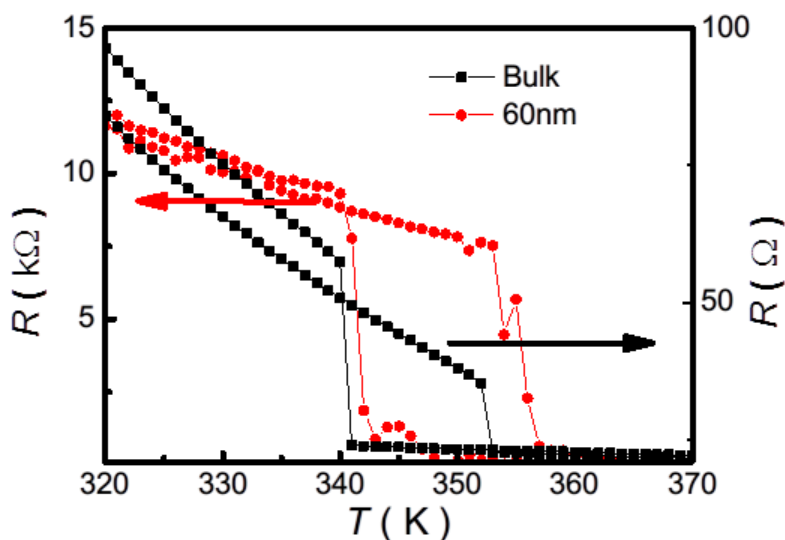


Figure 4.13: The comparison of R-T curve of the bulk and 60nm flake around the transition temperature. The red curve corresponds to the flake and the resistance value in kilohms is on the left, and the black bulk curve is on the right.

4.6 Summary

In summary, we report the electronic transport properties of mechanically exfoliated $\text{Ca}_3\text{Ru}_2\text{O}_7$ nanoflakes as a function of thickness. We show that thin flakes below 10 nm become more insulating and the magnetoresistance behavior is drastically different from that of the thicker samples, implying a change in both electronic state and magnetic order. Such a change may be associated with the enhancement in RuO_6 octahedral distortion and weakening of ferromagnetic interaction due to the loss of oxygen at the cleaved surfaces, whose contribution to the physical properties becomes

more significant as the surface-to-volume ratio increases in the thinner flakes. This study not only brings another dimensionality to control the physical properties of ruthenates, but also in general establishes the marriage between correlated electron systems and two-dimensional materials.

There are two side projects with great potential of further discoveries. One is the lateral dimension constriction effect on the low-temperature metallic state in $\text{Ca}_3\text{Ru}_2\text{O}_7$ nanoflakes which cannot be explained simply by the quantization of conductance based on the Fermi wavenumber estimated. The other one is the study on exfoliated Ca_2RuO_4 nanoflakes which needs more samples for examination. This research has proven the possibility of exfoliation of layer-structured material with tight interlayer binding showing dramatic changes of the physical properties of thin flakes. The result may bring more understanding of the intrinsic properties related to the dimensionality in correlated systems, motivating further studies of the combination of correlated systems and 2D materials.

Chapter 5

Properties of Fe_{1+y}Te thin flakes

In this chapter we are going to discuss the main result from exfoliated Fe_{1+y}Te flakes. The material properties and a brief review of $\text{Fe}(\text{Se},\text{Te})$ system will be given in Section 5.1. Characterization of Fe_{1+y}Te flakes and devices are in Section 5.2. In Section 5.3 we will discuss the broadened transition and superconductor-like feature observed in flakes with intermediate thickness. In very thin flakes, the insulating behavior and enhanced magnetoresistance are described within variable range hopping (VRH) regime in Section 5.4. And prior to the summary, we discuss a mini side project in Section 5.5 about the superconducting $\text{FeSe}_{0.5}\text{Te}_{0.5}$ flake and the application of ionic liquid gating.

5.1 Introduction:

Iron-based superconductors have been intensely researched since the discovery of superconductivity in iron pnictides LaOFeP ^{80 4}, mainly stimulated by the close correlation between the superconductivity and the magnetic correlation. Among the various types of iron pnictide and ion chalcogenides^{81 82 83}, including 1111 (RFeAsO , $\text{R} = \text{La}, \text{Ce} \dots$), 122 (AFe_2As_2 , $\text{A} = \text{Ba}, \text{Sr}, \text{Ca}$ and K), 111 (AFeAs , $\text{A} = \text{Li}, \text{Na}$), and 11 ($\text{FeTe}_{1-x}\text{Se}_x$) families, the $\text{FeTe}_{1-x}\text{Se}_x$ series possesses the simplest crystal structure composed of edge-sharing $\text{Fe}(\text{Te},\text{Se})_4$ tetrahedra layers (Figure 5.1)^{84 85 27 86} and attracts a lot of attention⁸⁷. At ambient pressure, one of the end members, FeTe , exhibits antiferromagnetic metallic ground state with the Neel temperature $T_N = 65 \text{ K} \sim 75 \text{ K}$ (which occurs concurrently with the tetragonal-orthogonal structure phase transition)^{27,85};

the other end member, FeSe, becomes superconducting below the transition temperature $T_c \sim 8$ K without the presence of preceding magnetic phases^{27,84-86}, which arises from the increase of Fe-Se-Fe bond angle of FeSe compared to that of FeTe. Various approaches, such as chemical substitution (Figure 5.2)^{88,89,90,91} and pressure⁹², have been applied to bulk $\text{FeTe}_{1-x}\text{Se}_x$ in order to enhance the superconducting phase transition temperature as well as to better understand the mechanism of the unconventional superconductivity in the iron based systems.

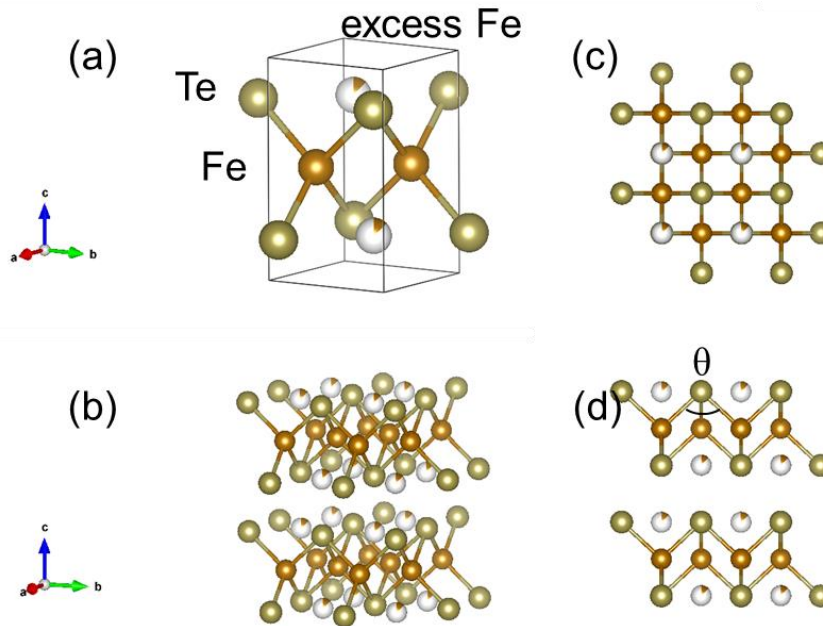


Figure 5.1. The structure of Fe_{1+y}Te . (a) unit cell of Fe_{1+y}Te . The Fe atoms sit in the center of the layers, surrounded by Te atoms forming FeTe_4 tetragons. The empty sphere with a colored section is the site of excess iron. (b) Fe_{1+y}Te layer structures. (c) top view of the crystal. Fe atoms show checkboard patterns. (d) a-axis view of the crystal. The bonding angle of Fe-Te-Fe which will be a key parameter in thin flakes is labeled θ here.

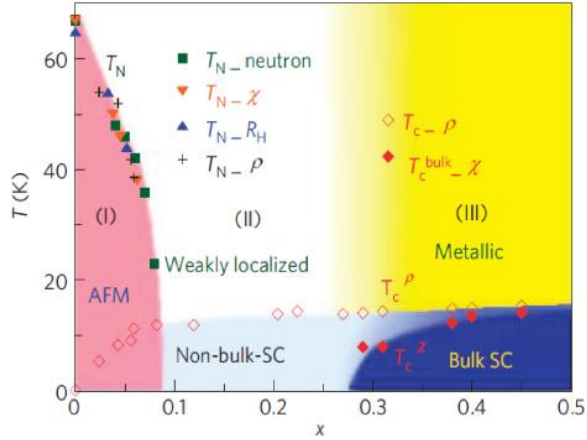


Figure 5.2: Phase diagram of $\text{Fe}(\text{Te}_{1-x}\text{Se}_x)$. Small number of Se doping breaks the AFM state and leads to superconductivity. (From T. J. Liu et al., Nat. Mater. 9, 716 (2010))

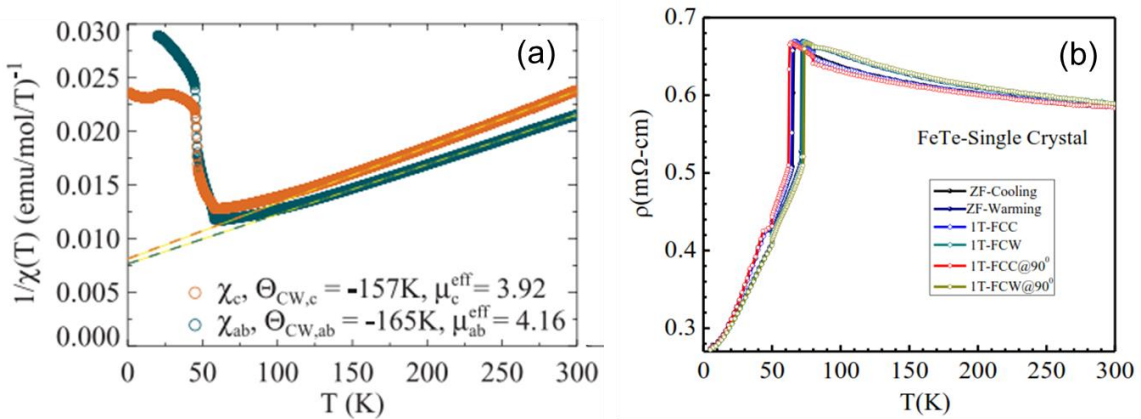


Figure 5.3: The bulk properties of Fe_{1+y}Te crystal. (a) The inverse χ curves indicate a clear AFM transition and the Curie-Weiss linear asymptotic at high temperature. (From I. A. Zaliznyak et al., Phys. Rev. B (2012)) (b) The resistance-temperature plots of bulk Fe_{1+y}Te crystal show the semiconductor-metal transition and a sharp drop of resistance.

Recently, significant efforts have been invested on FeSe in the epitaxial thin film form as well as in the mechanically-exfoliated thin flake form, which have not only unraveled novel phenomena that are distinct from the physical behavior observed in the

bulk counterpart, but also provided unprecedented insight into the nature of the superconductivity in bulk. For instance, it was discovered that T_c of FeSe monolayer grown on various substrates can be dramatically enhanced^{93,94,95,96,97,98,99}, e.g., $T_c \sim 109$ K for FeSe monolayer deposited on SrTiO₃ substrates⁹⁹. Interestingly, beyond the monolayer of FeSe, the superconductivity gets suppressed in FeSe thin films¹⁰⁰ and even exhibits an insulator-like behavior for relatively thin films while thicker FeSe films behave like the bulk sample¹⁰¹. Various mechanisms^{93-97,101,102,103,104}, such as electron-phonon coupling and charge transfer from substrates, phonon softening or structural modification induced by the lattice mismatch between the monolayer and the substrate, have been put forward to account for the change in T_c . Alternative to thin film growth, when being exfoliated down to nanometer thick, it is found that exfoliated FeSe thin flakes (~ 10 nm) still show metallic and superconducting behavior³², in contrast to the insulating behavior observed in FeSe thin films¹⁰¹. Furthermore, T_c of thin FeSe flakes is significantly enhanced upon ionic liquid gating, which has been ascribed to the change of the dominant carriers from holes to electrons³².

In contrast, relatively fewer studies of nanostructured Fe_{1+y}Te have been reported. It was found that tensile strain of epitaxial Fe_{1+y}Te films softens the first-order magnetic and structural phase transition observed in bulk (Figure 5.3), followed by an emergence of superconductivity upon further decreasing temperature due to the strain-induced increase of Fe-Te-Fe bond angle³¹. However, Nie et al reported that superconductivity was only induced in Fe_{1+y}Te films by incorporation of oxygen via low temperature thermal annealing³⁰. More recently, scanning tunneling microscopy/spectroscopy study has revealed interfacial superconductivity in Fe_{1+y}Te monolayer grown on a topological

insulator Bi_2Te_3 which coexists with the same antiferromagnetic order as the one observed in bulk Fe_{1+y}Te ¹⁰⁵. These studies raise a fundamental question of what happens to the electronic and magnetic properties of nanostructured Fe_{1+y}Te , i.e., exfoliated Fe_{1+y}Te nanoflakes, in the absence of epitaxial strain or interfacial charge transfer.

5.2 Fe_{1+y}Te nanoflake devices

Fe_{1+y}Te ($y = 0.15$) bulk single crystals were grown using a flux method⁸⁹. Nanoflakes of this material were prepared by mechanically exfoliating bulk crystals using Scotch tape method and then transferred to the pre-patterned SiO_2 (285 nm)/Si substrates. Flakes with various thickness ranging from ~ 10 nm up to ~ 100 nm were located under an optical microscope right after exfoliation, and then the topology was measured using the atomic force microscope (AFM). To reduce air exposure, samples were covered by spin-coated photoresist after AFM measurements such that the typical exposure time did not exceed 1 hour after exfoliation. Nanoflake devices with four-terminal electrode pattern were fabricated using the standard e-beam lithography procedure described in Chapter 2. Ohmic contacts were formed by depositing 10 nm Ni (used as the adhesive layer) and 100 nm Au electrodes by DC sputtering, preceded by an *in-situ* ion-milling to remove ~ 2 nm of Fe_{1+y}Te over the contact area which may be oxidized due to the air exposure. Electronic transport measurements were carried out using Quantum Design PPMS cryostat.

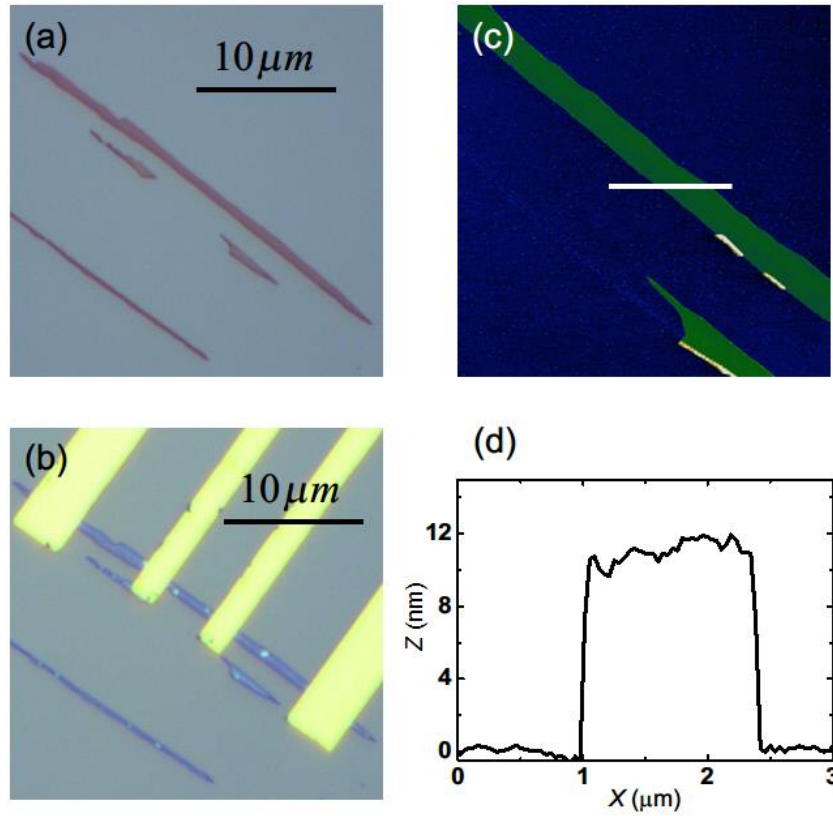


Figure 5.4: Images of an 11 nm exfoliated Fe_{1+y}Te flake. (a, b) 100X Optical images before and after metal electrode deposition. (c, d) Atomic force image and the cross-section profile of the 11 nm flake. The thickness can be determined within ± 1 nm.

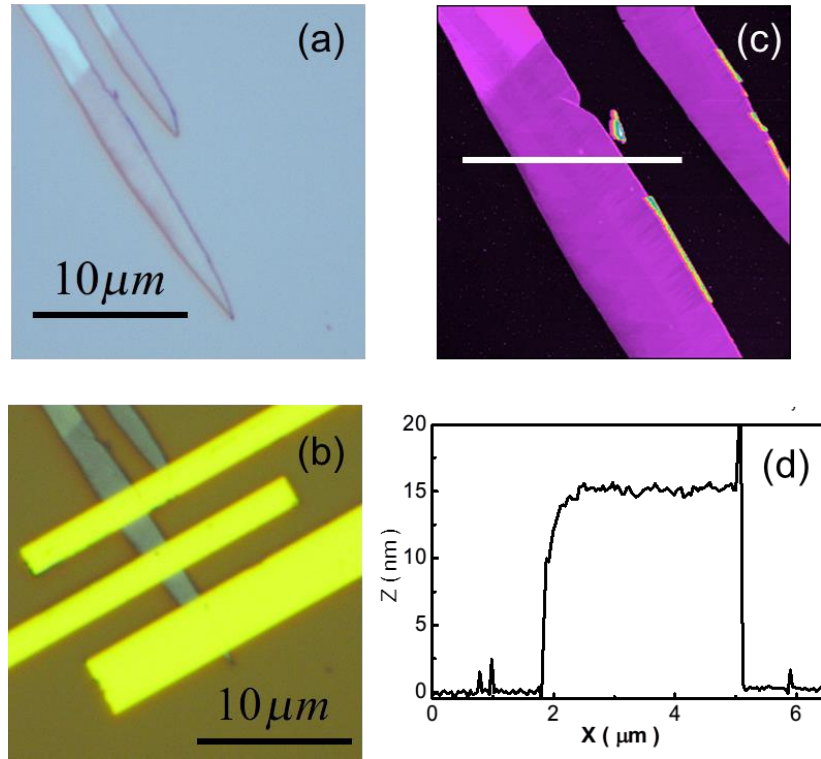


Figure 5.5: The images of 15nm Fe_{1+y}Te flake. (a,b) optical images before and after device fabrication. There are actually four electrodes but the other current lead is out of the view. (c,d) the AFM images and profile of cross-section.

Figure 5.4, 5.5 (a-b) display the optical images of 11 and 15 nm exfoliated flakes with and without patterned electrodes respectively, and Figure 5.4, 5.5(c-d) present the AFM images and the line scan profiles of the same flake, showing a flat surface topology with $\sim 1\text{nm}$ roughness.

Although it would be nice to have some lattice information through non-destructive optical measurement, but unfortunately Raman spectroscopy in air is not a good way to probe these Fe_{1+y}Te flakes. We have tried to take the Raman spectra of

Fe_{1+y}Te flakes right after the exfoliation, but the peaks of the intrinsic phonons are always overwhelmed by signals from degraded layers, as the same mentioned in [106] (Figure 5.6 Right). Figure 5.7 shows the typical Raman spectrum we have for Fe_{1+y}Te flakes.

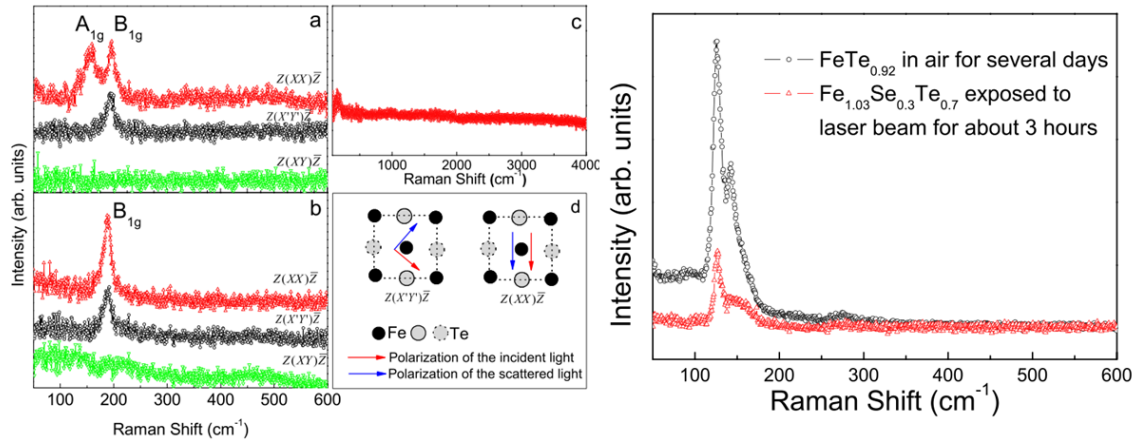


Figure 5.6: Raman modes of Fe_{1+y}Te crystal. Left: (a,d) Fe_{1+y}Te Raman spectra with various geometry where A_{1g} and B_{1g} should both present in parallel geometry and only B_{1g} will present in $Z(X'Y')\bar{Z}$ geometry. Right: The spectra of aged or long irradiated crystal shows strong peak at $\sim 150\text{cm}^{-1}$ and Raman modes are not distinguishable. (From Xia, T. L. et al. Phys. Rev. B - Condens. Matter Mater. Phys. 79, 1–4 (2009).)

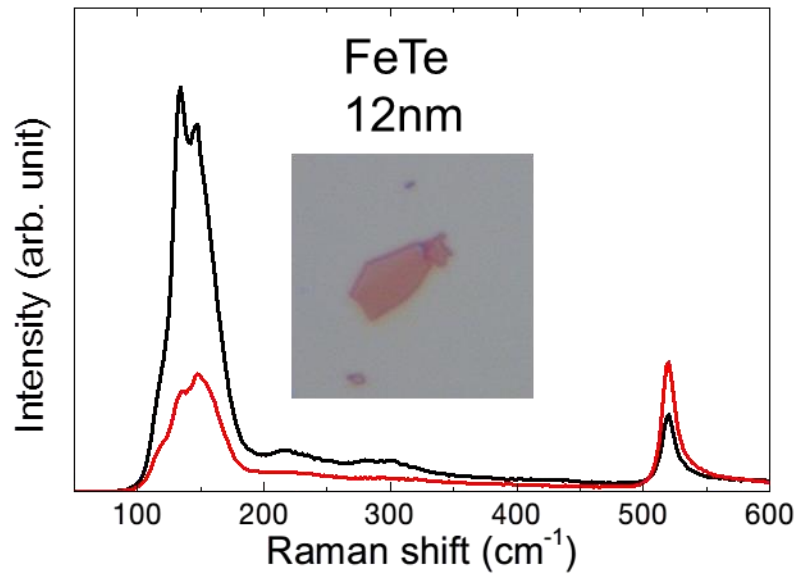


Figure 5.7: Raman spectra of a 12nm Fe_{1+y}Te flake. The black curve is taken with parallel Z(XX)-Z geometry and the red curve is with orthogonal Z(XY)-Z geometry. The Raman peaks are not observable in the strong background peak similar to degraded crystal. The peak at 520cm^{-1} is from Si background.

After device fabrication, I-V measurements between any two probes of the devices show linear behavior and the resistance values measured between any two electrodes are scalable with their separation (Figure 5.8), affirming ohmic contacts with negligible contact resistance. It is worth mentioning that two-probe measurements on devices without the ion-milling step prior to electrode deposition tend to show non-linear I-V character below 100 K, which suggests the importance of the *in-situ* ion-milling process (details described in Chapter 3).

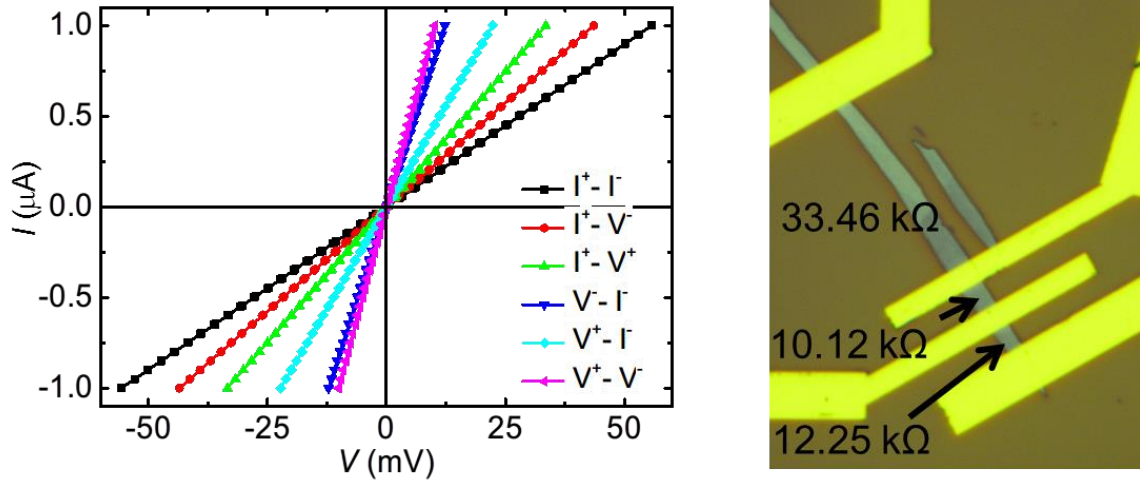


Figure 5.8: The I-V curve of the 15nm flake measured at 10K (without magnetic field.) The linear curves determine the resistance between each two probes as depicted on the right. And the resistance between two current leads is 55.69 k Ω , meaning the contact resistance is on the order of \sim 100 Ω which is negligible to the 4-probe resistance value we measured.

5.3 Superconductor-like intermediate thin flakes

Figure 5.9 depict the measured resistivity (ρ) as a function of temperature (T) of devices with typical flake thickness. One can see that the thicker flakes (e.g., 84 nm) shows a sharp semiconducting-metallic feature around 62 K, a feature which is also observed in bulk Fe_{1+y}Te and corresponds to the paramagnetic-antiferromagnetic phase transition that occurs simultaneously with tetragonal-orthorhombic structural phase transition^{89,107}. For the intermediate thickness range (e.g., 25 nm flake), such a semiconducting-metallic transition becomes broadened, as shown in Figure 5.3(b). In addition, there is a sharp drop in resistivity occurring below 10K, as seen in the inset. Such a feature is observed, although weaker, on devices with 27 nm and 30 nm flakes too, and resembles the onset of superconducting transition found in the FeTe thin films^{31,30,40}

or even bulk crystals¹⁰⁸. Note that the kink point around 10 K shifts slightly to lower temperature upon applying 9 T magnetic field, affirming the superconducting transition.

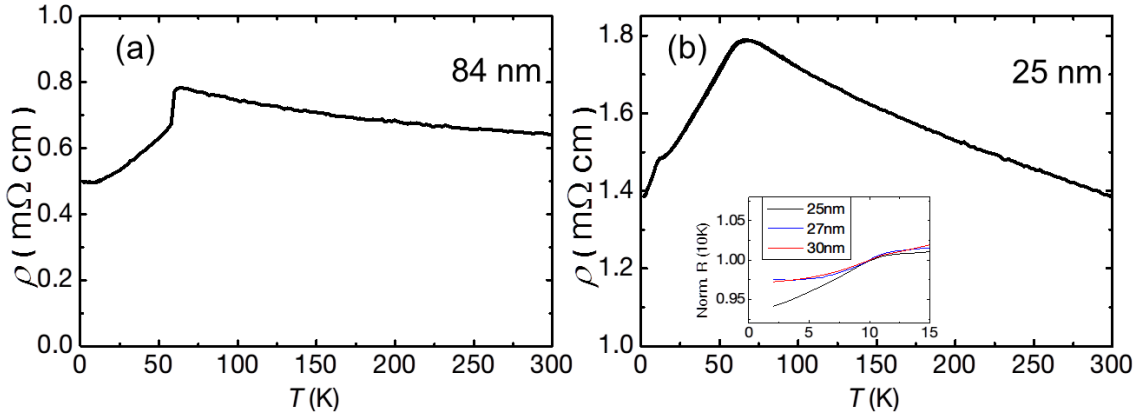


Figure 5.9: R-T curve of thick and intermediate flakes. (a) The R-T curve of the bulk-like flake (84nm) shows the transition similar to the bulk material. (b) The R-T curve of intermediate-thickness flake (25nm) shows broadened transition and a dip at 10K signatures the onset of superconductivity.

As discussed above, two different scenarios have been proposed to account for emergence of superconductivity in FeTe: one is due to the change of Fe-Te-Fe bond angle arising from the tensile strain in thin films³¹, and the other is due to the oxidization which changes the valence state of Fe 3d electrons and may suppress the local magnetic moment and enhance the carrier itinerancy^{30,108}. However, it is likely that the superconducting-like feature observed in the flakes with intermediate thickness is not ascribable to aging or oxidation of the samples, as it is present only for devices with intermediate thickness (e.g. see Figure 5.9 (a)) but absent for the devices with thicker

flakes. To further affirm this, we purposely baked the 25nm flake several times including in-situ and in air at 100°C for an hour and found that the overall features of the $\rho(T)$ curves did not change after all, except an increase in resistivity (Figure 5.10).

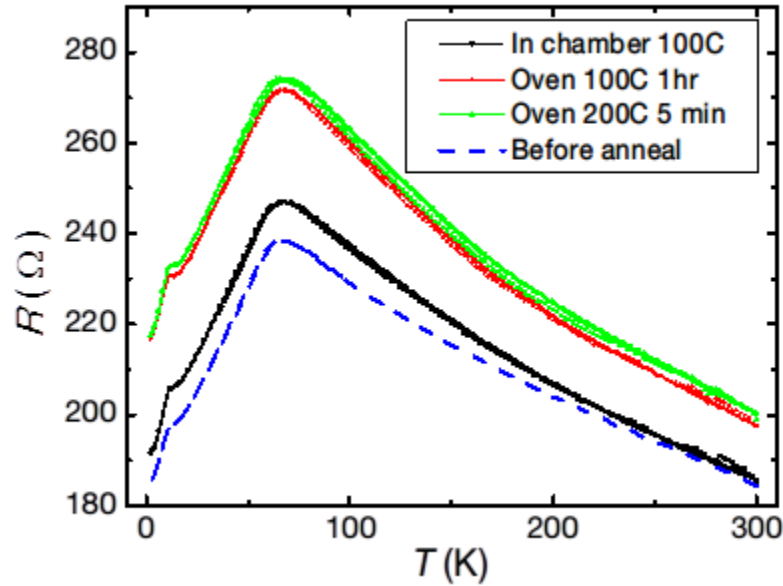


Figure 5.10: The increase of resistance over several baking process. After the first measurement without baking (blue-dashed line), the sample went through (1) in-situ 100°C baking for 2 hours (2) in air 100°C baking for 1 hour (3) in-air 200°C for 5 min. and R-T curves were measured after each process.

Instead, the appearance of the superconducting-like feature in the devices with flakes of intermediate thickness may presumably associate with the change of crystal structure. For exfoliated flakes with thin enough thickness, the absence of constraints on both surface and interface likely relaxes (partially) the structural distortion towards the ideal FeTe_4 tetrahedral structure by enlarging the in-plane lattice parameters. This results in an enhancement of Fe-Te-Fe bond angle, similar to that observed in the thin films with

tensile epitaxial strain³¹, leading to the broadening/smearing of the structural transition observed around 60 K and the onset of superconducting-like behavior^{31,40}.

5.4 VRH model in ultra-thin flakes

Interestingly, with further decreasing the thickness, both structural phase transition and the superconducting-like features are absent and the flakes becomes more insulating, as shown in Figure 5.11(a) for the 11 nm flake. The evolution of $R(T)$ of flakes with various thickness is presented in Figure 5.11 (b). The absence of superconducting-like feature in the thinner flakes originates from the predominant charge-carrier localization as the dimensionality reduces, which will be discussed next.

The rapid increases in resistivity observed in thinner Fe_{1+y}Te flakes can be associated with charge-carrier localization due to the excess of Fe, and the transport behavior can be well captured by the variable range hopping (VRH) model¹⁰⁹.

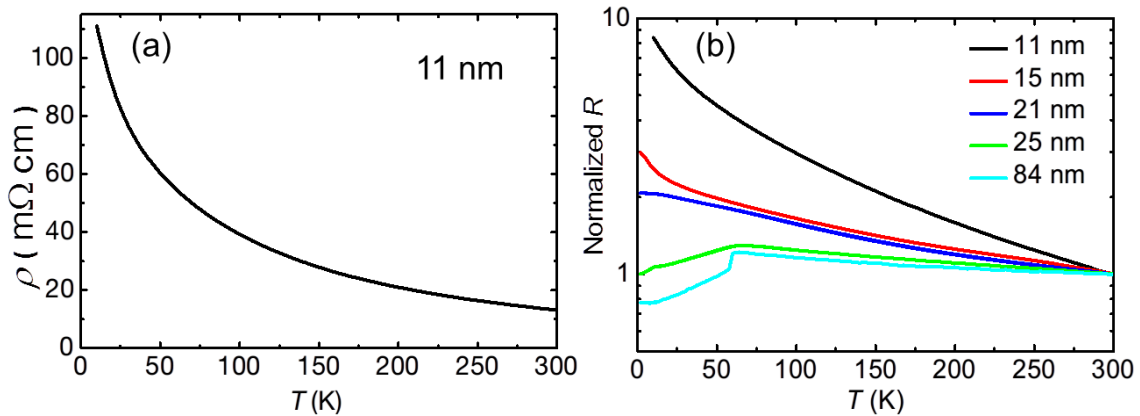


Figure 5.11: R-T curves of thin insulating flakes. (a) The R-T curve of 11nm flake showing the insulating behavior and the absence of both AFM transition and superconductor-like dip at 10K. (b) The evolution of R-T behavior in various thickness of Fe_{1+y}Te flakes. R is normalized to $R(300\text{K})$ and plotted in log-scale to contain the changes in orders.

Within this model, the charge-carriers in a highly disordered system hop between impurity sites with a variable hopping distance instead of fixed distance in normal crystals, and the electronic conductance can be fitted using the equation $\sigma(T) = \sigma_0 + A \exp(-(\frac{T_0}{T})^{\frac{1}{1+d}})$, where T_0 is the hopping parameter that is related to the localization length ξ of charge-carriers and d is the dimensionality of the sample. To validate if the VRH mechanism is applicable to Fe_{1+y}Te thin flakes, we fit the conductance-temperature $\sigma(T)$ curve of the 15 nm flake using the aforementioned equation, as shown in Figure 5.12(a). One can see that the VRH model fits the $\sigma(T)$ curve below 50 K very well, with the fitting parameter $d = 2$ reflecting the two-dimensional nature of the nanoflakes and $T_0 = 147$ K. Considering that $\xi = (13.8/k_B D T_0)^{\frac{1}{2}}$ ^{110,111}, where D is density of states, one can calculate the localization length ξ . Taking the effective mass $m^* = 3m_e$ obtained from the ARPES experiments¹¹², $D = \frac{m^*}{\pi \hbar^2}$ (neglecting the valley degeneracy) is calculated to be $1.25 \times 10^{15} / \text{eV} \cdot \text{cm}^2$, which gives $\xi = 9.34$ nm. Indeed there are three different mass enhancement on different carrier pockets, and $3m_e$ is the one estimated with the hole pocket. In bulk FeTe the two types of carriers coexist in the system, while below the transition electron-type carriers get largely enhanced and drive the system metallic⁴⁰, but at low temperature we did not observe this transition in very thin flakes and the behavior is quite insulating. Though the exact carrier composition in highly disordered flakes cannot be examined in our devices, since the systems show non-metallic properties it should be reasonable to assume those electron-type carriers are

largely suppressed and the conduction of current is through hole-type carriers. It is known that in Te-rich Fe(Te,Se) the presence of excess Fe leads to enhanced incoherent magnetic scattering and results in charge-carrier localization^{89 33}. Thus, while the charge-carrier localization due to the excess Fe yields to the metallic behavior in bulk/thick Fe_{1+y}Te at low temperature, it is anticipated that the effects of charge-carrier localization becomes more prominent in thin flakes with reduced dimensionality when the localization length is comparable to the flake thickness, i.e, being essentially a disordered two-dimensional system which exhibits localized states that can be well described using the VRH model.

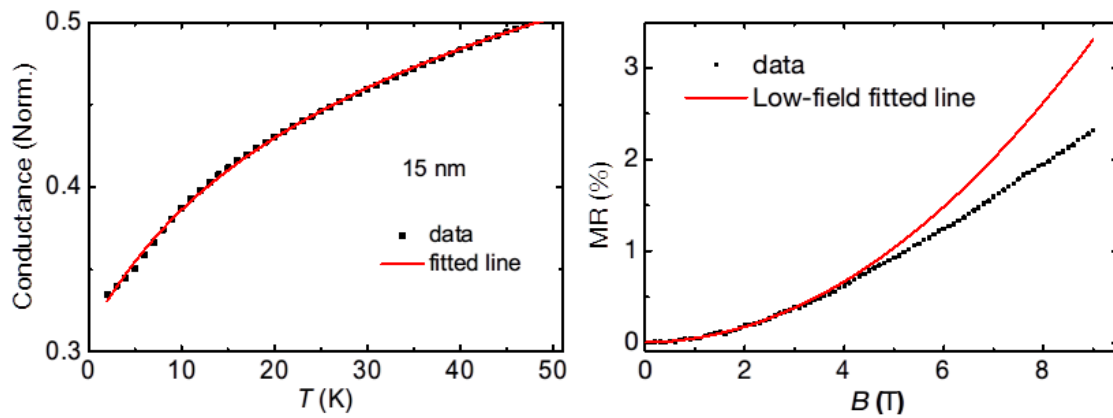


Figure 5.12: Fitting of VRH model (a) The zero field conductance σ (normalized to the value at 300 K) vs T and (b) the magnetoresistance MR data at $T = 2$ K for the devices on the 15 nm flake. The scatter points are experimental data and the red solid curve is the fit using the variable range hopping model described in the main text.

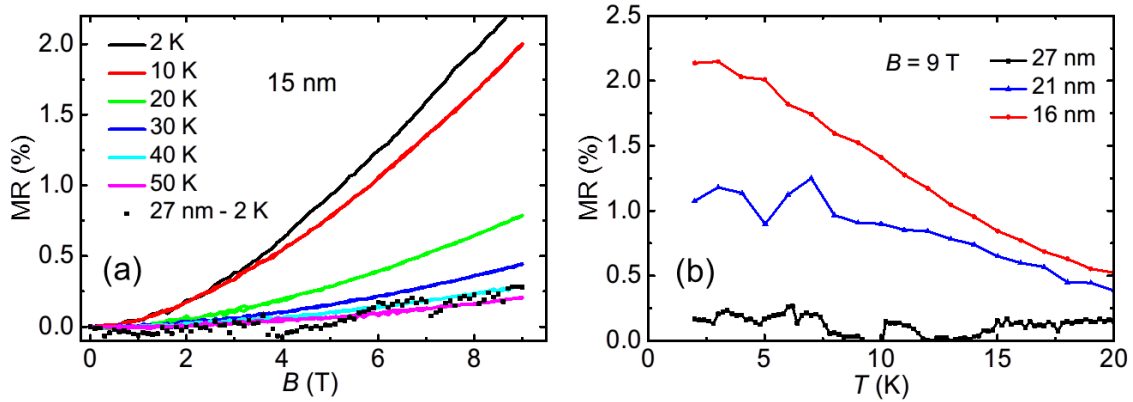


Figure 5.13: Comparison on MR. (a) The magnetoresistance of 15nm Fe_{1+y}Te flake at various temperature. In comparison of the largely enhanced MR the 27nm data at 2K is also plotted in the same graph. (b) The MR at 9 Tesla as a function of temperature of different samples. MR decreases quite fast with increasing temperature and thickness.

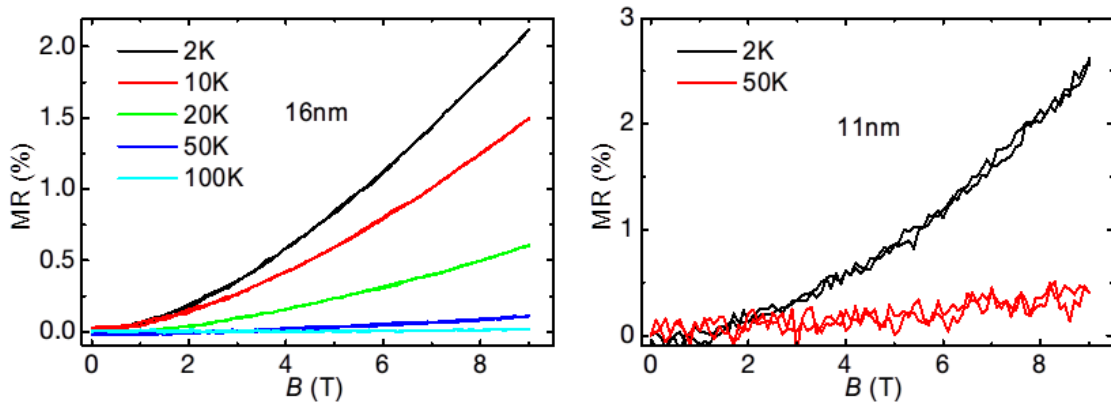


Figure 5.14: Magnetoresistance of 16nm and 11nm Fe_{1+y}Te flakes. The magnitude of MR is similar to 15nm flake. The 11nm flake curve is more noisy than the other two since the contact is less stable due to very insulating state at low temperature.

Figure 5.13 presents the magnetoresistance (MR), which is defined as $[R(B)-R(0)]/R(0)$, for insulating thin flakes ($t = 15 \text{ nm}$). There are two features worth pointing

out. First, compared to the MR value of thicker and metallic films (e.g., $t = 27$ nm), the MR of thinner and insulating flakes are largely enhanced. For instance, MR measured at $B = 9$ T and $T = 2$ K exceeds 2% for the 15 nm flake while MR is $\sim 0.5\%$ only for the 27 nm flake. And the MR decreases with increasing temperature, as shown in both Fig. 5.13(a) and Fig. 5.13(b). Second, interestingly, the MR value is positive and scales quadratically on magnetic field in the low field region, and such MR behavior can be attributed to the shrinkage of the overlap of the tails of wave functions of localized states in the VRH regime¹¹³. The similar behavior is observed also in 16nm and 11nm flakes (Figure 5.14). Within this model, MR depends on B^2 , $\frac{\Delta R}{R(0)} = \frac{R(B)-R(0)}{R(0)} = \frac{B^2}{B_0^2}$, with $B_0^2 = \left(\frac{\alpha\hbar^2}{e^2\xi^4}\right)\left(\frac{T}{T_0}\right)^{3/2}$ where $\alpha \approx 6.6 \times 10^2$ is a numerical constant. Based on the obtained localization length ξ ($= 9.34$ nm) and the hopping parameter T_0 ($=147$ K) discussed above, B_0 is calculated to be $B_0^{\text{cal}} \sim 39$ T at $T = 2$ K. By fitting the MR data ($0 < B < 3$ T) as shown in Fig. 5.12(b), we get the quadratic dependence $B_0^{\text{exp}} = 48$ Tesla, which is comparable to the calculated B_0^{cal} and thus affirms the validity of the VRH model in describing both $\sigma(T)$ and MR data in our system.

Finally, we would like to briefly comment on the thickness dependent transport behavior in Fe_{1+y}Te nanoflakes and raise a few interesting questions. Is there an antiferromagnetic order in the thinner flakes (thinner than 21 nm)? If so, would the magnetic order occur with potential structural phase transition, if the latter does exist as well? If there was no magnetic and structural phase transition in the thinner flakes, what would be the driving force for their absence? Future in-situ Raman scattering study is desirable to address these questions. Furthermore, it would be interesting to explore ionic

liquid gating on Fe_{1+y}Te nanoflakes to examine potential carrier doping-induced superconductivity as what has been recently reported on nanostructured FeSe ^{101 32}.

5.5 Exfoliated $\text{FeSe}_{0.5}\text{Te}_{0.5}$ flakes and ionic liquid gating

The motivation on studying the properties of exfoliated superconducting flakes of $\text{Fe}(\text{Se},\text{Te})$ comes from two studies shown in Figure 5.15 and Figure 5.16. The first one is the evolution of the transport properties in exfoliated $\text{FeSe}_{0.5}\text{Te}_{0.5}$ as a function of thickness, which indicates that the thin flakes start showing semiconducting behavior as the thickness decreases and eventually the superconductivity disappears for flakes with thickness 12nm and below³³. The researchers argued that the inhomogeneity of Se and Te atoms in thin flakes caused the inhomogeneous superconducting regions in the flake and the regions cannot form continuous path when the thickness is below a certain length. On the other hand, the ionic liquid gating effect study of the FeSe thin flakes (Figure 5.16) with thickness $\sim 10\text{nm}$ shows the application of positive gate voltage (which should draw negative charges on the sample surface) dramatically increases the T_c and at the same time reversing the Hall number (n_H)³². The study implies the close relationship between the superconductivity in FeSe and the heavy doping of electron-type carriers. These studies raise a question: Can we also increase T_c in $\text{FeSe}_{0.5}\text{Te}_{0.5}$ flakes by heavy electron doping using ionic liquid gating?

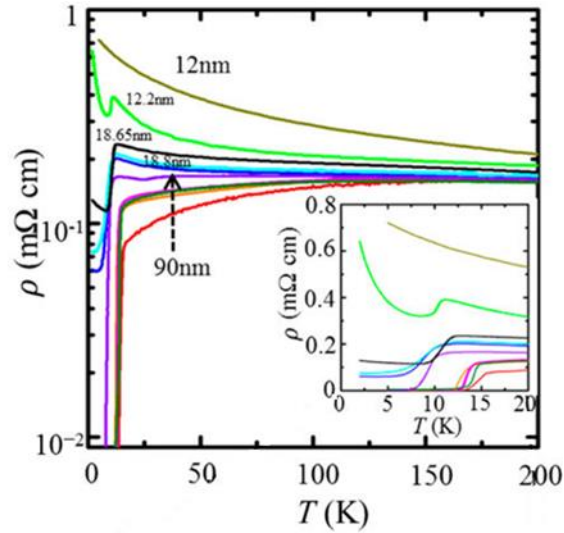


Figure 5.15: The evolution of superconductivity in exfoliated $\text{FeSe}_{0.5}\text{Te}_{0.5}$ flakes. The superconductivity is completely suppressed in flakes with thickness = 12nm or lower and the R-T curve shows insulating behavior.

(From Yue, C. et al. ACS Nano 10, 429–435 (2016))

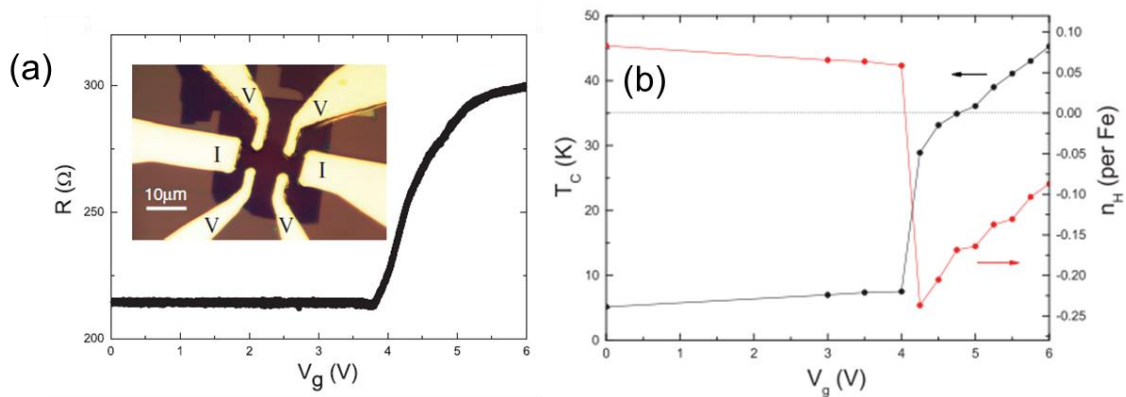


Figure 5.16: The ionic liquid gating effect study on FeSe exfoliated flakes.

(a) The optical image of the device with thickness $\sim 10\text{nm}$ and the R- V_g curve. (b) T_c and Hall number as a function of V_g . As the n_H is suppressed by positive V_g , T_c is enhanced up to 45K. (From Lei, B. et al., Physical Review Letters (2016))

Figure 5.17 shows both optical and AFM images of a fabricated device. With the large size shown in optical image (Figure 5.17(a)) and a nice flat surface and uniform thickness of 47nm all around shown in Figure 5.17(b-c) it ensures good quality contacts for ionic-liquid gating purpose since the application of gate voltage is often harmful to devices. The R-T measurement without ionic liquid found the T_c round 10K shown in Figure 5.18. We examined the magnetic field dependence of T_c with the field applied perpendicularly, as shown in the inset figure. The result confirms that the T_c is suppressed with magnetic field as a typical effect, setting up a good test base of the gating effect.

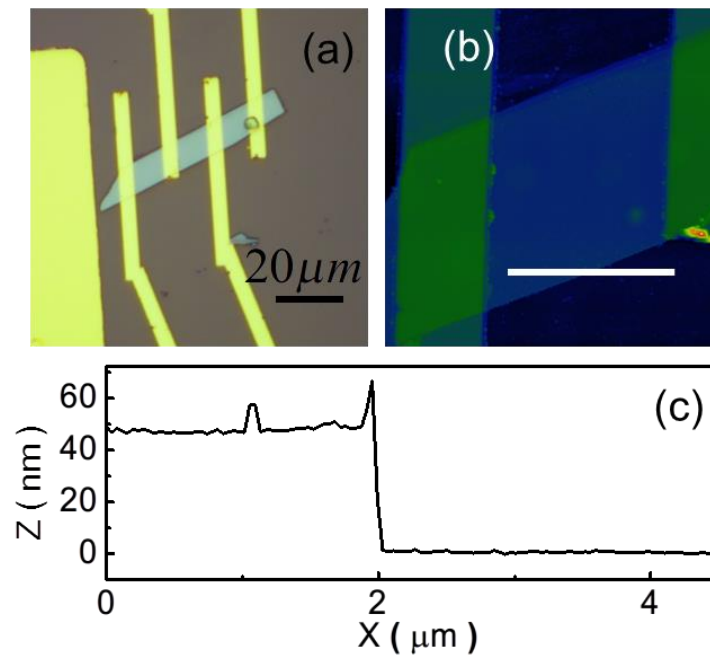


Figure 5.17: The fabricated $\text{FeSe}_{0.5}\text{Te}_{0.5}$ device with flake thickness 47nm.

(a) optical image of the device (b) AFM image (c) profile of the white line in (b) shows the thickness 47 nm.

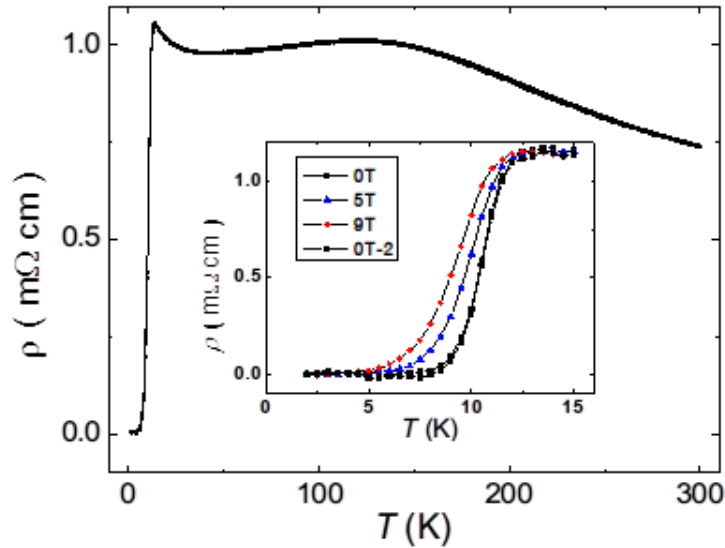


Figure 5.18: The R-T curve of superconducting $\text{FeSe}_{0.5}\text{Te}_{0.5}$ 47nm flake.

Inset: T_c is suppressed by the presence of magnetic field. The sequence started with no field applied (0T) and scanned with 5 Tesla and 9 Tesla of perpendicular field. Finally 0T was scanned again for consistency.

After the initial test we applied the ionic liquid on the device and cooled it down again (details described in Chapter 3). Right above the freezing point of the IL (around 180K), we scanned the gate voltage at 200K and found no significant effect to the resistance value. Then the sample was cooled down with 6V gating voltage. Interestingly, the change in T_c for this device is much smaller than what has been observed in FeSe nanoflakes.

There could be two reasons regarding the smaller electrostatic gating effect observed in our devices. The most possible one is the flake (47nm) is too thick so that the number of doped carrier on the first or two layers on the surface is not large enough to change the overall behavior, though the resistivity reduced $\sim 10\%$ at low temperature right

above T_c implies an increase of carrier number via gating. The other possibility comes from the insulating surface of the exfoliated flakes which we removed before depositing ionic liquid on the top of the device. The surface of FeTe or FeSeTe flakes is quite insulating possibly because of oxidation or degradation leading to a deformed structure (observed with TEM on FeTe surface.) The deformed surface could shield the underneath layers so the carrier doping becomes not quite efficient.

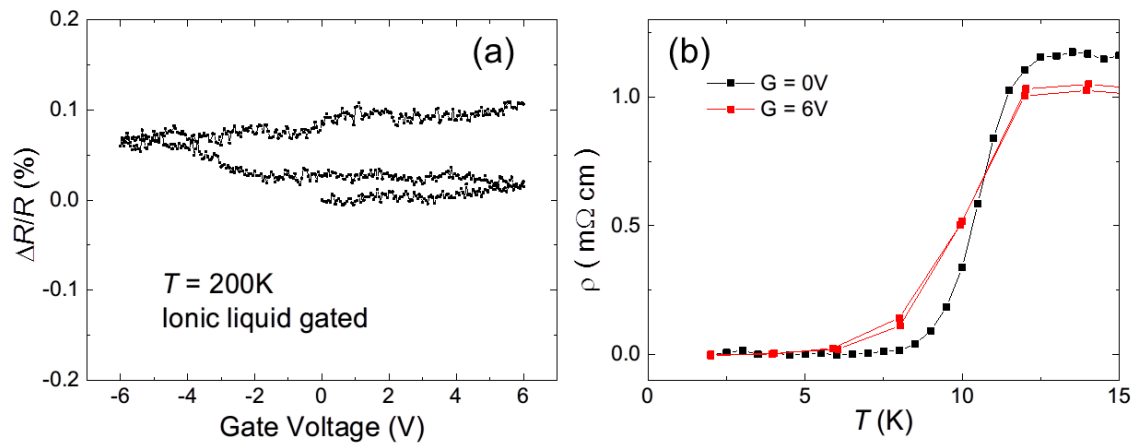


Figure 5.19: The device with the ionic liquid gating. (a) The resistance change as a function of gate voltage scanned from 0 to 6V, 6V to -6V and -6V to 6V at 200K (right above the freezing point of the ionic liquid). The change is actually negligible because the small non-reversible drift of resistance value is common when sweeping gate voltage since the liquid could be flowing. (b) Scanning of T_c with the ionic liquid and G is the gate voltage. The $G = 6V$ data has the resistivity slightly lower than the $G = 0V$ but T_c does not change much.

5.6 Summary

In summary, we report the study of electronic transport of exfoliated FeTe_{1-x} nanoflakes with various thickness. We find that while thick flakes behave similar to the

bulk counterpart and exhibit sharp first-order magnetic and structural phase transition simultaneously, flakes with intermediate thickness show a broadening of the structural phase transition followed by an onset of superconducting-like transition, which might be associated with the (partial) relaxation of structural distortion of FeTe_4 tetrahedra due to the absence of the constraint on the surface and interface of exfoliated thin flakes. With further decreasing thickness, the nanoflakes behave as a highly disordered two-dimensional system exhibiting charge-carrier localized states with largely enhanced magnetoresistance at low temperature, both of which can be well captured using the variable range hopping model with a localization length of ~ 10 nm due to the excess of Fe.

Chapter 6

Summary and Future Vision

In this dissertation, we have discussed the motivation in Chapter 1, several characterization methods in Chapter 2, detailed procedures and a lot of problem-solving in Chapter 3. The results from the studies of $\text{Ca}_3\text{Ru}_2\text{O}_7$, Ca_2RuO_4 , $\text{FeTe}_{0.85}$ and $\text{FeSe}_{0.5}\text{Te}_{0.5}$ exfoliated flakes are presented and discussed in Chapter 4 and 5. At the end of this dissertation, I would like to summarize the major progress we made and discuss the possibility of future experiment and expected discoveries.

On the part of preparation of samples, the invention of the “Gorilla glue method” used to exfoliate calcium ruthenate is certainly the greatest breakthrough. The cleavage of large single crystals in-situ is pretty common in surface studies, but such a method combined with mechanical exfoliation and turning the seemingly impossible exfoliation to sub-10 nm flakes possible is unprecedented. The contact resistance issue solved by changing adhesion layer material and in-situ ion milling, as well as the working procedure set up to prevent ESD hazard also play important roles and pave the way to the real study of atomically thin strongly correlated materials.

The decrease of transition temperature T_{MIT} in $\text{Ca}_3\text{Ru}_2\text{O}_7$ flakes below 10 nm indicates the existence of pure thickness effect in the system without substrate-induced strain. The effect may be related to the increased distortion of the surface layer by oxygen loss. The dramatic change in magnetoresistance (MR) as a function of field strength or in-plane rotation angle implies a very different magnetic structure in thinner flakes,

which may be closed to the incommensurate magnetic order observed in Fe-doped $\text{Ca}_3\text{Ru}_2\text{O}_7$. Even though the transport measurement can only provide indirect evidences, it is still quite exciting to see such a nanoscale size effect on magnetic structure. The lateral width effect on the low-temperature metallic state is still an unresolved one. Quantized conductance is calculated but it does not account for the experimental observation.

In the chapter of Fe_{1+y}Te flakes, the AFM transition and the transport properties are found to change drastically in sub-100 nm regime. The transition becomes broad around 30 nm and disappeared completely when it approaches 20 nm. Thinner flakes show insulating behavior in all temperature range accompanied enhanced MR. The behaviors can be described using the VRH model. Fitting both the R-T curve and the MR-H curves yields self-consistent result indicating the localization length around 10 nm.

A 47 nm $\text{FeSe}_{0.5}\text{Te}_{0.5}$ flake show superconductor transition around 12K the same as the bulk. We tried to apply the ionic liquid gating but did not see any significant effect on T_c , the reason could be either the flake being too thick or the surface layer blocking the carrier doping.

Besides of unresolved projects discussed in Chapter 4&5, there is still plenty of possibility in our attempt to combine the correlated system to nanostructures. In the short term the characterization of $\text{Ca}_3\text{Ru}_2\text{O}_7$ flakes with micro-XRD is definitely important as a direct evidence for surface relaxation of distortion. And magnetic force microscopy scanning of the flake before and after applied field may provide possible evidence of magnetic structure change in thinner flakes.

In the middle term, the solution to the problems encountered in ionic liquid gating experiments is desired. In my opinion there are some clues on the possible ways to avoid

these problems. One is the gate should never be connected to the source meter before it is cooled down to 200K or below. Another one is the test of low temperature ionic liquid attachment on hydrophilic and hydrophobic surfaces. Glass vessels could be used to avoid the dispersing of ionic liquid and platinum wires serves as the gate. Even though this method use much more ionic liquid on gating one device, it still worth a try on important devices because it solves the problem and promises the liquid is always in place when the gate voltage is applied. Again as mentioned in Chapter 3, initial tests could be done on graphene devices since the preparation is way much easier, parent material HOPG is cheap and available from vast choices of providers and the tolerance of ESD is huge compared to our ruthenate devices. For training purposes, I strongly suggest every new student following this project starts with preparing and measuring a gate-effect device of graphene with both bottom gate and ionic-liquid gate. This route contains almost all necessary skills needed in the project and will significantly reduce the frustration of beginners and the waste of precious crystals. If the ionic liquid problem can be finally solved, the carrier doping effect will be explored on thinner flakes of FeTe, Fe(Se,Te) and calcium ruthenates and I expect the shift of T_{MIT} or induced superconductivity can happen in these materials.

In the long term, the exfoliation method can be applied on more layered materials with strong binding forces, especially those materials which cannot be made single crystal thin film through epitaxial growth. At the beginning, it would be reasonable to explore more layered structured compounds in Ruddlesden-Popper series beyond ruthenate. Manganites are the most possible choices, particularly $La_{2-2x}Sr_{1+2x}Mn_2O_7$ with the intra-bilayer and inter-bilayer magnetic coupling changing dramatically with different

La/Sr ratio. Summarized by T. Kimura and Y. Tokura¹¹⁴ from a list of literature¹¹⁵⁻¹¹⁹, with $x \sim 0.3$ it has perpendicular intra-bilayer FM coupling and inter-bilayer AFM coupling but when x increases up to 0.32 the inter-bilayer coupling turns FM. Further increasing the x up to 0.4 makes all bi-layers coupling FM at in-plane direction. For $x > 0.4$ canted AFM is formed within the bilayer and the cant angle increases with increasing x . Finally A-type AFM is achieved at $x = 0.5$. Even though there has been the epitaxial MBE thin film growth of the material already¹²⁰, the grown thin film (50 cycles which should yield 50 unit cells) had the Curie temperature $T_C = 75\text{K}$, which is much lower than bulk ($\sim 120\text{K}$), indicating there might be still influence from the substrate or the crystallinity might be lower in the grown thin film compared to bulk (the authors consider small amount of 1-1-3 phases in grown thin films). The problems in the epitaxially grown thin film actually inspire new hopes of applying the exfoliation method in these decade-old materials. For $x = 0.3$ and $x = 0.32$ compound, my expectation is the effect of increased distortion may shift the configuration to different x ratio when it is exfoliated into sub-10 nm thin flakes. In $x > 0.4$ compounds, it would be interesting to examine if the canted-AFM or the A-type AFM ($x=0.5$) order will vanish in thin flakes as in the $\text{Ca}_3\text{Ru}_2\text{O}_7$ flakes.

Like the old proverb says, “The work will teach you how to do it”. Many of the solutions to the problems of this project did not even exist before one takes a look on them seriously. Fortunately most of hurdles are removed and interesting physics are dug out. I hope more surprising phenomena can be discovered in nanoscale from follow-up people in this thesis project.

REFERENCES

REFERENCES

- 1 Boer, J. H. d. & Verwey, E. J. W. Semi-conductors with partially and with completely filled 3d -lattice bands. *Proceedings of the Physical Society* **49**, 59-71, (1937).
- 2 Wu, M. K. *et al.* Superconductivity at 93 K in a new mixed-phase Yb-Ba-Cu-O compound system at ambient pressure. *Physical Review Letters* **58**, 908-910, (1987).
- 3 Kamihara, Y. *et al.* Iron-Based Layered Superconductor: LaOFeP. *Journal of the American Chemical Society* **128**, 10012-10013, (2006).
- 4 Kamihara, Y., Watanabe, T., Hirano, M. & Hosono, H. Iron-Based Layered Superconductor $\text{La}[\text{O}_{1-x}\text{F}_x]\text{FeAs}$ ($x = 0.05-0.12$) with $T_c = 26$ K. *Journal of the American Chemical Society* **130**, 3296-3297, (2008).
- 5 Berglund, C. N. & Jayaraman, A. Hydrostatic-Pressure Dependence of the Electronic Properties of VO_2 , Near the Semiconductor-Metal Transition Temperature. *Physical Review* **185**, 1034-1039, (1969).
- 6 Neuman, C. H., Lawson, A. W. & Brown, R. F. Pressure dependence of the resistance of VO_2 . *The Journal of Chemical Physics* **41**, 1591-1595, (1964).
- 7 Stefanovich, G., Pergament, A. & Stefanovich, D. Electrical switching and Mott transition in VO_2 . *Journal of Physics: Condensed Matter* **12**, 8837-8845, (2000).
- 8 Kubota, M. *et al.* Neutron scattering studies on magnetic structure of the double-layered manganite $\text{La}_{2-2x}\text{Sr}_{1+2x}\text{Mn}_2\text{O}_7$ ($0.30 \leq x \leq 0.50$). *Journal of Physics and Chemistry of Solids* **60**, 1161-1164, (1999).
- 9 Tomioka, Y., Asamitsu, A., Kuwahara, H., Moritomo, Y. & Tokura, Y. Magnetic-field-induced metal-insulator phenomena in $\text{Pr}_{1-x}\text{Ca}_x\text{MnO}_3$ with controlled charge-ordering instability. *Physical Review B* **53**, R1689-R1692, (1996).
- 10 Nakatsuji, S. & Maeno, Y. Switching of magnetic coupling by a structural symmetry change near the Mott transition in $\text{Ca}_{2-x}\text{Sr}_x\text{RuO}_4$. *Physical Review B - Condensed Matter and Materials Physics* **62**, 6458-6466, (2000).
- 11 Nakamura, F. Pressure-induced Mott transition and related novel quantum phenomena in Ca_2RuO_4 . *Journal of the Physical Society of Japan* **76**, 96-99, (2007).
- 12 Snow, C. S. *et al.* Pressure-tuned collapse of the Mott-like state in $\text{Ca}_{n+1}\text{Ru}_n\text{O}_{3n+1}$ ($n=1,2$): Raman spectroscopic studies. *Physical review letters* **89**, 226401-226401, (2002).
- 13 Bohnenbuck, B. *et al.* Magnetic structure and orbital state of $\text{Ca}_3\text{Ru}_2\text{O}_7$ investigated by resonant x-ray diffraction. *Physical Review B* **77**, 224412-224412, (2008).
- 14 Saito, R., Fujita, M., Dresselhaus, G. & Dresselhaus, M. S. Electronic structure of chiral graphene tubules. *Applied Physics Letters* **60**, 2204-2206, (1992).

- 15 Van Wees, B. J. *et al.* Quantized conductance of point contacts in a two-dimensional electron gas. *Physical Review Letters* **60**, 848-850, (1988).
- 16 Mikheenko, P. *et al.* Phase slips in submicrometer YBaCu₃O_{7- δ} bridges. *Physical Review B* **72**, 174506-174506, (2005).
- 17 Wei, J., Wang, Z., Chen, W. & Cobden, D. H. New aspects of the metal-insulator transition in single-domain vanadium dioxide nanobeams. *Nature nanotechnology* **4**, 420-424, (2009).
- 18 Cao, J. *et al.* Strain engineering and one-dimensional organization of metal-insulator domains in single-crystal vanadium dioxide beams. *Nature nanotechnology* **4**, 732-737, (2009).
- 19 Garcia-Barriocanal, J. *et al.* Electronically driven superconductor-insulator transition in electrostatically doped La₂CuO_{4+ δ} thin films. *Physical Review B - Condensed Matter and Materials Physics* **87**, 1-11, (2013).
- 20 Hong, X., Posadas, A., Lin, A. & Ahn, C. H. Ferroelectric-field-induced tuning of magnetism in the colossal magnetoresistive oxide La_{1-x}Sr_xMnO₃. *Physical Review B* **68**, 134415-134415, (2003).
- 21 Novoselov, K. S. *et al.* Electric field effect in atomically thin carbon films. *Science (New York, N.Y.)* **306**, 666-669, (2004).
- 22 Novoselov, K. S. *et al.* Two-dimensional atomic crystals. *Proceedings of the National Academy of Sciences of the United States of America* **102**, 10451-10453, (2005).
- 23 Teweldebrhan, D., Goyal, V. & Balandin, A. A. Exfoliation and characterization of bismuth telluride atomic quintuples and quasi-two-dimensional crystals. *Nano Letters* **10**, 1209-1218, (2010).
- 24 Mott, N. F. & Peierls, R. Discussion of the paper by de Boer and Verwey. *Proceedings of the Physical Society* **49**, 72-73, (1937).
- 25 Imada, M., Fujimori, A. & Tokura, Y. Metal-insulator transitions. *Reviews of Modern Physics* **70**, 1039-1263, (1998).
- 26 Yeh, K.-W. *et al.* Tellurium substitution effect on superconductivity of the alpha-phase Iron Selenide. *Epl* **37002**, 14-14, (2008).
- 27 Fang, M. H. *et al.* Superconductivity close to magnetic instability in Fe(Se_{1-x}Te_x)_{0.82}. *Physical Review B* **78**, 224503, (2008).
- 28 Hu, R., Bozin, E. S., Warren, J. B. & Petrovic, C. Superconductivity, magnetism, and stoichiometry of single crystals of Fe_{1+y}(Te_{1-x}S_x)_z. *Physical Review B* **80**, 214514-214514, (2009).
- 29 Li, S. *et al.* First-order magnetic and structural phase transitions in Fe_{1+y}Se_xTe_{1-x}. *Physical Review B - Condensed Matter and Materials Physics* **79**, 1-7, (2009).

- 30 Nie, Y. F., Telesca, D., Budnick, J. I., Sinkovic, B. & Wells, B. O. Superconductivity induced in iron telluride films by low-temperature oxygen incorporation. *Physical Review B - Condensed Matter and Materials Physics* **82**, 2-5, (2010).
- 31 Han, Y. *et al.* Superconductivity in Iron telluride thin films under tensile stress. *Physical Review Letters* **104**, 8-11, (2010).
- 32 Lei, B. *et al.* Evolution of High-Temperature Superconductivity from a Low- T_c Phase Tuned by Carrier Concentration in FeSe Thin Flakes. *Physical Review Letters* **116**, 077002, (2016).
- 33 Yue, C. *et al.* Nanoscale Inhomogeneous Superconductivity in Fe(Te_{1-x}Se_x) Probed by Nanostructure Transport. *ACS Nano* **10**, 429-435, (2016).
- 34 Hänke, T. *et al.* Reorientation of the diagonal double-stripe spin structure at Fe_{1+y}Te bulk and thin-film surfaces. *Nature Communications* **8**, 13939-13939, (2017).
- 35 Xi, X. *et al.* Strongly enhanced charge-density-wave order in monolayer NbSe₂. *Nature Nanotechnology* **10**, 1-6, (2015).
- 36 Blake, P. *et al.* Making graphene visible. *Applied Physics Letters* **91**, (2007).
- 37 Ferrari, A. C. *et al.* Raman Spectrum of Graphene and Graphene Layers. *Physical Review Letters* **97**, 187401-187401, (2006).
- 38 Puls, C. P. *et al.* Structural and metal-insulator transitions in ionic liquid-gated Ca₃Ru₂O₇ surface. *Applied Physics Letters* **104**, 253503, (2014).
- 39 Liang, X. *et al.* Toward clean and crackless transfer of graphene. *ACS Nano* **5**, 9144-9153, (2011).
- 40 Tsukada, I. *et al.* Mobility analysis of FeTe thin films. *Journal of the Physical Society of Japan* **80**, 1-4, (2011).
- 41 Goldman, a. M. Electrostatic Gating of Ultrathin Films. *Annual Review of Materials Research* **44**, 45-63, (2014).
- 42 Dagotto, E. Complexity in Strongly Correlated Electronic Systems. *Science* **309**, 257, (2005).
- 43 Dagotto, E. & Tokura, Y. Strongly Correlated Electronic Materials: Present and Future. *MRS Bulletin* **33**, 1037-1045, (2011).
- 44 Wei, J. & Natelson, D. Nanostructure studies of strongly correlated materials. *Nanoscale* **3**, 3509-3521, (2011).
- 45 Tian, W., Pan, X. Q., Haeni, J. H. & Schlom, D. G. Transmission electron microscopy study of n= 1–5 Sr_{n+1}Ti_nO_{3n+1} epitaxial thin films. *Journal of Materials Research* **16**, 2013-2026, (2011).

- 46 Sandilands, L. J. *et al.* Stability of exfoliated $\text{Bi}_2\text{Sr}_2\text{Dy}_x\text{Ca}_{1-x}\text{Cu}_2\text{O}_{8+\delta}$ studied by Raman microscopy. *Physical Review B* **82**, 064503, (2010).
- 47 Mackenzie, A. P. & Grigera, S. A. Electronic Properties of the Layered Perovskite Ruthenates: Correlated Electron Physics Approaching the Low-Disorder Limit. *Journal of Low Temperature Physics* **135**, 39-50, (2004).
- 48 Andrew, P. M., Yoshiteru, M. & Stephen, R. J. Novel quantum order in the ruthenates. *Physics World* **15**, 33, (2002).
- 49 Cao, G., Alexander, C. S., McCall, S., Crow, J. E. & Guertin, R. P. From antiferromagnetic insulator to ferromagnetic metal: a brief review of the layered ruthenates. *Materials Science and Engineering: B* **63**, 76-82, (1999).
- 50 Yoshida, Y. *et al.* Quasi-two-dimensional metallic ground state of $\text{Ca}_3\text{Ru}_2\text{O}_7$. *Physical Review B* **69**, 220411, (2004).
- 51 Mackenzie, A. P. *et al.* Quantum Oscillations in the Layered Perovskite Superconductor Sr_2RuO_4 . *Physical Review Letters* **76**, 3786-3789, (1996).
- 52 Liu, Y. *et al.* Electrical transport properties of single-crystal $\text{Sr}_3\text{Ru}_2\text{O}_7$ The possible existence of an antiferromagnetic instability at low temperatures. *Physical Review B* **63**, 174435, (2001).
- 53 Cao, G., McCall, S., Crow, J. E. & Guertin, R. P. Observation of a Metallic Antiferromagnetic Phase and Metal to Nonmetal Transition in $\text{Ca}_3\text{Ru}_2\text{O}_7$. *Physical Review Letters* **78**, 1751-1754, (1997).
- 54 Yoshida, Y. *et al.* Crystal and magnetic structure of $\text{Ca}_3\text{Ru}_2\text{O}_7$. *Physical Review B* **72**, 054412, (2005).
- 55 Bao, W., Mao, Z. Q., Qu, Z. & Lynn, J. W. Spin Valve Effect and Magnetoresistivity in Single Crystalline $\text{Ca}_3\text{Ru}_2\text{O}_7$. *Physical Review Letters* **100**, 247203, (2008).
- 56 Ke, X. *et al.* Spin-wave excitation in the antiferromagnetic bilayer ruthenate $\text{Ca}_3\text{Ru}_2\text{O}_7$. *Physical Review B* **84**, 014422, (2011).
- 57 Yoshida, Y. *et al.* Crystal and magnetic structure of $\text{Ca}_3\text{Ru}_2\text{O}_7$. *Physical Review B* **72**, 054412-054412, (2005).
- 58 Cao, G., Balicas, L., Xin, Y., Crow, J. E. & Nelson, C. S. Quantum oscillations, colossal magnetoresistance, and the magnetoelastic interaction in bilayered $\text{Ca}_3\text{Ru}_2\text{O}_7$. *Physical Review B* **67**, 184405, (2003).
- 59 Liu, G.-Q. Mott transition and magnetic anisotropy in $\text{Ca}_3\text{Ru}_2\text{O}_7$. *Physical Review B* **84**, 235137, (2011).
- 60 Baumberger, F. *et al.* Nested Fermi Surface and Electronic Instability in $\text{Ca}_3\text{Ru}_2\text{O}_7$. *Physical Review Letters* **96**, 107601, (2006).

- 61 Qu, Z. *et al.* Unusual heavy-mass nearly ferromagnetic state with a surprisingly large Wilson ratio in the double layered ruthenates $(\text{Sr}_{1-x}\text{Ca}_x)_3\text{Ru}_2\text{O}_7$. *Physical Review B* **78**, 180407, (2008).
- 62 Ke, X. *et al.* Commensurate-incommensurate magnetic phase transition in the Fe-doped bilayer ruthenate $\text{Ca}_3\text{Ru}_2\text{O}_7$. *Physical Review B* **89**, 220407, (2014).
- 63 Lin, X. N., Zhou, Z. X., Durairaj, V., Schlottmann, P. & Cao, G. Colossal Magnetoresistance by Avoiding a Ferromagnetic State in the Mott System $\text{Ca}_3\text{Ru}_2\text{O}_7$. *Physical Review Letters* **95**, 017203, (2005).
- 64 Snow, C. S. *et al.* Pressure-Tuned Collapse of the Mott-Like State in $\text{Ca}_{n+1}\text{Ru}_n\text{O}_{3n+1}$ ($n=1,2$): Raman Spectroscopic Studies. *Physical Review Letters* **89**, 226401, (2002).
- 65 Peng, J. *et al.* Interplay between the lattice and spin degrees of freedom in $(\text{Sr}_{1-x}\text{Ca}_x)_3\text{Ru}_2\text{O}_7$. *Physical Review B* **82**, 024417, (2010).
- 66 Matzdorf, R. *et al.* Ferromagnetism Stabilized by Lattice Distortion at the Surface of the p-Wave Superconductor Sr_2RuO_4 . *Science* **289**, 746, (2000).
- 67 Moore, R. G. *et al.* A Surface-Tailored, Purely Electronic, Mott Metal-to-Insulator Transition. *Science* **318**, 615-619, (2007).
- 68 Martínez-Anaya, O., García-Valdés, J., de la Mora, P. & Tavizón, G. Synthesis and Crystal Structure of Oxygen-deficient Bilayer Ruthenate $\text{Sr}_3\text{Ru}_2\text{O}_{7-\delta}$. *Australian Journal of Chemistry* **67**, 777-783, (2014).
- 69 Takenaka, K., Okamoto, Y., Shinoda, T., Katayama, N. & Sakai, Y. Colossal negative thermal expansion in reduced layered ruthenate. *Nature Communications* **8**, 14102, (2017).
- 70 Fobes, D., Peng, J., Qu, Z., Liu, T. J. & Mao, Z. Q. Magnetic phase transitions and bulk spin-valve effect tuned by in-plane field orientation in $\text{Ca}_3\text{Ru}_2\text{O}_7$. *Physical Review B* **84**, 014406, (2011).
- 71 Cao, G., Balicas, L., Xin, Y., Crow, J. & Nelson, C. Quantum oscillations, colossal magnetoresistance, and the magnetoelastic interaction in bilayered $\text{Ca}_3\text{Ru}_2\text{O}_7$. *Physical Review B* **67**, 184405-184405, (2003).
- 72 Zhu, M. & al, e. *unpublished*, (2017).
- 73 Zhu, M. *Phys. Rev. B in press*, (2017).
- 74 Braden, M., André, G., Nakatsuji, S. & Maeno, Y. Crystal and magnetic structure of Ca_2RuO_4 Magnetoelastic coupling and the metal-insulator transition. *Physical Review B* **58**, 847-861, (1998).
- 75 Ke, X. *et al.* Emergent electronic and magnetic state in $\text{Ca}_3\text{Ru}_2\text{O}_7$ induced by Ti doping. *Phys. Rev. B* **84**, 201102-201102, (2011).

- 76 Alexander, C. *et al.* Destruction of the Mott insulating ground state of Ca_2RuO_4 by a structural transition. *Physical Review B* **60**, R8422-R8425, (1999).
- 77 Friedt, O. *et al.* Structural and magnetic aspects of the metal-insulator transition in $\text{Ca}_{2-x}\text{Sr}_x\text{RuO}_4$. *Physical Review B* **63**, 174432-174432, (2001).
- 78 Miao, L. *et al.* Itinerant ferromagnetism and geometrically suppressed metal-insulator transition in epitaxial thin films of Ca_2RuO_4 . *Applied Physics Letters* **100**, 052401-052401, (2012).
- 79 Wang, X., Xin, Y., Stampe, P. a., Kennedy, R. J. & Zheng, J. P. Epitaxial thin film growth of $\text{Ca}_2\text{RuO}_{4+\delta}$ by pulsed laser deposition. *Applied Physics Letters* **85**, 6146-6146, (2004).
- 80 Kamihara, Y. *et al.* Iron-Based Layered Superconductor: LaOFeP . *Journal of the American Chemical Society* **128**, 10012-10013, (2006).
- 81 Johnston, D. C. The puzzle of high temperature superconductivity in layered iron pnictides and chalcogenides. *Advances in Physics* **59**, 803-1061, (2010).
- 82 Paglione, J. & Greene, R. L. High-temperature superconductivity in iron-based materials. *Nature Physics* **6**, 645-658, (2010).
- 83 Stewart, G. R. Superconductivity in iron compounds. *Reviews of Modern Physics* **83**, (2011).
- 84 Hsu, F.-C. *et al.* Superconductivity in the PbO-type structure $\alpha\text{-FeSe}$. *Proceedings of the National Academy of Sciences* **105**, 14262-14264, (2008).
- 85 Kuo-Wei, Y. *et al.* Tellurium substitution effect on superconductivity of the α -phase iron selenide. *EPL (Europhysics Letters)* **84**, 37002, (2008).
- 86 McQueen, T. M. *et al.* Extreme sensitivity of superconductivity to stoichiometry in $\text{Fe}_{1+\delta}\text{Se}$. *Physical Review B* **79**, 014522, (2009).
- 87 Mizuguchi, Y. & Takano, Y. Review of Fe Chalcogenides as the Simplest Fe-Based Superconductor. *Journal of the Physical Society of Japan* **79**, 102001, (2010).
- 88 Mizuguchi, Y., Tomioka, F., Tsuda, S., Yamaguchi, T. & Takano, Y. Substitution effects on FeSe superconductor. *Journal of the Physical Society of Japan* **78**, 1-5, (2009).
- 89 Liu, T. J. *et al.* Charge-carrier localization induced by excess Fe in the superconductor $\text{Fe}_{1+y}\text{Te}_{1-x}\text{Se}_x$. *Physical Review B* **80**, 174509, (2009).
- 90 Liu, T. J. *et al.* From $(\pi,0)$ magnetic order to superconductivity with (π,π) magnetic resonance in $\text{Fe}_{1.02}\text{Te}_{1-x}\text{Se}_x$. *Nat Mater* **9**, 718-720, (2010).
- 91 Zhang, A. M., Xia, T. L., Kong, L. R., Xiao, J. H. & Zhang, Q. M. Effects on superconductivity of transition-metal doping in $\text{FeSe}_{0.5}\text{Te}_{0.5}$. *Journal of Physics: Condensed Matter* **22**, 245701, (2010).

- 92 Medvedev, S. *et al.* Electronic and magnetic phase diagram of β -Fe_{1.01}Se with superconductivity at 36.7K under pressure. *Nat Mater* **8**, 630-633, (2009).
- 93 Wang, Q.-Y. *et al.* Interface-Induced High-Temperature Superconductivity in Single Unit-Cell FeSe Films on SrTiO₃. *Chinese Physics Letters* **29**, 037402-037402, (2012).
- 94 Liu, D. *et al.* Electronic origin of high-temperature superconductivity in single-layer FeSe superconductor. *Nature Communications* **3**, 931, (2012).
- 95 He, S. *et al.* Phase diagram and electronic indication of high-temperature superconductivity at 65 K in single-layer FeSe films. *Nat Mater* **12**, 605-610, (2013).
- 96 Tan, S. *et al.* Interface-induced superconductivity and strain-dependent spin density waves in FeSe/SrTiO₃ thin films. *Nature Materials* **12**, 634-634, (2013).
- 97 Lee, J. J. *et al.* Interfacial mode coupling as the origin of the enhancement of T_c in FeSe films on SrTiO₃. *Nature* **515**, 245-248, (2014).
- 98 Shiogai, J., Ito, Y., Mitsuhashi, T., Nojima, T. & Tsukazaki, A. Electric-field-induced superconductivity in electrochemically etched ultrathin FeSe films on SrTiO₃ and MgO. *Nat Phys* **12**, 42-46, (2016).
- 99 Ge, J.-F. *et al.* Superconductivity above 100 K in single-layer FeSe films on doped SrTiO₃. *Nat Mater* **14**, 285-289, (2015).
- 100 Qingyan, W. *et al.* Thickness dependence of superconductivity and superconductor–insulator transition in ultrathin FeSe films on SrTiO₃ (001) substrate. *2D Materials* **2**, 044012, (2015).
- 101 Hanzawa, K., Sato, H., Hiramatsu, H., Kamiya, T. & Hosono, H. Electric field-induced superconducting transition of insulating FeSe thin film at 35 K. *Proceedings of the National Academy of Sciences* **113**, 3986-3990, (2016).
- 102 He, J. *et al.* Electronic evidence of an insulator–superconductor crossover in single-layer FeSe/SrTiO₃ films. *Proceedings of the National Academy of Sciences* **111**, 18501-18506, (2014).
- 103 Zhang, W. *et al.* Interface charge doping effects on superconductivity of single-unit-cell FeSe films on SrTiO₃ substrates. *Physical Review B* **89**, 060506, (2014).
- 104 Yang, S. *et al.* Thickness-Dependent Coherent Phonon Frequency in Ultrathin FeSe/SrTiO₃ Films. *Nano Letters* **15**, 4150-4154, (2015).
- 105 Manna, S. *et al.* Interfacial superconductivity in a bi-collinear antiferromagnetically ordered FeTe monolayer on a topological insulator. *Nature Communications* **8**, 14074, (2017).
- 106 Xia, T. L. *et al.* Raman phonons of α -FeTe and Fe_{1.03}Se_{0.3}Te_{0.7} single crystals. *Physical Review B - Condensed Matter and Materials Physics* **79**, 1-4, (2009).

- 107 Bao, W. *et al.* Tunable $(\delta\pi, \delta\pi)$ -Type Antiferromagnetic Order in α -Fe(Te,Se) Superconductors. *Physical Review Letters* **102**, 247001, (2009).
- 108 Zhang, Z. T. *et al.* Superconductivity in Fe_{1.05}Te:O_x single crystals. *Physical Review B* **88**, 214511, (2013).
- 109 Mott, N. F. Conduction in non-crystalline materials. *Philosophical Magazine* **19**, 835-852, (1969).
- 110 Van Keuls, F. W., Hu, X. L., Jiang, H. W. & Dahm, A. J. Screening of the Coulomb interaction in two-dimensional variable-range hopping. *Physical Review B* **56**, 1161-1169, (1997).
- 111 Ovchinnikov, D., Allain, A., Huang, Y.-S., Dumcenco, D. & Kis, A. Electrical Transport Properties of Single-Layer WS₂. *ACS Nano* **8**, 8174-8181, (2014).
- 112 Tamai, A. *et al.* Strong Electron Correlations in the Normal State of the Iron-Based FeSe_{0.42}Te_{0.58} Superconductor Observed by Angle-Resolved Photoemission Spectroscopy. *Physical Review Letters* **104**, 097002, (2010).
- 113 Schoepe, W. Variable-range hopping conduction in doped germanium at very low temperatures and high magnetic fields. *Zeitschrift für Physik B Condensed Matter* **71**, 455-463, (1988).
- 114 Kimura, T. & Tokura, Y. Layered magnetic manganites. *Annual review of materials science* **30**, 451-474, (2000).
- 115 Kubota, M. *et al.* Neutron scattering studies on magnetic structure of the double-layered manganite La_{2-2x}Sr_{1+2x}Mn₂O₇ (0.30≤x≤0.50). *Journal of Physics and Chemistry of Solids* **60**, 1161-1164, (1999).
- 116 Hirota, K. *et al.* Neutron-Diffraction Studies on the Magnetic Ordering Process in the Layered Mn Perovskite La_{2-2x}Sr_{1+2x}Mn₂O₇ (x=0.40, 0.45 and 0.48). *Journal of the Physical Society of Japan* **67**, 3380-3383, (1998).
- 117 Perring, T. G., Aeppli, G., Kimura, T., Tokura, Y. & Adams, M. A. Ordered stack of spin valves in a layered magnetoresistive perovskite. *Physical Review B* **58**, R14693-R14696, (1998).
- 118 Argyriou, D. N. *et al.* Unconventional magnetostriction in layered La_{1.2}Sr_{1.8}Mn₂O₇: Evidence for spin-lattice coupling above T_C. *Physical Review B* **55**, R11965-R11968, (1997).
- 119 Battle, P. D. *et al.* Antiferromagnetism, Ferromagnetism, and Phase Separation in the GMR System Sr_{2-x}La_{1+x}Mn₂O₇. *Chemistry of Materials* **9**, 1042-1049, (1997).
- 120 Tanaka, H. & Kawai, T. Artificial construction of SrO/(La,Sr)MnO₃ layered perovskite superlattice by laser molecular-beam epitaxy. *Applied Physics Letters* **76**, 3618-3620, (2000).

